



|                  |   |
|------------------|---|
| Title            | Analyses of Some Leaking Modes  |
| Author(s)        | YOSHII, Toshikatsu  |
| Citation         | Journal of the Faculty of Science, Hokkaido University. Series 7, Geophysics, 3(4), 287-378 |
| Issue Date       | 1971-03-25  |
| Doc URL          | <a href="http://hdl.handle.net/2115/8687">http://hdl.handle.net/2115/8687</a>               |
| Type             | bulletin (article)  |
| File Information | 3(4)_p287-378.pdf   |



[Instructions for use](#)

## Analyses of Some Leaking Modes

Toshikatsu YOSHII

(Received March 23, 1970)

### Abstract

Some types of leaking modes were analyzed by utilizing OLIVER and MAJOR's as well as SU and DORMAN's methods. The mathematical reliability of these two methods, which are called "approximate methods" in the present paper, have already been confirmed by TAZIME and YOSHII. The studies of leaking modes have not been so popular, probably due to its theoretical vaguenesses and the difficulty of the calculation. Just a few papers mainly about PL waves have been published.

The leaking mode is characterized by its higher phase velocity than the shear velocity in the half space of the stratified media. The PL wave is not the only wave train which satisfies the above feature, and there exist many other interesting leaking modes as shown in the present study. The present author believes that many records which have been remained to be untouched can be analyzed in the light of the leaking mode. Two approximate methods may be the powerful tools for such analyses.

### 1. Introduction

This paper has been prepared as a synthetic report of a few papers on leaking modes written by the present author in Japanese<sup>1)-9)</sup>. The "keynote" of these papers was the analysis of observed leaking modes by using the dispersion curves obtained by the approximate methods of OLIVER and MAJOR<sup>10)</sup> and SU and DORMAN<sup>11)</sup>. All previous discussions on leaking modes were restricted in PL waves, but as will be shown in the present paper, there exist many other interesting leaking modes. At any rate, the two approximate methods above mentioned are very powerful for the analysis of these leaking modes.

One of the reasons why the present author gives attention to these approximate methods is the theoretical vagueness of the leaking mode. Since the publication of a paper by ROSENBAUM<sup>12)</sup>, the theory of the leaking mode seems to become perfect "mathematically" by noticing complex roots of the period equation. But some difficulties remain when we want to connect the mathematical result with the physical meaning. On the other hand, though the two approximate methods seem to be imperfect mathematically, they can

be understood more explicitly. TAZIME and YOSHII<sup>8)</sup> have examined the mathematical reliability of these two methods. Since "dispersion" is very stable information from the seismogram, the concept of the leaking mode may be a powerful tool for the analysis of the seismogram.

This report mainly consists of following four parts.

- 1) PL waves. (§ 3)
- 2) Surface waves on the model with a high velocity layer. (§ 4)
- 3) Wave group II observed in small explosion seismology. (§ 5)
- 4) Water waves observed in the shallow sea. (§ 6)

In § 7, some comparisons of approximate solutions and complex roots will be discussed.

#### \* List of Notations \*

- $c$  phase velocity.
- $d$  depth of the receiver.
- $f$  frequency.
- $H_i$  thickness of the  $i$ 'th layer.
- $k$  angular wave number.
- $r$  horizontal distance.
- $t$  time.
- $T$  period.
- $u$  (horizontal) ground displacement.
- $U$  group velocity.
- $z$  depth of the source.
- $a$  attenuation coefficient (§ 4.2).
- $\alpha_i$  compressional wave velocity in the  $i$ 'th layer.
- $\beta_i$  shear wave velocity in the  $i$ 'th layer.
- $\mathcal{A}$  period function ( $\mathcal{A}=0$ : period equation).
- $\rho_i$  density in the  $i$ 'th layer.
- $\sigma$  Poisson's ratio.
- $\omega$  angular frequency.

#### 2. On the leaking mode and the approximate dispersion curve.

Now, we are going to discuss elastic surface wave propagation on the layered half space. The solution of the present problem is represented by such a double integral as follows,

$$u(t, r, z, d) = \int_{-\infty}^{\infty} dk \cdot k J_0(kr) \int_{-\infty}^{\infty} d\omega \cdot \exp(-i\omega t) \cdot \left[ \frac{F(\omega, k, z, d)}{\mathcal{A}(\omega, k)} \right]. \quad (1)$$

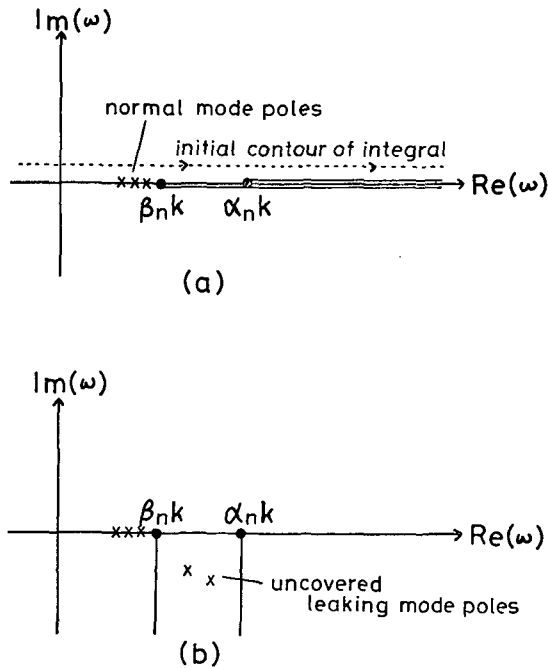


Fig. 1. Normal and leaking mode poles on  $\omega$ -plane.

Evaluation of this integral may be performed by the residual theorem for one integral and by a suitable way such as the stationary phase method for the other. This technique is called the normal mode expansion and is very useful when  $r$  and  $t$  are large. Following GILBERT<sup>13)</sup>, we shall at first evaluate the integral of  $\omega$  by the residual theorem. The dominant contribution in this integral arises from poles which are to be determined by the period equation  $\mathcal{A}=0$ .

On the complex  $\omega$ -plane (Fig. 1), integral (1) has two pairs of branch points at  $\omega=\pm\alpha_n k$  and  $\omega=\pm\beta_n k$  due to following two radicals,

$$\nu = (k^2 - \omega^2 / \alpha_n^2)^{1/2} \quad \text{and} \quad \nu' = (k^2 - \omega^2 / \beta_n^2)^{1/2} \quad (2)$$

in the integral, where suffix  $n$  indicate the value in the half space. Because of these branch points, we have four Riemann sheets which are called  $(+, +)$ ,  $(+, -)$ ,  $(-, +)$  and  $(-, -)$  sheets according to the sign of the real part of  $\nu$  and  $\nu'$ .

The roots of the period equation  $\mathcal{A}(\omega, k)=0$  on the  $(+, +)$  sheet give

familiar normal modes and lie on the real axis of the  $\omega$ -plane where  $\text{Re}(\omega) \leq \beta_n k$ . When two branch lines are taken along  $\text{Re}(\nu)=0$  and  $\text{Re}(\nu')=0$  as shown in Fig. 1 (a), no other poles are found on this uppermost sheet. Thus, the  $\omega$ -integral of Eq. (1) is completely evaluated by contributions of the normal mode poles and of two branch lines.

The contributions of these branch line integrals can be partly replaced by those of residues. When we deform the branch lines as those shown in Fig. 1 (b), poles on the other Riemann sheets are uncovered. These new complex roots yield the concept of the leaking mode.<sup>12)</sup> In this case, the integrals along two new branch lines are very small and dominant contributions in integral (1) arise from these real and complex roots. When the value of  $k$  is changed gradually, these poles take walks on the complex  $\omega$ -plane. The track of a pole is called a dispersion curve.

If we restrict our attention to the dispersion of the leaking mode, it is necessary to trace the position of the complex root. In general, when both  $\omega$  and  $k$  are taken as complex values in the period equation, the dispersion curve cannot be decided without one additional condition such as  $\text{Im}(k)=0$ <sup>13)</sup> or  $\text{Im}(\omega)=0$ <sup>14)</sup>. TAZIME<sup>15)</sup> showed that the period equation means a kind of conformal mapping from a complex variable to the other.

Even though a simple additional condition is chosen, it is still difficult to find the complex root of the period equation. OLIVER and MAJOR<sup>10)</sup> suggested a simple way to get the approximate dispersion curve for the leaking mode. They calculated the period function  $\Delta(\omega, k)$  for real  $\omega$  and real  $k$ , and defined the dispersion curve which is the trace of its minima.

The other simple method was given by SU and DORMAN<sup>11)</sup>. In their method, surface amplitude spectra<sup>16)</sup> were calculated in order to get the dispersion curve of the leaking mode. They compared their results with the complex roots obtained by GILBERT<sup>13)</sup> for the same model and got good agreements. But they have given no mathematical discussions on the approximate method. TAZIME and YOSHI<sup>8)</sup> mathematically confirmed that the solution from these simple methods agrees with the complex root when the imaginary part of the complex root is very small.

Integral (1) contains the vibration term of

$$J_0(kr) \cdot \exp(-i\omega t). \quad (3)$$

Consequently, it is immediately recognized that the imaginary part of the complex root causes some attenuation of the wave train besides geometrical spreading or absorption. This attenuation corresponds to the wave energy

leaking out from the wave guide into the half space. Because this kind of attenuation depends on the magnitude of the imaginary part of the complex root, it is concluded from TAZIME and YOSHII's study that the two approximate methods are very powerful for the analysis of the leaking mode which has large amplitude due to small attenuation.

In the present paper, dispersion curves of the leaking mode were mainly obtained by these two approximate methods. Some comparisons of the approximate solutions with the complex roots will be given in §7 in this paper. These complex roots were pursued from the start points decided by the approximate methods. Because the computer program of the author is written by the matrix method<sup>17)</sup>, the complex root for the multi-layered wave guide can be calculated easily.

### 3. PL waves.

#### 3.1 Model experiments on PL waves.

The PL wave has been the most popular leaking mode since OLIVER and MAJOR's famous paper<sup>10)</sup> was published. The general appearance of the PL wave on the earthquake seismogram is a long period dispersed wave train between P and S waves. This wave train has the nature akin to a surface wave of Rayleigh type, and has considerable attenuation. The particle orbit on the free surface of this wave train is often prograde.

Also in model seismology, PL waves have been observed frequently. KNOPOFF et al.<sup>18)</sup> observed dominant vibrations just after the P arrival, using the Brass-steel model, and attempted to explain it by the ray theory. GILBERT and LASTER<sup>19)</sup> computed the approximate dispersion curves of the PL wave by OLIVER and MAJOR's method and compared them with the dispersions of the wave trains which were observed in their model experiment. They also suggested to label PL modes according to their connections to M modes named by TOLSTOY and USDIN<sup>20)</sup>, as  $PL_{21}$ ,  $PL_{12}$  etc. In the present paper, PL waves are labeled in this manner. LASTER et al.<sup>14)</sup> computed the complex root of the period equation for the Brass-steel model. They also calculated modal seismograms, considering the dispersion curve, the excitation function, the attenuation coefficient and the instrumental response. They compared them with actual records.

In all these previous model experiments, the predominant PL wave is always  $PL_{22}$  and the "fundamental" PL wave, namely  $PL_{21}$ , is usually not found on the record. This appearance is very different from that of the

Table 1. Elastic constants of the constituent plates.

|           | $\alpha$ (km/s) | $\beta$ (km/s) | $\rho$ (g/cm <sup>3</sup> ) |
|-----------|-----------------|----------------|-----------------------------|
| Plastics  | 1.89            | 1.07           | 1.40                        |
| Aluminum  | 5.35            | 3.06           | 2.70                        |
| Lamiverre | 3.45            | 1.55           | 1.75                        |

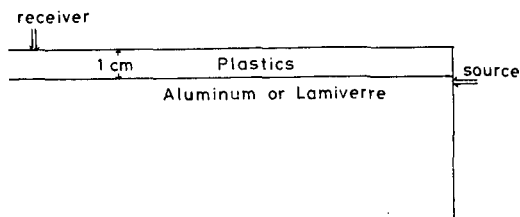


Fig. 2. Schematic diagram of the present model experiment.

earthquake record. LASTER et al. explained that this was due to the instrumental response.

Two dimensional single layer models in the present model experiment are Plastics-Aluminium and Plastics-Lamiverre models. These models will be called simply PL-AL and PL-LAM models respectively. The elastic constants of these plates, about 2 mm thick, are tabulated in Table 1. The thickness of the model layer is 1 cm. Details about the instrument used in this model experiment have been described by SATTO<sup>21)</sup>.

In the present experiment, a sound source and a receiver were arranged as shown in Fig. 2, and because of this special arrangement, PL<sub>21</sub> waves were clearly observed. It is not obvious why PL<sub>21</sub> waves were predominantly observed by this way. Probably, some source conditions, such as source depth, have the great role in this problem.

Examples of observed records are exhibited in Fig. 3. The upper trace is a record from PL-AL model and the lower trace is from PL-LAM model. The source signal is a pulse of about 7  $\mu$ s width. On both records, M<sub>11</sub> waves having large amplitude are found about 200  $\mu$ s after the arrivals of initial P waves. Between P and M<sub>11</sub> waves, two kinds of dispersed waves are recognized.

One is a wave train with longer periods, about 40  $\mu$ s, and the other is a wave train with shorter periods, about 10  $\mu$ s. Both have a nature of normal dispersion and correspond to PL<sub>21</sub> and PL<sub>22</sub> respectively. Using the same PL-AL model like this, HAMADA<sup>22)</sup> also observed PL<sub>22</sub> waves but did not PL<sub>21</sub> waves.

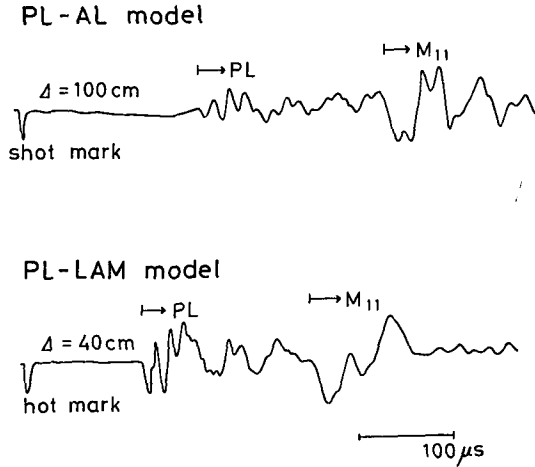


Fig. 3. Examples of records obtained from the model experiments. Upper; PL-AL model, Lower; PL-LAM model.

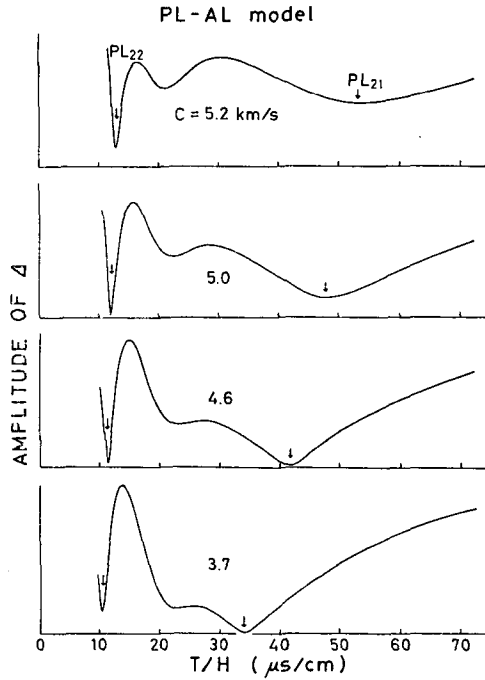


Fig. 4. Examples of the calculation of  $|\Delta|$ . Two pairs of the minima represented with small arrows correspond to  $PL_{21}$  and  $PL_{22}$  waves.

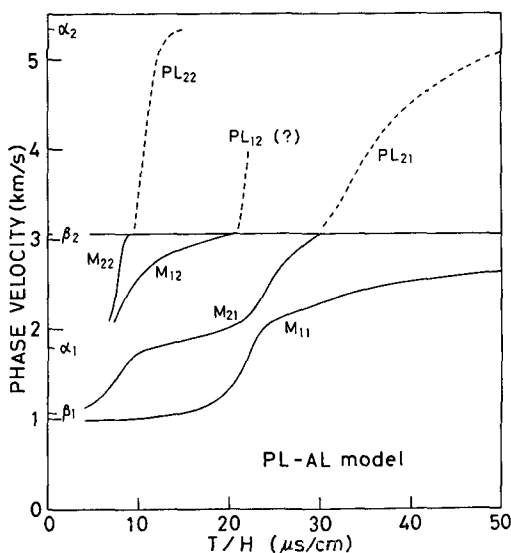


Fig. 5. Theoretical phase velocity curves of normal and leaking modes for PL-AL model. Phase velocity curves of PL waves were obtained by OLIVER and MAJOR's method.

The theoretical dispersion curves of PL waves for these two models were obtained by OLIVER and MAJOR's method. Some examples of the absolute value of the period function for PL-AL model are illustrated in Fig. 4. In order to calculate the period function, phase velocity  $c$  and frequency  $f$  were chosen as parameters. The ordinate of Fig. 4 is the arbitrary linear scale. Two pairs of sharp minima are represented with small arrows. The dispersion curves of PL waves were obtained by tracing these minima.

The phase velocity curves of both normal and leaking modes for PL-AL model are shown in Fig. 5. As mentioned before, PL waves are labeled according to connections to M waves. The minima of the period function for PL<sub>12</sub> wave are not so clear in this case.

Fig. 6 is the travel time chart of peaks and troughs of observed PL<sub>21</sub> waves for PL-AL model. Open and solid circles represent peaks and troughs of the wave train respectively. Observed phase velocity was defined as the propagation speed of a peak or a trough. Group velocity was obtained by an usual way<sup>23</sup>). The same process of the calculation was also performed for the other wave trains.

Observed phase and group velocities of PL waves are plotted in Fig. 7

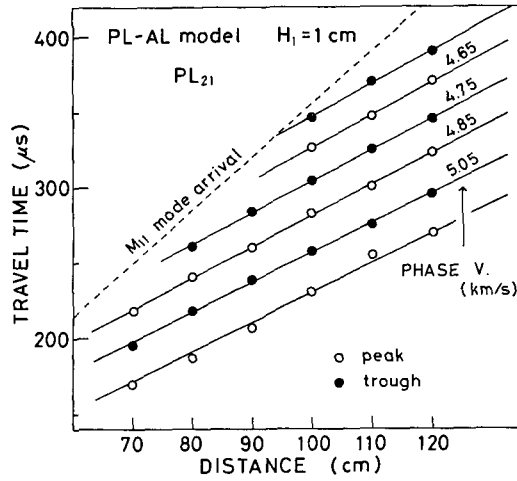


Fig. 6. Travel times of peaks and troughs of observed  $PL_{21}$  wave trains for PL-AL model. The phase velocity was obtained from the traveling speed of a peak or a trough.

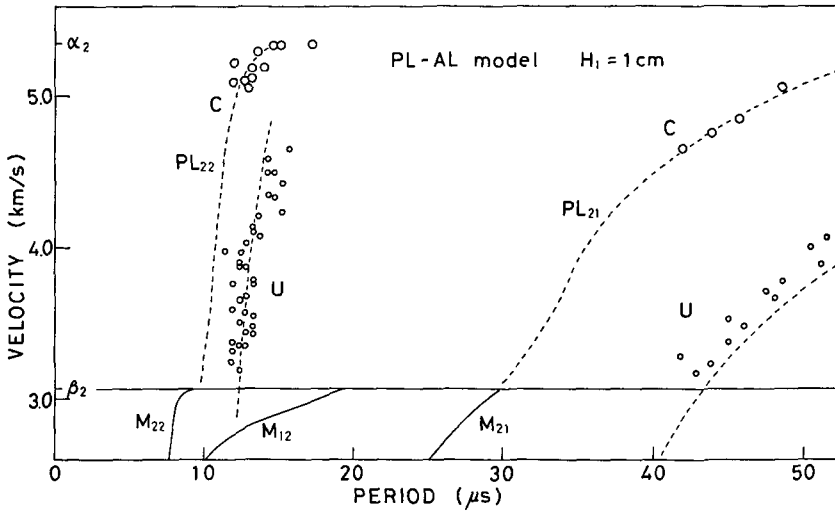


Fig. 7. Observed and theoretical dispersions of PL waves for PL-AL model.

and are compared with theoretical dispersion curves. Theoretical group velocity curves were obtained by graphic differentiation of phase velocity curves from the relation,  $U=c+k \cdot dc/dk$ . The agreement between the observed and the theoretical dispersion is very good except for the small

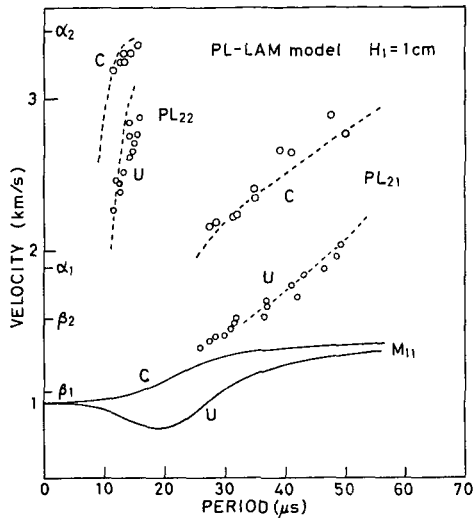


Fig. 8. Observed and theoretical dispersions of PL waves for PL-LAM model.

discrepancy of  $PL_{21}$  group velocity. It was also confirmed that dispersed waves observed in HAMADA's model experiment were  $PL_{22}$  waves. Now, no discussion on normal modes is given in the present paper, because HAMADA made a perfect report about them.

In Fig. 8, the comparison of observed and theoretical dispersions of PL waves for PL-LAM model is represented. The minima of the period function for this model are not so sharp as those for PL-AL model. This may be due to the smaller velocity contrast between the superficial layer and the half space of this model. But the agreement between the observation and the theoretical curve is still good.

One of the major objects of this model experiment is to examine the reliability of the approximate dispersion curve for the leaking mode. As shown in this section, approximate solutions agree with experimental data very well. Of course, any approximation has its own limitation. In our leaking mode problem, approximate methods seem to be very powerful for the analysis of wave trains of the leaking mode which have large amplitude due to the small attenuation.

### 3.2 PL waves in earthquake seismograms.

#### 3.2.1 Theoretical dispersion curves.

Since the publication of OLIVER and MAJOR's paper,<sup>10)</sup> many authors

discussed PL waves in the long period seismograms<sup>24),25),11),26)</sup>. OLIVER and MAJOR calculated the dispersion curve of the PL wave for a crust-mantle model by their approximate method and compared it with observed data. This simple model has been called "OLIVER and MAJOR's model" and was also analyzed by GILBERT<sup>13)</sup> and SU and DORMAN<sup>11)</sup>. GILBERT calculated the complex roots of the period equation for this model. SU and DORMAN showed that the results from two approximate methods agree with the complex roots obtained by GILBERT.

OLIVER<sup>24)</sup> attempted to determine the velocity variation in the upper mantle from the analyses of PL waves. He could not get the good result for this problem, but obtained the variation of the crustal thickness in United States.

In this section, more complicated crustal models will be analyzed. Dispersion curves are calculated mainly by the two approximate methods. Because the computer program is written by the matrix method<sup>17)</sup> dispersion curves for rather complicated models can be calculated easily. In § 7, some comparisons of approximate solutions and complex roots for the same model will be given.

Table 2. Elastic constants of five crust-mantle models.

| Model | $\alpha_3$ (km/s) | $\beta_3$ (km/s) | $\rho_3$ (g/cm <sup>3</sup> ) | $H_1$ (km) | $H_2$ (km) |
|-------|-------------------|------------------|-------------------------------|------------|------------|
| JW-1  | 8.00              | 4.50             | 3.30                          | 15.0       | 15.0       |
| JW-1A | 7.50              | 4.20             | 3.30                          | 15.0       | 15.0       |
| JW-1B | 8.50              | 4.80             | 3.30                          | 15.0       | 15.0       |
| JW-2  | 8.00              | 4.50             | 3.30                          | 10.0       | 20.0       |
| JW-3  | 8.00              | 4.50             | 3.30                          | 20.0       | 10.0       |

$\alpha_1=6.10$ ,  $\beta_1=3.45$ ,  $\rho_1=2.77$ ,  $\alpha_2=6.60$ ,  $\beta_2=3.80$  and  $\rho_2=2.90$  in all cases.

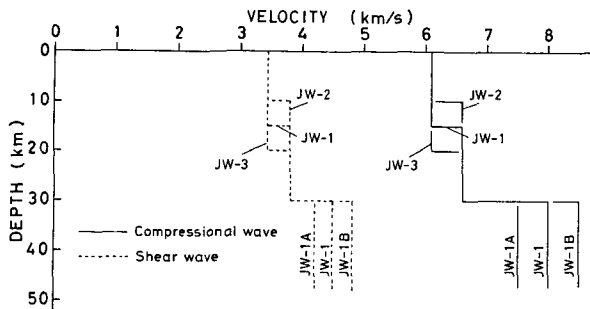


Fig. 9. Compressional and shear wave velocity distributions with depth of five crust-mantle models.

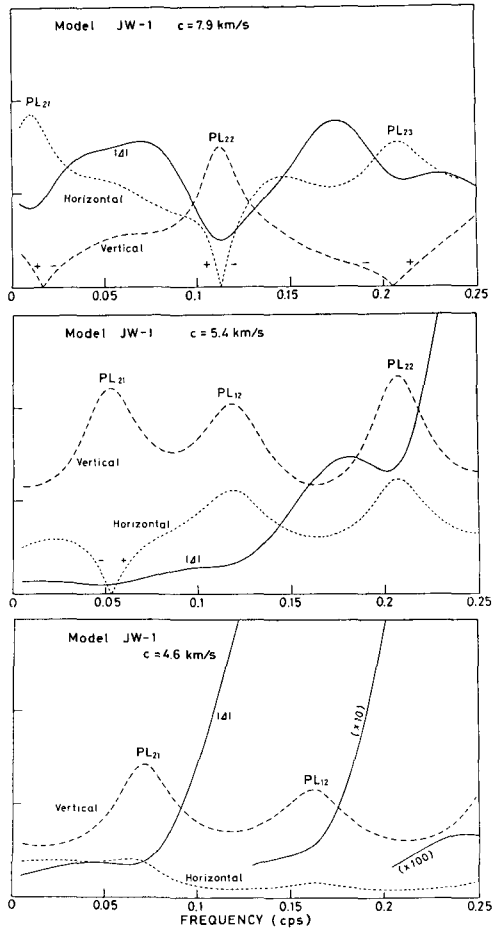


Fig. 10. Examples of computations by the two approximate methods for dispersion curves of PL waves. **Horizontal**, **Vertical** and  $|\Delta|$  are two components of surface displacement spectra and the absolute value of the period function.

At first of this section, the effect of the mantle velocity variation on dispersion of the PL wave is discussed. Three continental models (JW-1, JW-1A and JW-1B) tabulated in Table 2 are chosen for this purpose. Each model consists of two crustal layers and a half space mantle. The elastic constants of the crustal layers were determined by the present author<sup>27)</sup> in the analysis of Rayleigh waves observed in Japan. Constants of the mantle were determined tentatively for the present study. These models are exhibited also in Fig. 9.

Some computation examples by the two approximate methods for Model JW-1 are shown in Fig. 10. The phase velocities are 7.9, 5.4 and 4.6 km/s. In this figure, **Horizontal**, **Vertical** and  $|A|$  represent the horizontal and vertical spectral amplitudes and the absolute value of the period function respectively. The phase velocity of 7.9 km/s is the example which is approximately same to the compressional wave velocity in the upper mantle. Some extremes which correspond to PL<sub>21</sub>, PL<sub>22</sub> and PL<sub>23</sub> waves are recognized. When the phase velocity is 5.4 km/s, the spectrum has a clear maximum for PL<sub>12</sub> wave. But the period function shows very steep exponential increase, and the minimum for PL<sub>12</sub> wave cannot be found. The phase velocity 4.6 km/s is a little larger than the shear wave velocity in the upper mantle. Exponential increase of the period function is now very large and no sharp minimum is recognized. However, the spectra of two components have clear maxima for PL waves.

The merits of those two approximate methods are clearly compared in Fig. 10. One problem is sudden sign change of the spectrum. Sometimes, this sign change occurs near the place where any PL wave is expected to arise. The other problem is steep exponential increase in the absolute value of the period function. These "anti-symmetries" disturb the positions of the extremes.

Fig. 11 is the dispersion curves for Model JW-1. Group velocity  $U$  was determined from the relation,  $U=c+k \cdot dc/dk$ , by graphic differentiation of the phase velocity curve. This figure is very similar to Fig. 4 in SU and DORMAN's paper<sup>11)</sup>. The group velocity curve of PL<sub>22</sub> has a very steep part and its approximate period was estimated from Fig. 11 as follows,

$$T = H_c/3.8 \quad (\text{sec}) \quad (4)$$

where  $H_c$  is crustal thickness in km.

The phase velocity curves for three models, JW-1, JW-1A and JW-1B are shown in Fig. 12, where the abscissa means frequency. These models have the mantle P wave velocities of 8.0, 7.5 and 8.5 km/s respectively, and the effect of this velocity difference on the phase velocity clearly indicated in this figure. In Fig. 13, phase and group velocity curves of two principal PL waves, PL<sub>21</sub> and PL<sub>22</sub>, are given. In spite of large differences of the mantle velocity, the group velocity curves of PL<sub>21</sub> wave in shorter period are of almost coincided with each other. This result may suggest a severe limit the application of the analysis of PL wave to obtain the detailed crust-mantle structure. In general, the group velocity of PL wave has more chances to

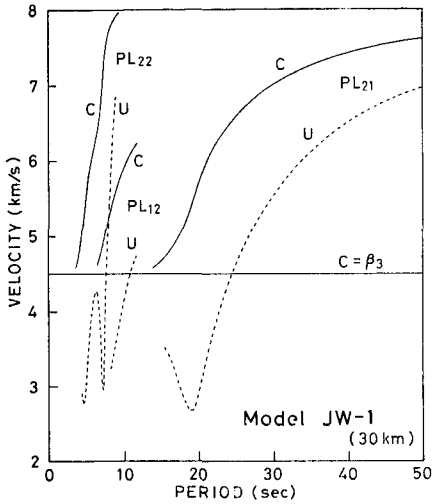


Fig. 11

Fig. 11. Dispersion curves of  $PL_{21}$ ,  $PL_{12}$  and  $PL_{22}$  waves for Model JW-1.

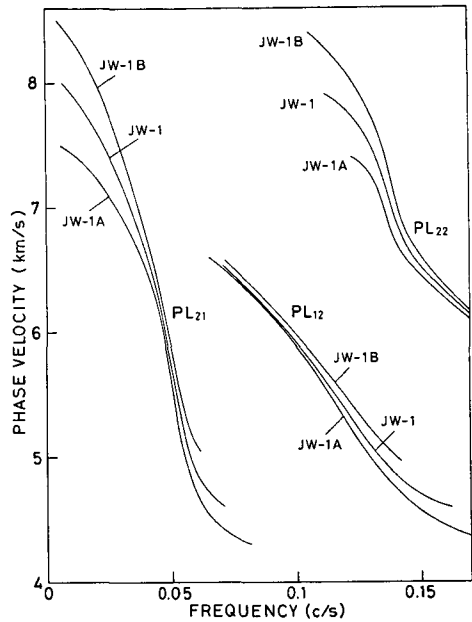


Fig. 12

Fig. 12. Phase velocity curves for three models JW-1, JW-1A and JW-1B.

be determined from observations than the phase velocity. Consequently, it seems to be very difficult to determine the accurate mantle velocity from the observation of PL wave.

Phase velocity curves of PL waves for three models, JW-1, JW-2 and JW-3 are shown in Fig. 14. They have different ratios of  $H_2/H_1$  as given in Table 2 and in Fig. 9. There are no systematic changes in these curves except for  $PL_{21}$  wave. Since these changes seem to be less than observation errors, it may be also very difficult to determine the ratio mentioned above.

Next, we discuss the effect of the shallow water layer on the dispersion curves of PL waves. Three models, JW-1WA, JW-1WB and JW-1WC were considered. These models have water layers of 1 km, 2 km and 3 km thick, respectively, and are tabulated in Table 3. The velocity distributions of compressional and shear waves with depth of Models JW-1WC and JW-1 are shown in Fig. 15. The sound velocity and the density of the water layer are 1.52 km/s and 1.02 g/cm<sup>3</sup>. The total thickness of the crust is assumed to be 30 km in all these models.

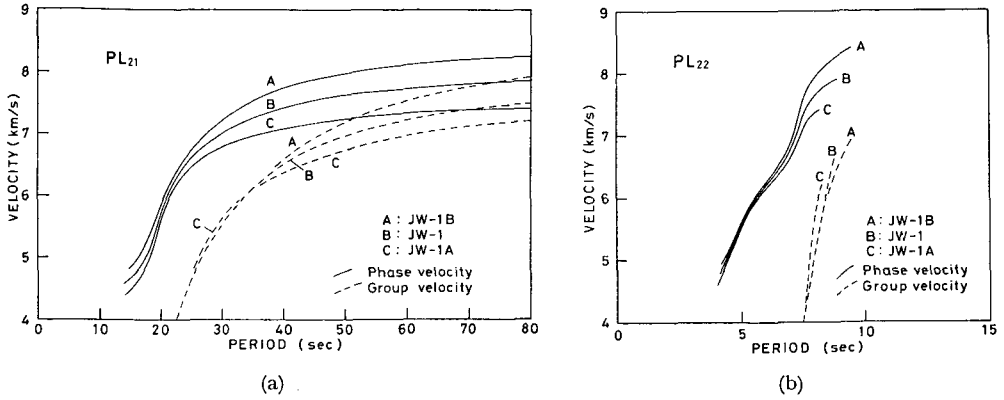


Fig. 13. Phase and group velocity curves for three models JW-1, JW-1A and JW-1B. (a)  $PL_{21}$  wave, (b)  $PL_{22}$  wave.

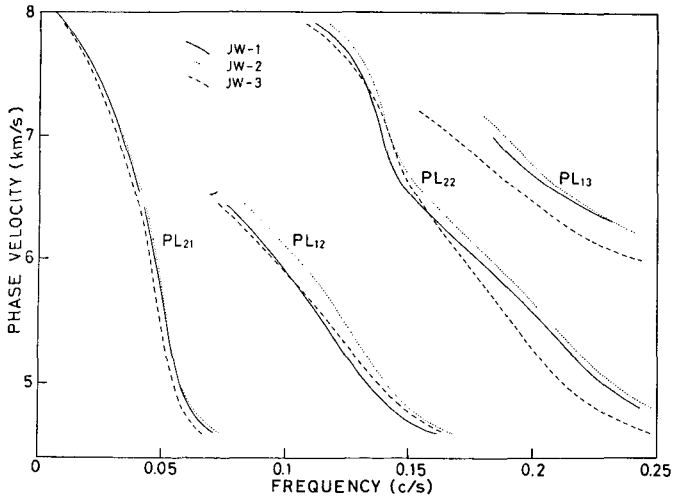


Fig. 14. Phase velocity curves for three models, JW-1, JW-2 and JW-3.

Some examples of the calculation by the approximate methods are shown in Fig. 16, where phase velocity is 6.7km/s. The upper figure represents the absolute value of the period function and the surface spectra for Model JW-1WC. At about 0.13 cps, the period function has a very sharp minimum, and the vertical component of the spectrum has an extremely large maximum. On the other hand, the horizontal component changes its sign at this point suddenly. This special frequency corresponds to a kind of resonance in the

Table 3. Elastic constants of water covered crust-mantle models.

| Layer | $\alpha$ (km/s) | $\beta$ (km/s) | $\rho$ (g/cm <sup>3</sup> ) | $H$ (km)       |
|-------|-----------------|----------------|-----------------------------|----------------|
| 1     | 1.52            | —              | 1.02                        | $H_1$          |
| 2     | 6.10            | 3.45           | 2.77                        | $(15.0 - H_1)$ |
| 3     | 6.60            | 3.80           | 2.90                        | 15.0           |
| 4     | 8.00            | 4.50           | 3.30                        | INF.           |

Model JW-1WA;  $H_1=1.0$ (km), Model JW-1WB:  $H_1=2.0$ , Model JW-1WC;  $H_1=3.0$ .

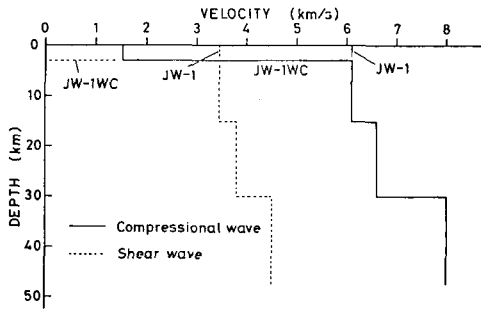


Fig. 15

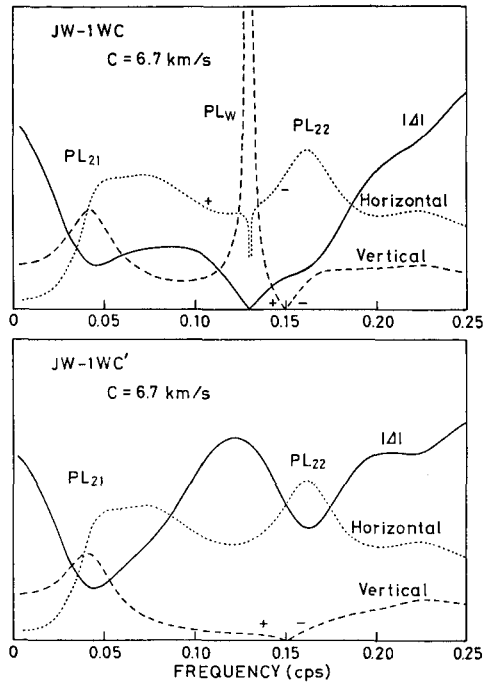


Fig. 16

Fig. 15. Velocity distributions of compressional and shear waves of models JW-1 and JW-1WC. Other two models have almost same velocity distributions except for the thickness of the water layer.

Fig. 16. Examples of computation by two approximate methods. Upper; Model JW-1WC, Lower; Model JW-1WC'. Phase velocity is 6.7 km/s.

water layer. OLIVER and MAJOR<sup>10)</sup> have proposed an equation for this phenomenon,

$$kH_1 = \frac{\pi(2n-1) + 2\epsilon}{2(c^2/\alpha_1^2 - 1)^{1/2}} \tag{5}$$

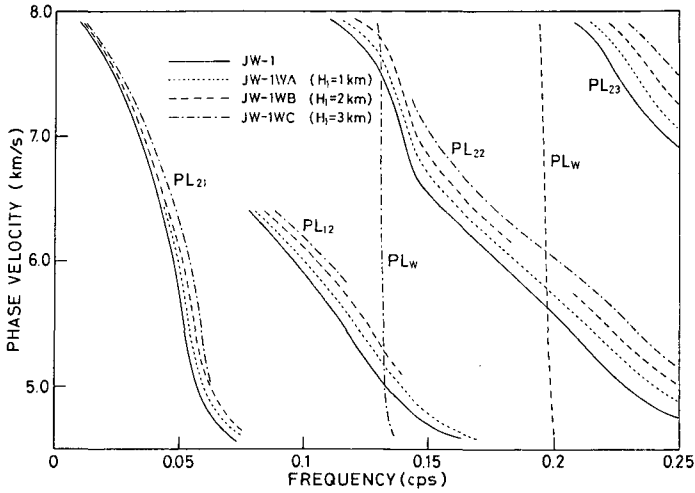


Fig. 17. Phase velocity curves for models JW-1, JW-1WA, JW-1WB and JW-1WC.

where  $2\epsilon$  is phase shift of the compressional wave reflecting on the liquid-solid interface. In the present paper, the wave train corresponding to this special frequency is called  $PL_w$  wave.

The lower figure of Fig. 16 is the similar example for Model JW-1WC'. This model has no water layers but the other portions are exactly same to those of Model JW-1WC. From two figures in Fig. 16, it is soon recognized that the horizontal component of the spectrum is not disturbed by existence

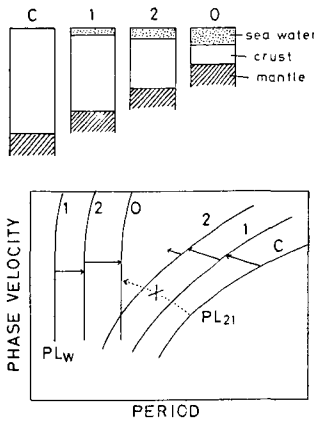


Fig. 18. Schematic representation of transition from continental PL wave to oceanic PL wave.

of the water layer except for the sudden change of its sign at the frequency which corresponds to  $PL_w$  wave. This result suggests the decoupling of the horizontal motion on the liquid-solid interface, and the dispersion curve of PL wave except for  $PL_w$  wave may be simply calculated from the model with no water layer.

In Fig. 17, the dispersion curves of PL waves for Models JW-1, JW-1WA, JW-1WB and JW-1WC are illustrated. It is soon understood that the thicker the water layer, the lower the frequency of  $PL_w$  wave. On the other hand, other PL waves, such as  $PL_{21}$  have opposite trend because of the thickness of the "solid" crust. From Fig. 17, the approximate frequency of  $PL_w$  wave can be determined graphically as follows,

$$f = 1/T = 1/(2.5 \times H_1) \quad (\text{cps}) \quad (6)$$

where  $H_1$  is the thickness of the water layer in km.

Transition from continental PL wave to oceanic PL wave is schematically illustrated in Fig. 18. CHANDER (personal communication) has shown some records of shear-coupled PL wave named by OLIVER<sup>24)</sup> which has periods as long as 40 seconds and propagated along the sub-oceanic path. The present author has such an opinion that shear-coupled PL wave is possible to have such long periods if it is not  $PL_w$  but  $PL_{21}$ . Sometimes, the transition of PL waves from continental to oceanic has been recognized as indicated by a dotted line in Fig. 18, but it does not seem to be true.

### 3.2.2. Analyses of observed PL waves.

It has been shown that the long period vibration was recognized on the record near the initial motion of the great earthquake<sup>28)</sup>. MATUZAWA<sup>29)</sup> explained that this vibration is not the leaking mode but a kind of body

Table 4. List of the earthquakes.

| No. | Earthquake         | Date          | Epicentre |        | Obs. pt. | $d(\text{km})$ | Instrument |      |
|-----|--------------------|---------------|-----------|--------|----------|----------------|------------|------|
|     |                    |               | N         | E      |          |                | V          | H    |
| 1   | Tajima             | May 23, 1925  | 35.6°     | 134.8° | T        | 455            | A          | B, G |
| 2   | Tango              | March 7, 1927 | 35.6      | 135.1  | T        | 427            | A, C       | B    |
|     |                    |               |           |        | K        | 410            | A'         | B    |
| 3   | E off Aomori Pref. | March 9, 1931 | 41.2      | 142.5  | T        | 450            | D          | E    |
| 4   | Off Miyazaki Pref. | Nov. 6, 1931  | 32.2      | 132.1  | T        | 817            |            | F    |

Observation point T; Hongo (Tokyo), K; Kamakura.

Table 5. Characteristics of the seismometers.

|           | Magnification | Natural period (sec) | Damping ratio | Remarks              |
|-----------|---------------|----------------------|---------------|----------------------|
| <b>A</b>  | 2             | 10                   | 2.5           | with oil damper      |
| <b>A'</b> | 2             | 10                   | 2.0           | with oil damper      |
| <b>B</b>  | 2             | 5                    | 2.0           | with oil damper      |
| <b>C</b>  | 1.5           | 30                   | 1.6           |                      |
| <b>D</b>  | 1.5           | 50                   | 1.5           | with oil damper      |
| <b>E</b>  | 7.5           | 20                   | 3.0           | with magnetic damper |
| <b>F</b>  | 7.5           | 18                   | 2.3           |                      |
| <b>G</b>  | 10            | 12                   |               |                      |

waves. But as explained in §2 of the present paper, the leaking mode was the contribution of the pole which took the place of that of the branch line. The contribution of the integral along the branch line corresponds to the body wave. Therefore, the analysis of the leaking mode is considered as another approach to the body wave. For example, KNOPOFF et al.<sup>18)</sup> observed the predominant vibrations which correspond to  $PL_{22}$  waves in his model experiment, and attempted to explain them by the ray theory or by the superposition of many body waves.

At first, four old great earthquakes which occurred in Japan will be analyzed. These four earthquakes are tabulated in Table 4. The data about Tajima earthquake are due to MATUZAWA<sup>30)</sup>, and other data were picked up from *Catalog of Major Earthquake which occurred in and near Japan (1926-1956)* by J.M.A. All records of these earthquakes were traced from the figures in the reports which were already published. The characteristics of the seismometers indicated with **A**, **B** etc. are tabulated in Table 5.

Observation points and the epicentres of the earthquakes are shown in Fig. 19. In this figure, T and K mean the Hongo and Kamakura observation stations of the Earthquake Research Institute of Tokyo University. The propagation paths from these four earthquakes to the observation points are those of nearly continental structures.

Figs. 20(a) and (b) are traced records of Tajima earthquake in 1925 observed at Hongo. Notations P, P\*,  $\bar{P}$  etc. in these figures are the name of the peculiar phases after MATUZAWA<sup>30)</sup>. In the records of EW component of (a) and the vertical component of (b), dispersed wave trains begin from near the point indicated with P\*.

Now we must take our attention to the characteristics of the seismometers which were used in the observation. As shown in Table 5, the natural

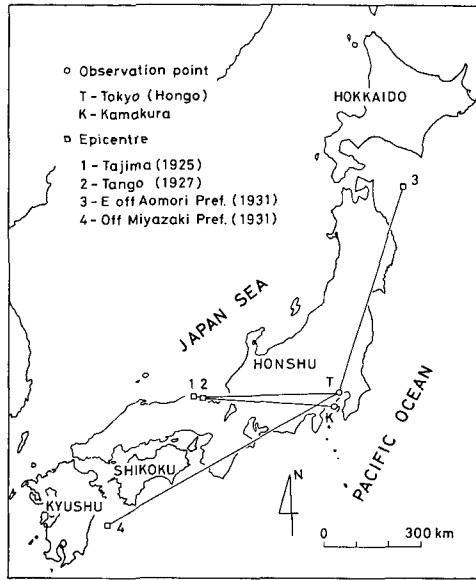


Fig. 19. Observation points and the epicentres of the earthquakes No. 1-No. 4.

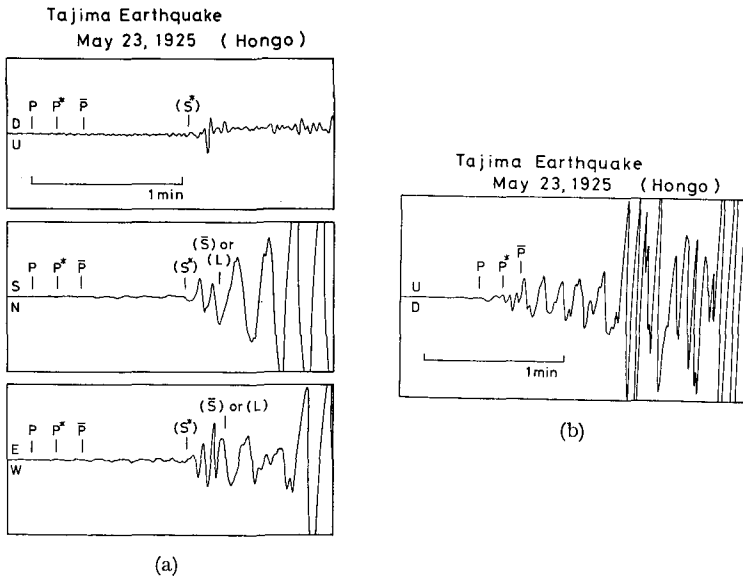


Fig. 20. Traced records of Tajima earthquake observed at Hongo.

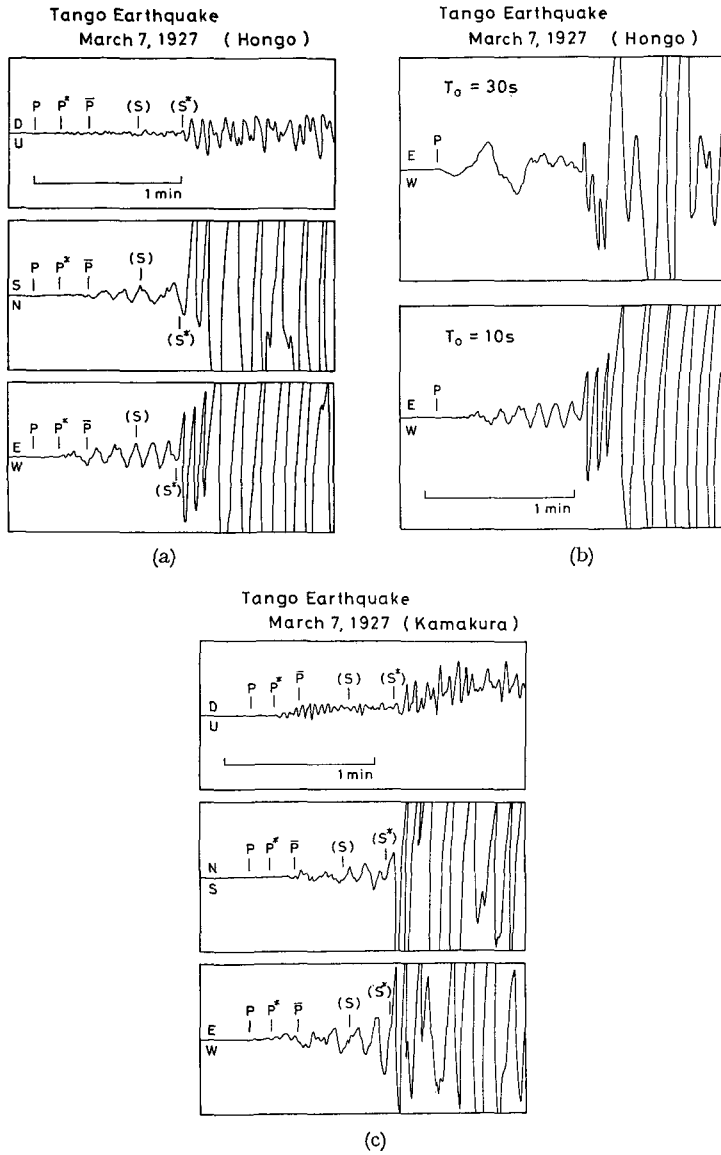


Fig. 21. Traced records of Tango earthquake observed at Hongo and Kamakura.

period of the seismometer **A** which recorded the EW component record of figure (a) is about 10 seconds and is not so longer than period of observed waves, 7-8 seconds. Moreover, the damping ratio of the pendulum is not

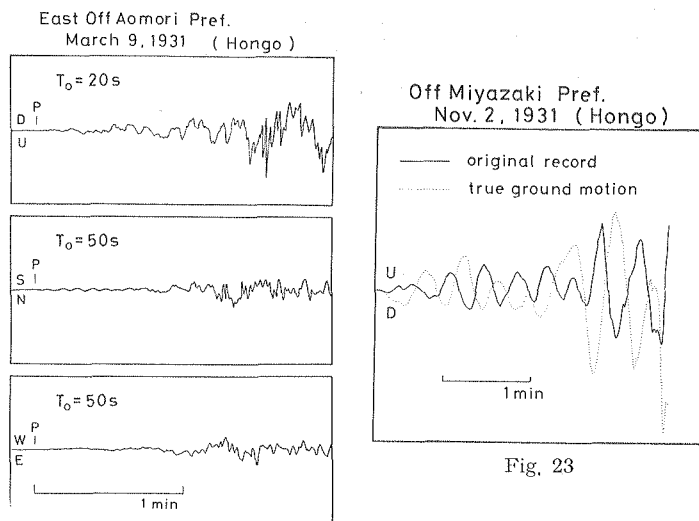


Fig. 22

Fig. 22. Traced records of the earthquake of East off Aomori Pref. observed at Hongo.

Fig. 23. Seismogram of the earthquake of Off Miyazaki Pref. observed at Hongo. The trace of a dotted line is the true ground motion computed by KAWASUMI.

enough. But the period of this wave train is same to that in figure (b) which was recorded by seismometer **G**. The natural period of this seismometer is about 12 seconds.

No predominant dispersed waves were found in the vertical component record in figure (a). It may be because of the rather shorter natural period of the pendulum. In all records of Fig. 20, many dispersed wave trains can be pointed out after the S arrival. They must be Love waves, Rayleigh waves and their higher modes, though they are not analyzed in the present study.

Figs. 21 (a), (b) and (c) are the records of Tango earthquake in 1927 observed at Hongo and Kamakura. These records were observed by IMAMURA's strong motion seismometer<sup>31</sup>). In the horizontal components of figure (a), very beautiful dispersed waves can be found between P and S arrivals. The periods of these wave trains are again 7-8 seconds.

The upper figure of (b) is the record obtained by a seismometer whose natural period is about 30 seconds. Large vibrations of long periods, about 24 seconds, are recognized but it must be noticed that the damping ratio of this seismometer was also very small. The lower figure is same to EW component

in figure (a). From the comparison of these figure, we can also find the shorter period vibration superposing on the longer period one in the upper figure. If it is true, this figure suggests that the shorter period vibration, about 7–8 seconds, is not due to the smaller damping ratio of the seismometer, but indicates the true information of the propagating wave. Figure (c) shows the records observed at Kamakura. The same vibration which was found in figure (b) can also be found in this figure. But the record of EW component seems to be disturbed by something, and the period is not exactly same to that of the other records.

Traced records of the earthquake of East off Aomori Prefecture in 1931 observed at Hongo are shown in Fig. 22. In the records of vertical and NS components, small but beautiful vibrations can be recognized. The period of this vibration is about 6 seconds and is very small compared with the natural period of the seismometer.

Fig. 23 is the record of the earthquake of Off Miyazaki Prefecture in 1931 observed at Hongo. The trace of a solid line is the original record and that of a dotted line is the true ground motion after KAWASUMI<sup>32)</sup>. He obtained this true ground motion by means of numerical integration. In both records, a dispersed wave train with periods of 20–30 seconds can be found clearly.

Now, we are going to compute the group velocity from these records. But there is a big problem about “time”. In all these old observations, the accuracy of time of the record was not so good, and the origin time of the earthquake could not be determined exactly. In the present study, the arrival times of initial P waves were fixed from the epicentral distances by the travel time table by WADATI, SAGISAKA and MASUDA<sup>33)</sup> and the group velocity was computed by using “relative time”. The accuracy of determination of initial P arrivals by this method may be about  $\pm 2$  seconds. Consequently, the group velocities obtained have the accuracy of about  $\pm 3\%$ .

Group velocities from the records of Tajima and Tango earthquakes by the method mentioned above are plotted with various marks in Fig. 24. Because the paths from both epicentres to the observation points are almost same, the group velocities obtained are well concentrated in a narrow region. Solid lines in this figure are theoretical group velocity curves of PL<sub>22</sub> wave for Model JW-1. The thickness of the crust is found to be 30 to 35 km. This result agrees very well with the crustal thickness obtained from the dispersion of Rayleigh waves<sup>34)</sup> as well as from the gravity analysis<sup>35)</sup>.

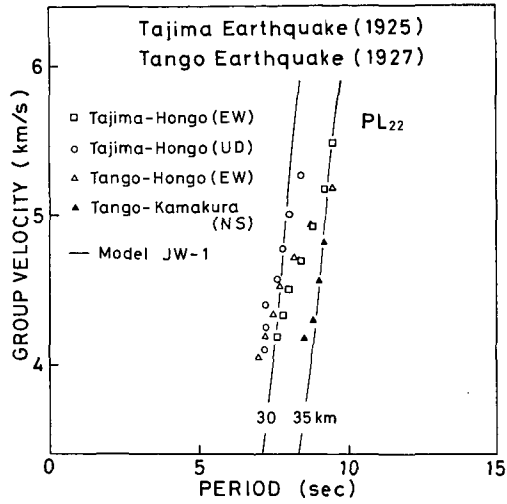


Fig. 24. Observed group velocities from the records of Tajima and Tango earthquakes. Solid lines are theoretical dispersion curves of  $PL_{22}$  wave for Model JW-1.

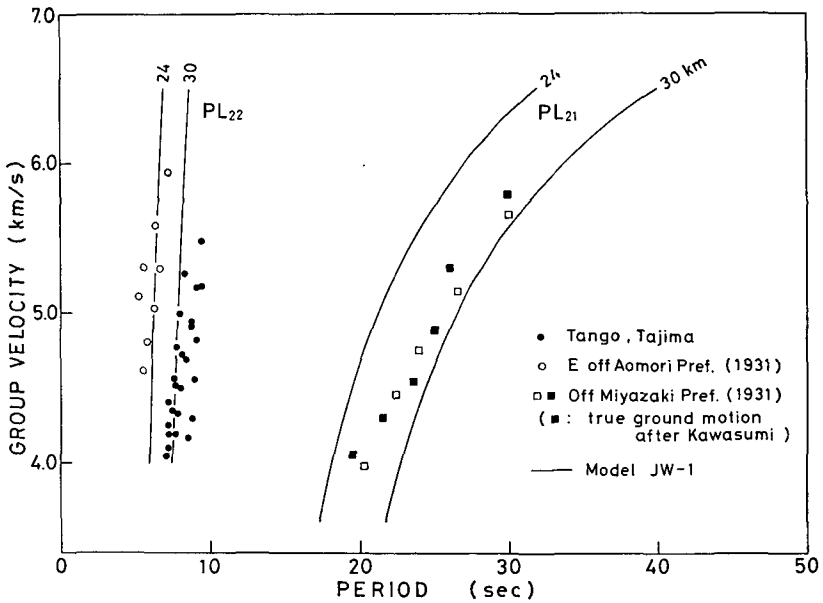


Fig. 25. Observed group velocities of four earthquakes and theoretical dispersion curves of  $PL_{21}$  and  $PL_{22}$  waves for model JW-1.

Table 6. List of the earthquakes (continued).

| No. | Earthquake               | Date          | Epicentre |         | M   | Obs. pt. | $\Delta$ (km) |
|-----|--------------------------|---------------|-----------|---------|-----|----------|---------------|
|     |                          |               | N         | E       |     |          |               |
| 5   | Off E Coast of Hokkaido  | Feb. 15, 1961 | 43°16'    | 147°56' | 6.3 | M        | 1030          |
| 6   | Off SE Coast of Hokkaido | Feb. 21, 1962 | 42 46     | 145 13  |     | M        | 849           |
| 7   | Off Etorofu Is.          | Nov. 16, 1963 | 43 32     | 149 04  | 6.2 | N        | 283           |
| 8   | Off SE Coast of Hokkaido | Nov. 12, 1966 | 41 37     | 144 26  | 5.9 | S        | 301           |
| 9   | Off Kinkazan             | Jan. 17, 1967 | 38 15     | 142 05  | 6.3 | S        | 537           |
| 10  | Hyuganada (A)            | April 1, 1968 | 32 18     | 132 23  | 6.3 | M        | 835           |
| 11  | Hyuganada (B)            | Nov. 14, 1968 | 31 32     | 131 53  | 5.3 | M        | 923           |

Observation point M; Mt. Tsukuba, S; Sapporo, N; Memuro.

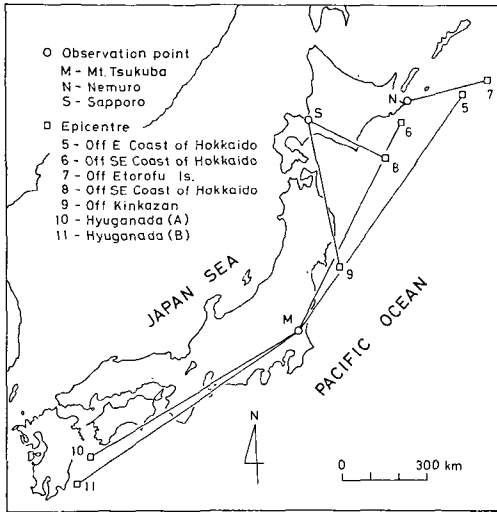


Fig. 26

Fig. 26. Observation points and the epicentres of earthquakes No. 5-No. 11.

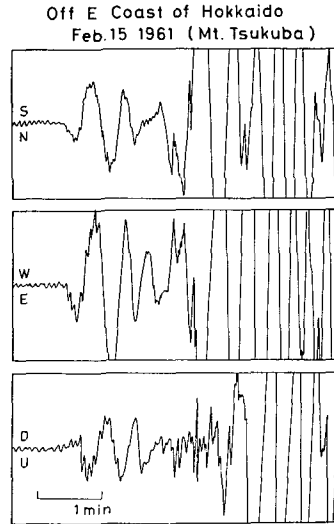


Fig. 27

Fig. 27. Traced records of the earthquake of Off E coast of Hokkaido observed at Mt. Tsukuba.

In Fig. 25, observed group velocities obtained from the records of four earthquakes are compared with the theoretical curves of  $PL_{21}$  and  $PL_{22}$  waves for Model JW-1. For the earthquake of Off Miyazaki Prefecture, group velocities were obtained from both the original record and the true ground motion. The group velocity of this wave train fits to the theoretical curve of

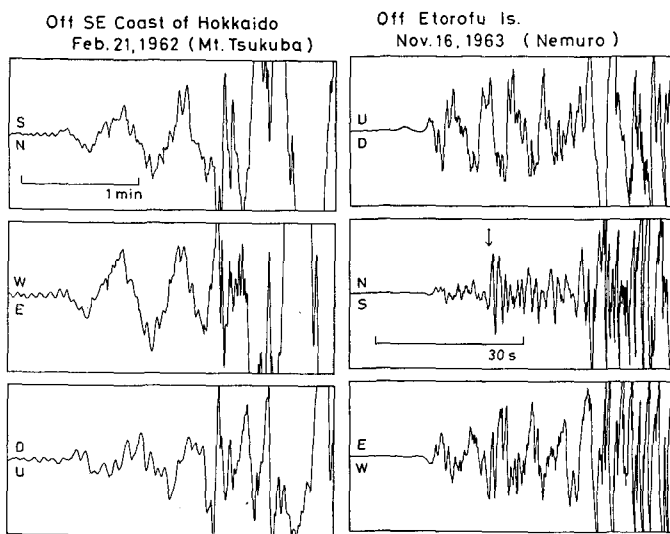


Fig. 28

Fig. 29

Fig. 28. Traced records of the earthquake of Off SE coast of Hokkaido observed at Mt. Tsukuba.

Fig. 29. Traced records of the earthquake of Off Etorofu Island observed at Nemuro.

PL<sub>21</sub> wave for Model JW-1 whose crustal thickness is assumed to be 28 km.

Open circles in Fig. 25 are the group velocities from the earthquake of Off Aomori Prefecture. These group velocities fit to the theoretical curve of PL<sub>22</sub> wave for Model JW-1 whose crustal thickness is about 24 km.

Next, PL waves found in more recent records will be analyzed. Table 6 is the list of earthquakes No. 5—No. 11. Observation points are Mt. Tsukuba, Sapporo and Nemuro, and the seismometer used are the Press-Ewing long period seismometer, the portable long period seismometer by YOSHII<sup>36)</sup> and J.M.A. Type-59 seismometer respectively. These observation points and the epicentres are illustrated in Fig. 26. The data of the earthquakes tabulated in Table 6 were determined by J.M.A.

Traced records of the earthquake of Off E coast of Hokkaido observed at Mt. Tsukuba are shown in Fig. 27. The long period dispersed wave, about 30 seconds, can be found clearly, and the particle orbit of this wave train is prograde. The path from the epicentre to Mt. Tsukuba is rather sub-oceanic than continental.

Records of the earthquake of Off SE coast of Hokkaido observed at Mt. Tsukuba are shown in Fig. 28. Also a long period wave train can be

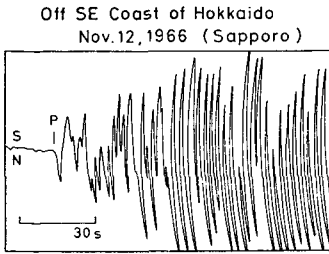


Fig. 30

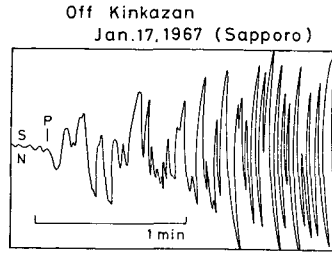


Fig. 31

Fig. 30. Traced record of the earthquake of Off SE coast of Hokkaido observed at Sapporo.

Fig. 31. Traced record of the earthquake of off Kinkazan observed at Sapporo.

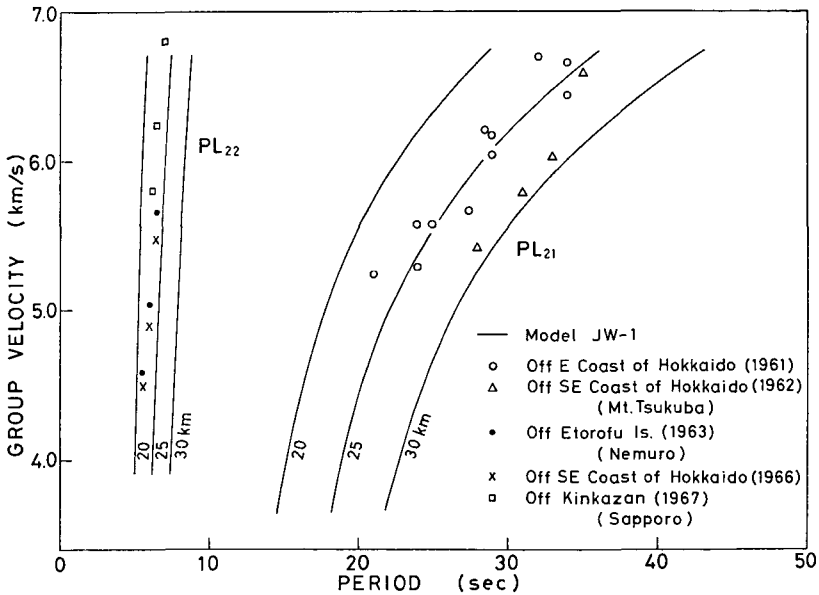


Fig. 32. Observed group velocities from the records of earthquakes No. 5-No. 9. Solid lines are theoretical dispersion curves of  $PL_{21}$  and  $PL_{22}$  waves for Model JW-1.

found. The particle orbit of this wave is prograde.

Records of the earthquake of Off Etorofu Island observed at Nemuro by J.M.A. Type-59 seismometer are given in Fig. 29. Rather short period dispersed waves can be found between P and S waves. In this case, the particle orbit is retrograde. We can find a strange phase indicated by a small

arrow in the record of NS component about 12 seconds after the initial P arrival. This component is almost transversal to the wave path as shown in Fig. 26. It is not clear why such a strange phase appeared at this position.

Fig. 30 is a record of the earthquake of Off SE coast of Hokkaido observed at Sapporo. Between P and S waves, we can find two kinds of vibrations having longer and shorter periods. The former has not enough wave numbers for the dispersion analysis.

Fig. 31 is a record of the earthquake of Off Kinkazan observed at Sapporo. The appearance of the record is very similar to that of the record in Fig. 30. The shorter period wave train can be recognized more clearly.

In Fig. 32, group velocities obtained from these five earthquakes are shown together with the theoretical dispersion curves of PL waves for Model JW-1. Group velocities from the earthquakes of Off Etorofu Island, Off SE coast of Hokkaido and Off Kinkazan correspond to those of PL<sub>22</sub> waves and crustal thicknesses determined are about 20–25 km in all these cases.

Open circles and open triangles in Fig. 32 are the group velocities from the earthquakes of Off E coast of Hokkaido and Off SE coast of Hokkaido observed at Mt. Tsukuba. The crustal thickness estimated from the group velocity of PL<sub>21</sub> wave is about 26 km and this value is somewhat too large to be compared with the other investigations. The present author thinks that these wave trains have not enough wave numbers to get the accurate group velocity.

Figs. 33 (a) and (b) are records of the aftershocks of Hyuganada earthquake in 1968 observed at Mt. Tsukuba. As shown in Fig. 26 and Fig. 19, the propagation paths from these two epicentres to the observation point are very similar to that in the case of the earthquake of Off Miyazaki Prefecture in 1931. Actually, it is soon recognized that the records of Figs. 33(a) and (b) have the almost same appearance to the record of Fig. 23. The particle orbit is also prograde.

Fig. 34 is the comparison of observed and theoretical group velocities. Solid circles are group velocities from the records of Fig. 23. Theoretical dispersion curves are again those for Model JW-1. Observed data fit well to the dispersion curve of PL<sub>21</sub> wave for Model JW-1 whose crustal thickness is about 28 km.

In the analyses of earthquakes No. 5–No. 11, epicentres and origin times used were taken from the catalog by J.M.A., and group velocities obtained are more reliable than those of earthquakes No. 1–No. 4.

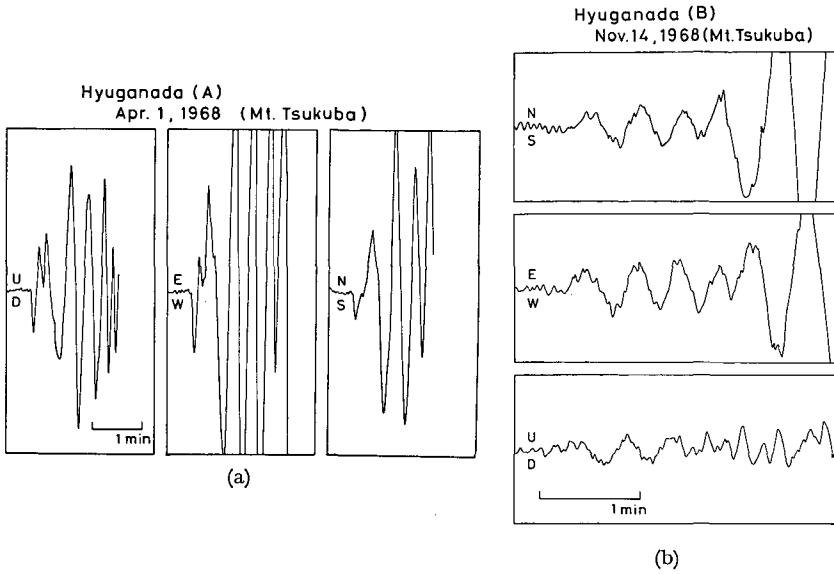


Fig. 33. Traced records of two Hyuganada earthquakes.

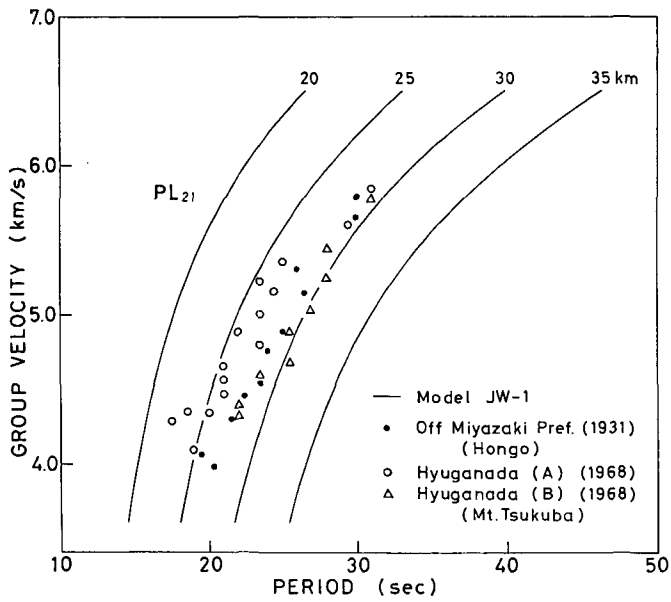


Fig. 34. Group velocities obtained from the records of two Hyuganada earthquakes. Solid lines are theoretical dispersion curves of PL<sub>21</sub> wave for Model JW-1.

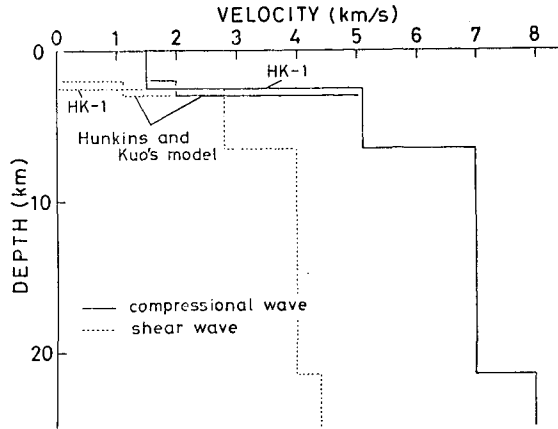


Fig. 35. Velocity distributions of HUNKINS and KUO's model and a simplified model HK-1.

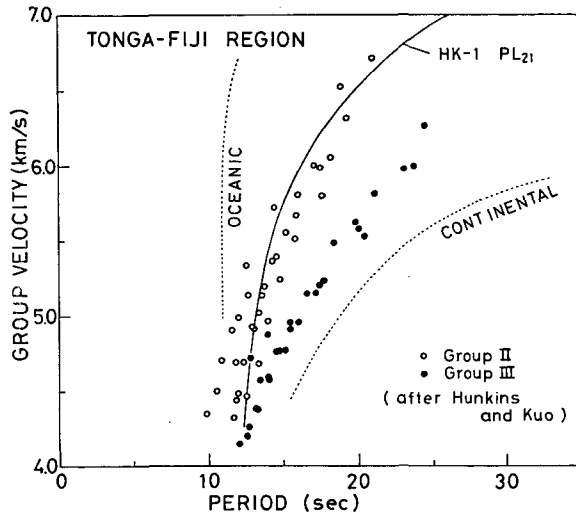


Fig. 36. Comparison of observed and theoretical group velocities of PL waves observed in Tonga-Fiji region. Solid line is the theoretical curve of  $PL_{21}$  wave for Model HK-1.

At last in this section, we will discuss the PL wave described by HUNKINS and KUO<sup>37)</sup>. They discussed Rayleigh, Love and PL waves observed at Suva, Fiji Island. They divided Tonga-Fiji region into five groups according to the dispersion of the surface waves. They exhibited a crust-mantle structure obtained from the analyses of Love and Rayleigh waves for the wave path of

Group V. Observed group velocities of PL waves for Groups II and III were given in their paper but no theoretical calculations have been shown.

Considering the dispersion of Love and Rayleigh waves, we can understand that Group II is similar to Group V. In Fig. 35, HUNKINS and KUO's model for the wave path of Group V is transcribed. The present author computed the dispersion curve of PL wave for Model HK-1 which is illustrated in Fig. 35.

The comparison of observed and theoretical dispersions is given in Fig. 36. The theoretical group velocity of  $PL_{21}$  wave for Model HK-1 fits to the observed data for Group II very well. It is very important that this theoretical curve is not of  $PL_w$  wave but of  $PL_{21}$  wave as shown in Fig. 18. Model HK-1 has the solid crust of about 19 km thick. The theoretical curve for a model which has the solid crust of about 22 km thick may fit to the observed data for Group III.

#### 4. Propagation of surface waves on the model having a high velocity layer.

##### 4.1. Theoretical dispersion curves.

Propagation of surface waves on the special model which has a high velocity layer is a very interesting problem, because the usual technique of seismic prospecting is often invalid in such a case. This situation can be easily recognized from the simple ray theory.

At first, five models in which high velocity layers are sandwiched will be discussed. As shown in Fig. 37, these models are composed of plastics, aluminium and Lamiverre plates and are called PAL-models in this paper. Thickness ratios  $H_2/H_1$  of two layers within five PAL-models, PAL-02, PAL-05, PAL-1, PAL-2 and PAL-5 are 0.2, 0.5, 1.0, 2.0 and 5.0 respectively. The elastic constants of plastics, aluminum and Lamiverre plates were given already in Table 1.

As illustrated in Fig. 37, two limits of  $H_2/H_1 \rightarrow 0$  and  $H_2/H_1 \rightarrow \infty$  correspond respectively to PL-LAM and PL-AL models. Dispersion curves of Rayleigh waves for these two models can be easily calculated. In Fig. 38, phase velocity curves of  $M_{11}$  wave for PL-LAM and PL-AL models are given. When the ratio  $H_2/H_1$  increases from zero to infinity, the dispersion curve for PAL-model may leave from that for PL-LAM model and approach to that for PL-AL model. In this case, shear wave velocity  $\beta_3$  in the half space is less than that in the second layer. Therefore, the period equation  $\Delta=0$  has no real roots in the region of  $c > \beta_3$ . The surface wave in this region must

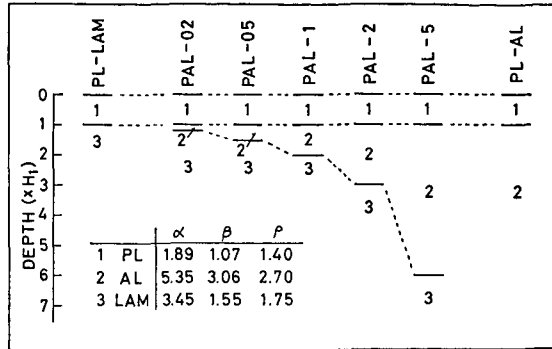


Fig. 37. Schematic diagram of five PAL-models.

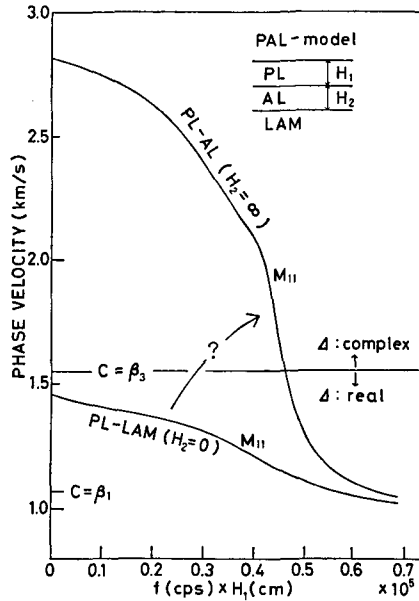


Fig. 38. Transition of the dispersion curve from PL-LAM model to PL-AL model.

be a kind of leaking modes.

Dispersion curves of the leaking mode for PAL-models were calculated by OLIVER and MAJOR's method and are represented in Fig. 39. The dispersion curve for PAL-10 ( $H_2/H_1=10.0$ ) is also shown. Dashed lines represent the leaking mode, and solid and chain lines represent the normal modes. In the high frequency region, dispersion curves for PAL-models are

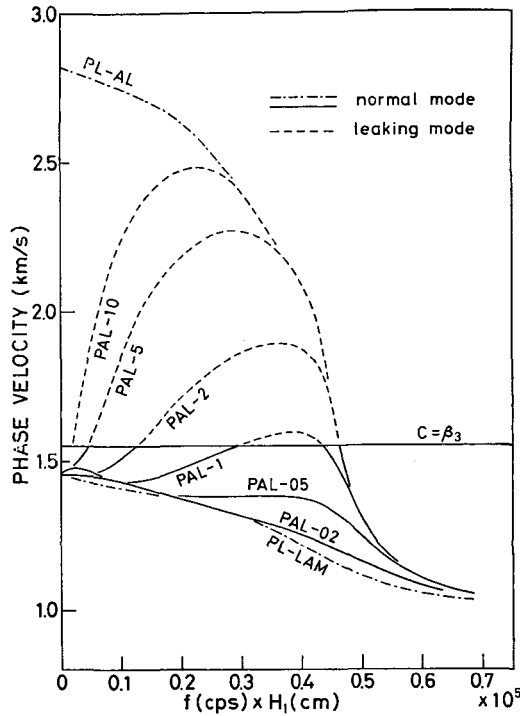


Fig. 39. Phase velocity curves for PAL-models. Dashed lines are the phase velocity curves of the leaking mode obtained by the approximate method.

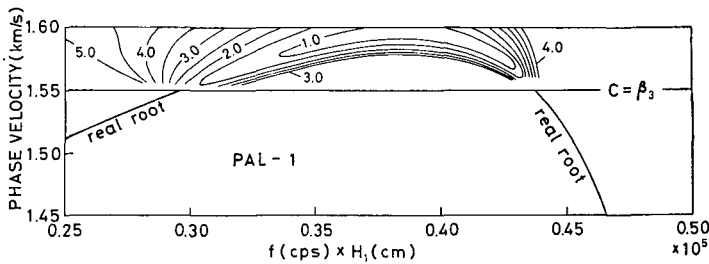


Fig. 40. Relation between the dispersion curves of leaking and normal modes for PAL-1. Contour lines in the region of  $c > \beta_3$  represent the absolute value of the period function.

very close to that for PL-AL model. These phase velocity curves have very strange features which have maxima and minima. The low frequency portion of the normal mode is also very complicated, though it is simplified in

Table 7. Elastic constants of PAL-1A.

| Layer     | $\alpha$ (km/s) | $\beta$ (km/s) | $\rho$ (g/cm <sup>3</sup> ) | Layer thickness |
|-----------|-----------------|----------------|-----------------------------|-----------------|
| Plastics  | 1.89            | 1.07           | 1.40                        | $H_1$           |
| Aluminum  | 5.35            | 3.06           | 2.70                        | $H_1$           |
| Lamiverre | 3.45            | 1.55           | 1.75                        | $4 \times H_1$  |
| (assumed) | 2.79            | 1.61           | 2.20                        | INF             |

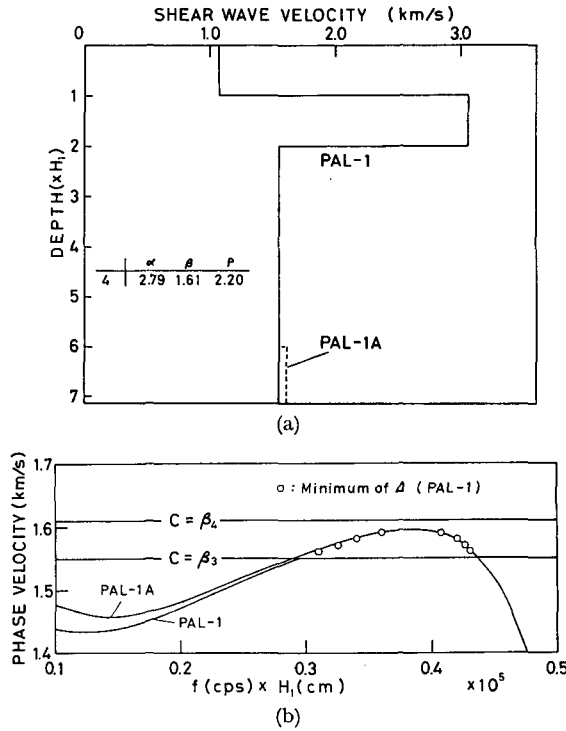


Fig. 41. (a) Shear wave distribution of PAL-1A.  
 (b) Comparison of phase velocity curves for PAL-1 and PAL-1A. Open circles indicate positions of minima of the period function for PAL-1.

this figure. This portion will be represented later in more detail (Fig. 43). The dispersion curves for PAL-1, PAL-2, PAL-5 and PAL-10 have two transition parts from normal to leaking modes. The transitions of the higher frequency sides are very smooth, but the sudden changes of the gradient of the dispersion curves are found at the lower frequency sides.

The transition from the normal mode to the leaking mode for PAL-1 is shown in Fig. 40. In the region of  $c > \beta_3$ , the absolute value of the period func-

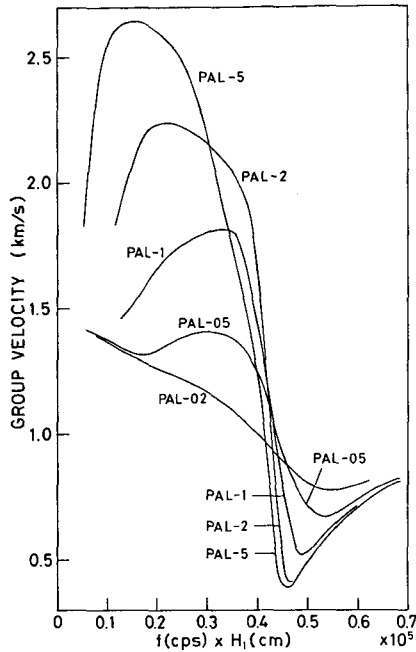


Fig. 42. Group velocity curves for five PAL-models.

tion is given by contour lines. Heavy solid lines in  $c \leq \beta_3$  are real roots of the period equation. We can find a very sharp “trough” of the period function in  $c > \beta_3$  and this trough seems to be connected smoothly to the dispersion curves of the real root. Now, we must pay attention to the fact that the dispersion curve discussed here is that of the “fundamental” mode. Since this mode may be the most important one, other “higher” modes were not discussed.

In Figs. 41 (a) and (b), the other proof of reliability of the approximate dispersion curve for the leaking mode is shown. A new model PAL-1A has a half space in which shear wave velocity is a little larger than that in Lamiverre. The detail of this model is shown in Fig. 41 (a) and in Table 7. It is expected that the difference between phase velocities for PAL-1 and PAL-1A will be very small except in the lower frequency region. It is also expected that whole dispersion curve of “fundamental” mode for PAL-1A will be included in the normal mode region, because shear wave velocity in the half space is larger than that of a layer just above. The phase velocity curve for PAL-1A is shown in Fig. 41 (b). In the region of  $\beta_3 < c < \beta_4$ , the normal mode solution

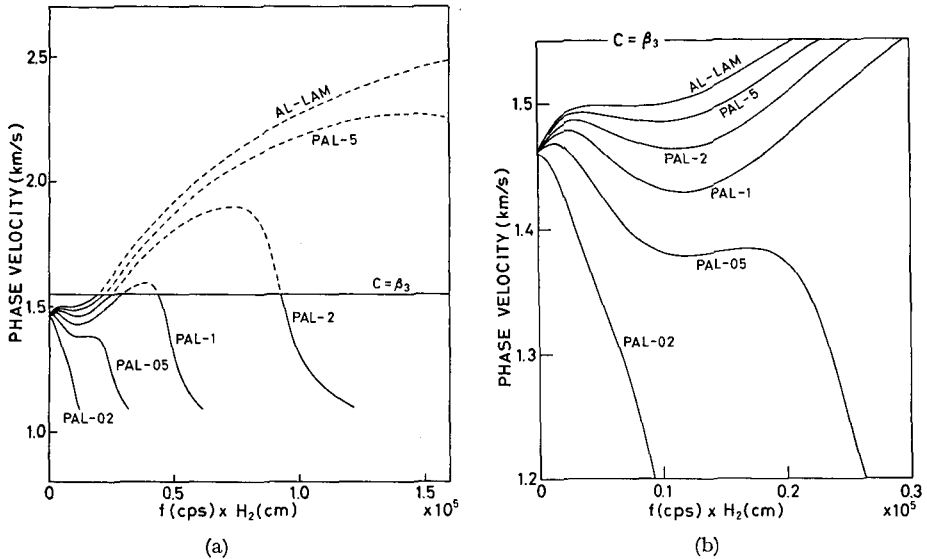


Fig. 43. (a) Phase velocity curves for PAL-models. The abscissa of this figure is normalized to  $H_2$ . The phase velocity curve for AL-LAM model is also shown.

(b) Low frequency portion of figure (a) is magnified. Only normal modes are shown.

for PAL-1A is very close to the minimum of the period function for PAL-1. This result suggests high reliability of the approximate method for the present problem. The comparison of approximate solutions and complex roots of the period equation will be given in § 7 of this paper.

Group velocity curves for PAL-models are illustrated in Fig. 42. These curves have very complicated appearances because of maxima and minima of the phase velocity curves. The group velocity has the higher value than the phase velocity in the region where the phase velocity has a characteristic of "inverse dispersion".

Fig. 43 (a) illustrates the phase velocity curves for PAL-models and is essentially equivalent to Fig. 39, but the abscissa is normalized to  $H_2$ . If  $H_2$  is not infinitely large, the limit of  $H_2/H_1 \rightarrow \infty$  correspond to AL-LAM model. As shown in this figure, when the ratio  $H_2/H_1$  increases, the phase velocity for PAL-model approaches to that for AL-LAM model, gradually. The low frequency portion of normal modes is shown very clearly now. This portion is magnified in Fig. 43 (b).

AL-LAM model is another simple example of the "high velocity layer

Table 8. Elastic constants of five high velocity layer models.

| Model | $\alpha_1/\beta_2$ | $\alpha_2/\beta_2$ | $\beta_1/\beta_2$ | $\rho_1/\rho_2$ |
|-------|--------------------|--------------------|-------------------|-----------------|
| H-125 | 2,165              | 1,732              | 1,250             | 1,118           |
| H-150 | 2,598              | 1,732              | 1,500             | 1,225           |
| H-200 | 3,464              | 1,732              | 2,000             | 1,414           |
| H-250 | 4,330              | 1,732              | 2,500             | 1,581           |
| H-300 | 5,196              | 1,732              | 3,000             | 1,732           |

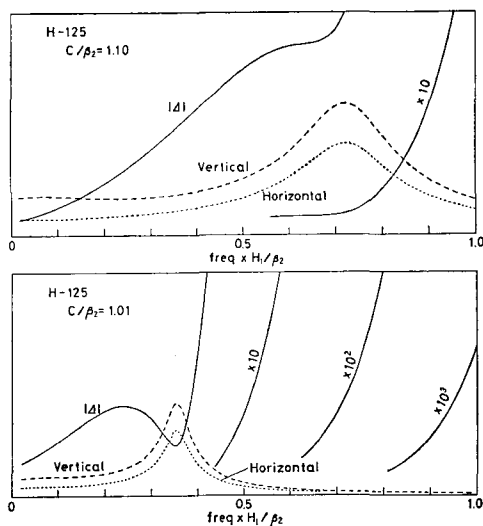


Fig. 44. Examples of the calculation by two approximate methods for Model H-125. **Vertical, Horizontal** and  $|d|$  are the two components of the surface spectrum and the absolute value of the period function.

model". Its surface layer has the higher velocity than the half space medium. Next, general characteristics of the wave in the model of this type will be discussed.

Elastic constants of five high velocity layer models discussed are listed in Table 8. The velocity contrasts of the surface layer and the half space for these models are 1.25, 1.5, 2.0, 2.5 and 3.0 respectively. All the velocities are normalized to  $\beta_2$ , because this is the critical velocity between normal and leaking modes. The density contrast  $\rho_1/\rho_2$  is tentatively assumed as the square root of the velocity contrast in all cases. Poisson's ratios in all these media are 0.25.

Calculations of dispersion curves were carried out by using OLIVER and MAJOR's and SU and DORMAN's methods. Better results were obtained

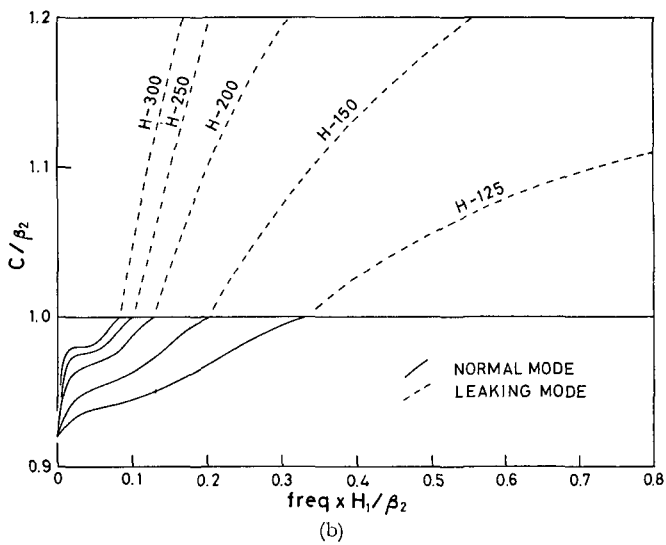
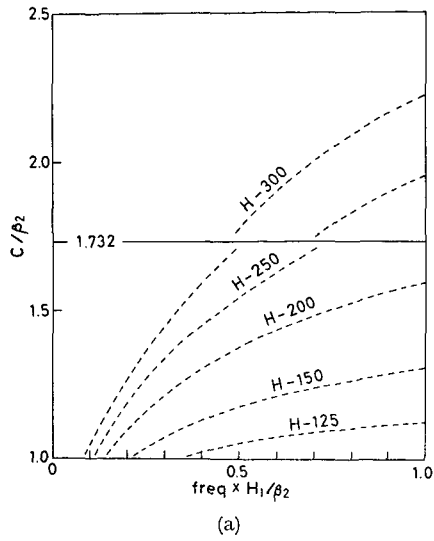


Fig. 45. (a) Phase velocity curves of leaking modes for five high velocity layer models. The phase velocity  $c=1.732 \times \beta_2$  corresponds to the compressional wave velocity in the half space.  
 (b) Phase velocity curves which show connections between normal and leaking modes.

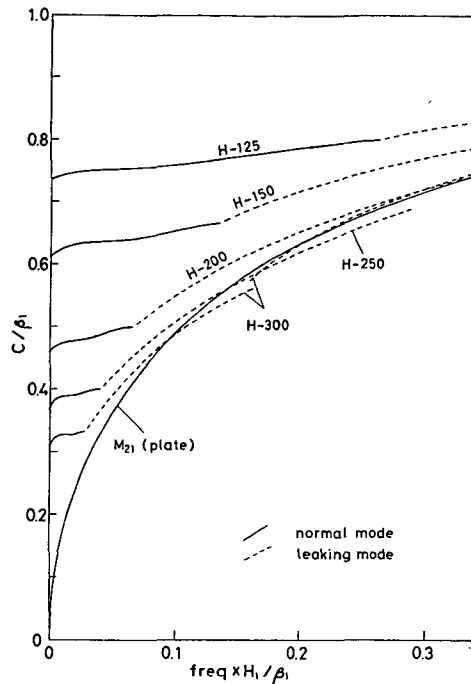


Fig. 46. Phase velocity curves for high velocity layer models. The ordinate and abscissa of this figure are normalized to  $\beta_1$ . The phase velocity curve of  $M_{21}$  mode for a "plate" model is also shown for comparison.

by the latter method, because the former one was disturbed by steep exponential increase of the period function. This situation is illustrated in Fig. 44. When the absolute value of the period function suffers from steep exponential increase, the minima of it sometimes disappears.

Phase velocity curves of the leaking mode for the high velocity layer models are shown in Fig. 45 (a). These curves were obtained mainly by SU and DORMAN'S method. All these phase velocity curves have a special appearance of "inverse dispersion". Another special appearance is the discontinuity of them at  $c = 1.732 \times \beta_2$ . This velocity corresponds to  $a_2$ . Probably, the leaking mode has different natures in the region of  $c > a_2$ . In this region, not only leak of the shear wave but also that of the compressional wave may be occurred. This problem will be discussed again in § 4.2 and in § 7.

The connections between normal and leaking modes for high velocity layer

Table 9. Elastic constants of three high velocity layer models.

| Model | $a_1/\beta_2$ | $a_2/\beta_2$ | $\beta_1/\beta_2$ | $\rho_1/\rho_2$ |
|-------|---------------|---------------|-------------------|-----------------|
| HA-1  | 2.598         | 2.598         | 1.500             | 1.000           |
| HA-2  | 3.464         | 3.464         | 2.000             | 1.000           |
| HA-3  | 6.928         | 6.928         | 4.000             | 1.000           |

models are shown in Fig. 45(b). This feature is very similar to that of AL-LAM model in Fig. 43 (a). Again the gradients of the phase velocity curves of the normal modes at  $c=\beta_2$  seem to be different from those of the leaking modes. All dispersion curves for these models converge into a point when the frequency approaches to zero. This velocity,  $c=0.9194\times\beta_2$ , corresponds to the free Rayleigh wave on the half space medium.

If  $a_1$  and  $\beta_1$  are not infinitely large,  $a_1/a_2\rightarrow\infty$  and  $\beta_1/\beta_2\rightarrow\infty$  are equivalent to  $a_2=\beta_2=0$  which will regard as to the condition of a "plate". As shown in Fig. 46, when the ratio  $\beta_1/\beta_2$  or  $a_1/a_2$  increases, the dispersion curve of the surface wave for the high velocity layer model approaches to that of  $M_{21}$  wave for a plate model. The abscissa and ordinate of this figure are normalized to  $\beta_1$  for showing this relation.

The other special high velocity layer models are shown in Fig. 47 and Table 9. In these models, compressional wave velocities in the surface layer are equal to those in the half space, but shear wave velocities in the surface layers are greater than those in the half spaces. As shown in Fig. 48, the surface waves for these models have the similar feature to that for H-125 etc. In this case,  $a_2/\beta_2\rightarrow\infty$  corresponds to a liquid half space. The problem of this type is sometimes called the "floating ice problem".

All surface waves discussed in this section are those corresponding to  $M_{21}$  wave (or an antisymmetric mode) for a "plate" model. Is there any surface wave corresponding to  $M_{11}$  wave (or a symmetric mode)? This problem will be discussed briefly in § 4.2.

#### 4.2. Model experiments of surface waves propagating on high velocity layer models.

Experimental surface waves propagating on the high velocity layer models are analyzed here. Similar experiments have been carried out by OLIVER, PRESS and EWING<sup>18)</sup>. However, they had no ideas about the leaking mode, and only experimental date were shown. Two dimensional models used in the present study are aluminum-Lamiverre and aluminum-plastics models.

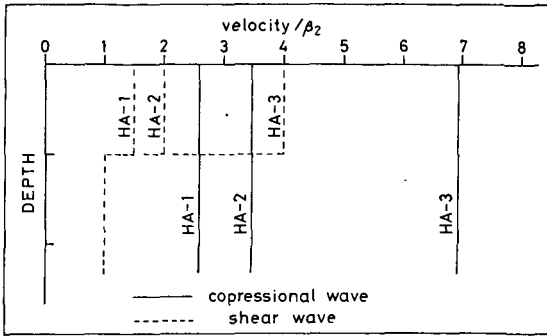


Fig. 47

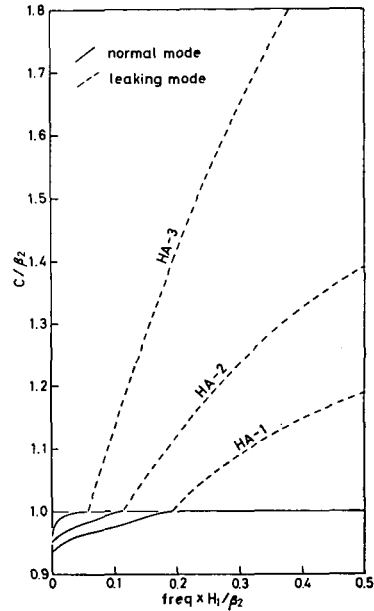


Fig. 48

Fig. 47. Compressional and shear wave velocity distributions of three high velocity layer models, HA-1, HA-2 and HA-3.

Fig. 48. Phase velocity curves for three high velocity layer models shown in Fig. 47.

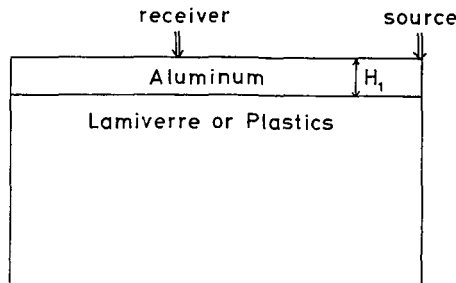


Fig. 49. Schematic diagram of the present model experiment. Both AL-LAM and AL-PL models were used.

These models are called simply AL-LAM and AL-PL models here. The elastic constants of the three plates, about 2 mm thick, have been tabulated in Table 1. The equipment used in the present model experiment is same as that used in § 3. The sound source is a pulse of 5–10 $\mu$ s width.

The schematic diagram of the experiment is illustrated in Fig. 49. A

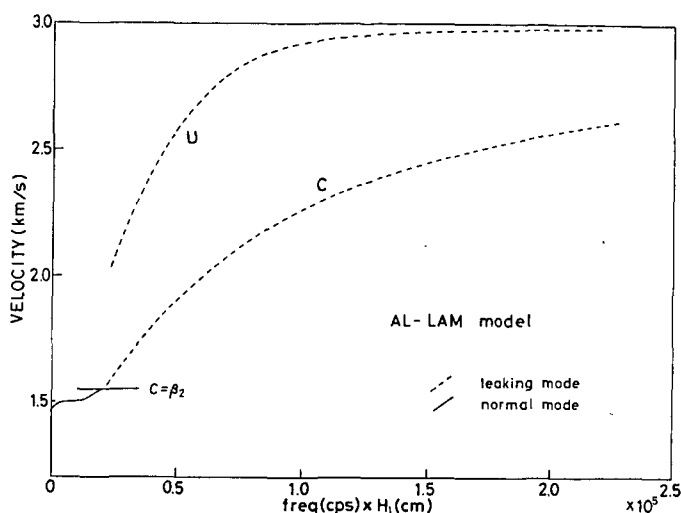


Fig. 50. Phase and group velocity curves of surface waves for AL-LAM model.

sound source was attached to a corner of the model in order to avoid the reflection signals which may become undesirable disturbances on the record, because the dimensions of these models are only  $85 \times 85 \text{ cm}^2$ . Though the corner of the model is a kind of the singular point, no effects of it could not be found on the record, *prima facie*.

Phase and group velocity curves for AL-LAM model are shown in Fig. 50. This group velocity curve was calculated by the usual way mentioned before. The group velocity is larger than the phase velocity because of "inverse dispersion" of the phase velocity. The group velocity curve of the normal mode is not given in Fig. 50. Since the gradient of the phase velocity curve suddenly changes at a transition point from the leaking mode to the normal mode, the group velocity may have a great gap at this point.

Figs. 51 (a), (b) and (c) are experimental records for AL-LAM model. The equipment used in the present experiment has not so broad frequency response that a single model cannot get the record whose frequency range is broad enough to cover the theoretical dispersion curve. Because of this reason, model experiments were carried out for three models whose layer thicknesses are 2 cm, 1 cm and 0.4 cm respectively. By using this way, the frequency range of the equipment can be relatively broadened.

Wave trains of inverse dispersion which have large amplitudes can be found in the records of Figs. 51 (a), (b) and (c). The short period portion of

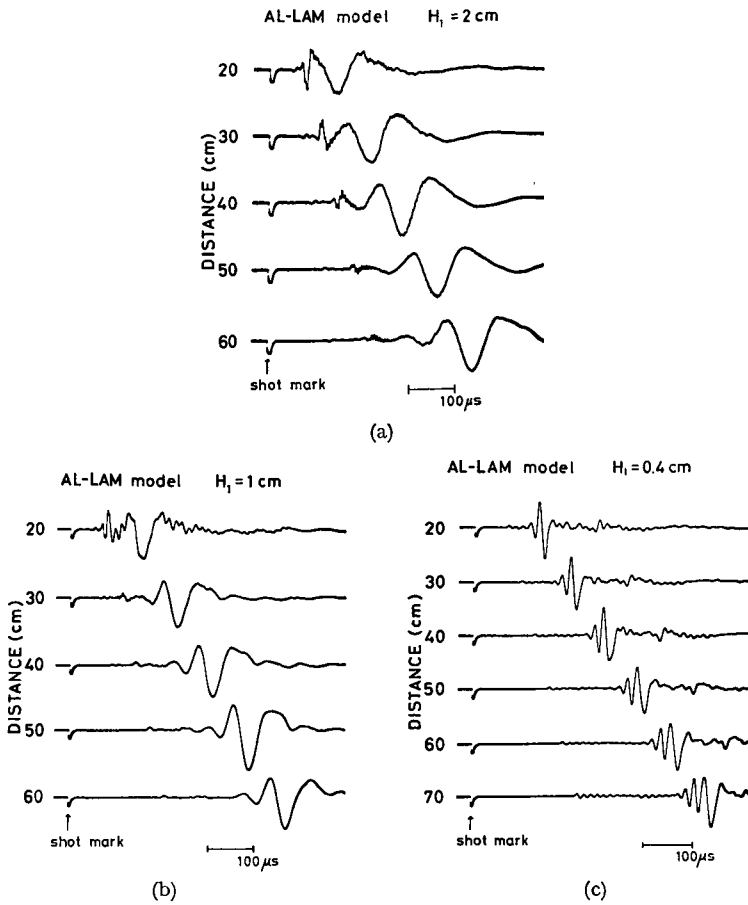


Fig. 51. Experimental records for AL-LAM model.  
 (a)  $H_1 = 2$  cm, (b)  $H_1 = 1$  cm, (c)  $H_1 = 0.4$  cm.

the wave train damps suddenly with increase of the epicentral distance. Probably, it is due to the leakage of wave energy from the superficial layer to the half space.

Observed phase and group velocities were calculated by NAFE and BRUNE'S<sup>30)</sup> and PEKERIS'S<sup>23)</sup> methods from the travel time chart of peaks and troughs of the wave train. Fig. 52 represents the comparison of the observed and the theoretical dispersion. The agreement may be satisfactory. In the case of a model which has a surface layer of 0.4 cm thick, the predominant wave train seems to be the normal mode because of large attenuation of the

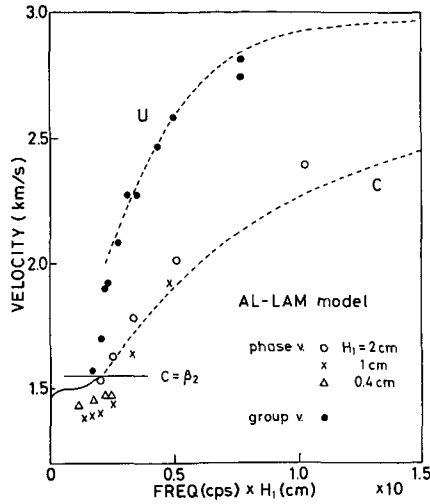


Fig. 52. Theoretical dispersion curves and observed data for AL-LAM model. Observed data were calculated from the travel time chart of peaks and troughs of were trains.

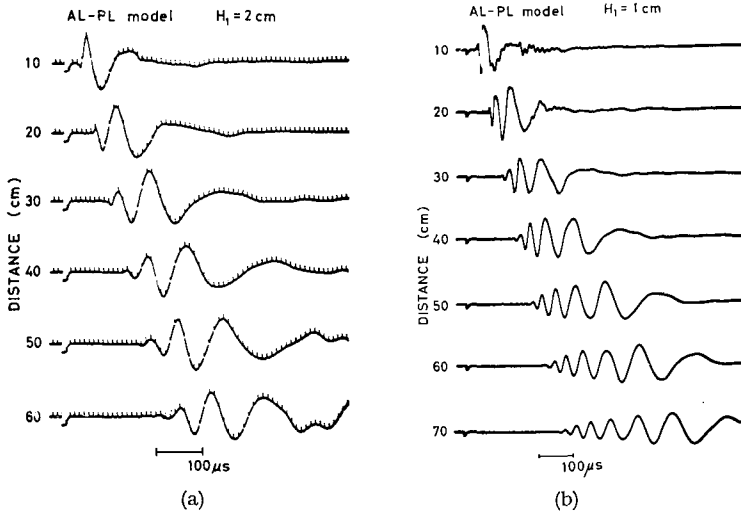


Fig. 53. Experimental records for AL-PL models. (a)  $H_1=2$  cm, (b)  $H_1=1$  cm.

leaking mode within the frequency range of the equipment. Small discrepancy between the observation and the theory in the normal mode region may be due to the measurement error in elastic constants of the Lamiverre plate. Since the Lamiverre plate has small unisotropy, this plate is not so

good as the constituent medium for the model experiment.

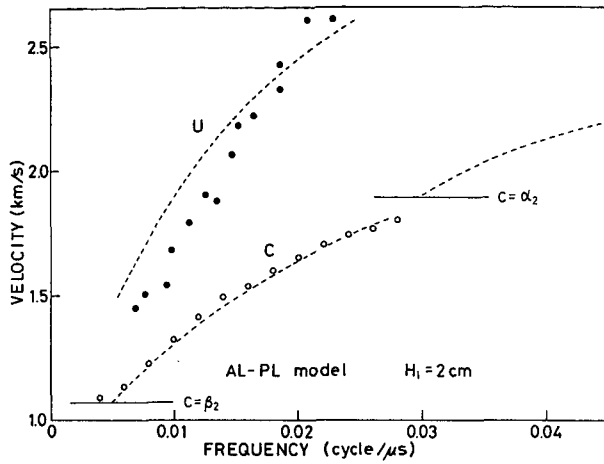
Figs. 53 (a) and (b) are records for AL-PL model. This model has larger velocity contrast than AL-LAM model, and thicknesses of surface layers are 2 cm and 1 cm. Very beautiful dispersed wave trains of inverse dispersion are found in the records.

The comparison between the observation and the theory of the surface wave is shown in Fig. 54. Again, theoretical dispersion curves of the leaking mode were calculated by OLIVER and MAJOR's and SU and DORMAN's methods. Observed phase velocities were obtained from the phase delay of the spectral analysis. Group velocities were obtained by the usual way. As illustrated in Fig. 54, the agreement between the observation and the theory is considered to be excellent. Small discrepancies of the observed and theoretical group velocities may be due to time delay of the equipment, because no group delay corrections have been done in the evaluation of observed group velocities. In the case of  $H_1=1$  cm, the short period of the wave train and the large epicentral distance relatively decrease this time delay in compared with the case of  $H_1=2$  cm, and the agreement is better than in the latter case. The discontinuity of the theoretical curve at  $c=a_2$  was already discussed in § 4.1. No predominant wave trains in the region of  $c>a_2$  were observed in the experimental records. This may be due to the large attenuation of this wave.

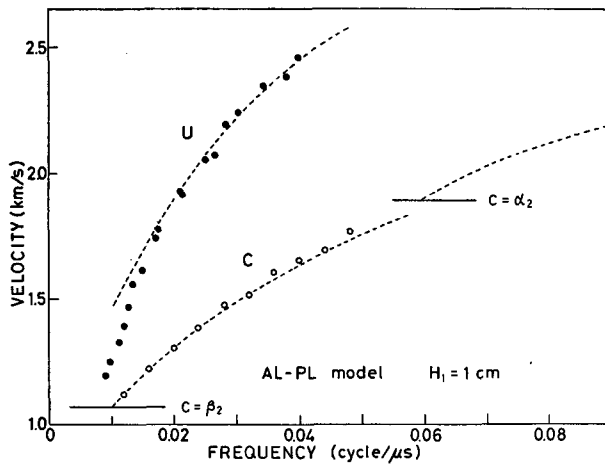
Next, we discuss the attenuation of the leaking mode. Since the most predominant surface wave on AL-PL model is the leaking mode, this model is suitable to examine the attenuation of the leaking mode.

One of the most interesting characteristics of the leaking mode is attenuation. In general, the phase velocity of the leaking mode is larger than the shear wave velocity in the half space, and a part of wave energy of the propagating wave leaks into the half space. This leakage causes the attenuation which is peculiar to leaking mode propagation.

Upper parts of Figs. 55 (a) and (b) are the amplitude spectra of the experimental records which were represented in Fig. 53. These spectra are normalized at a point which is very close to the boundary between the normal mode and the leaking mode, because the attenuation discussed here is expected to be zero in the normal mode region. Large attenuation of the leaking mode can be soon recognized from these figures. Attenuation coefficients obtained from these spectra are illustrated in the lower parts of Figs. 55 (a) and (b) by open circles.



(a)



(b)

Fig. 54. Theoretical curves and observed data for AL-PL model. Observed phase velocities were calculated from the spectral analysis of the records.

(a)  $H_1 = 2$  cm, (b)  $H_1 = 1$  cm.

Beside the attenuation due to "energy leak", there is another attenuation due to "absorption" in the propagation of the leaking mode. The surface wave absorption on the aluminum plate is very small and negligible, but that on the plastics plate is considerable, about  $Q=28^*$ . The absorption of the normal mode on the layered half space can be estimated by the

\* This  $Q$  was defined by  $Q = \pi f / ac$ , where  $a$  is the absorption coefficient,

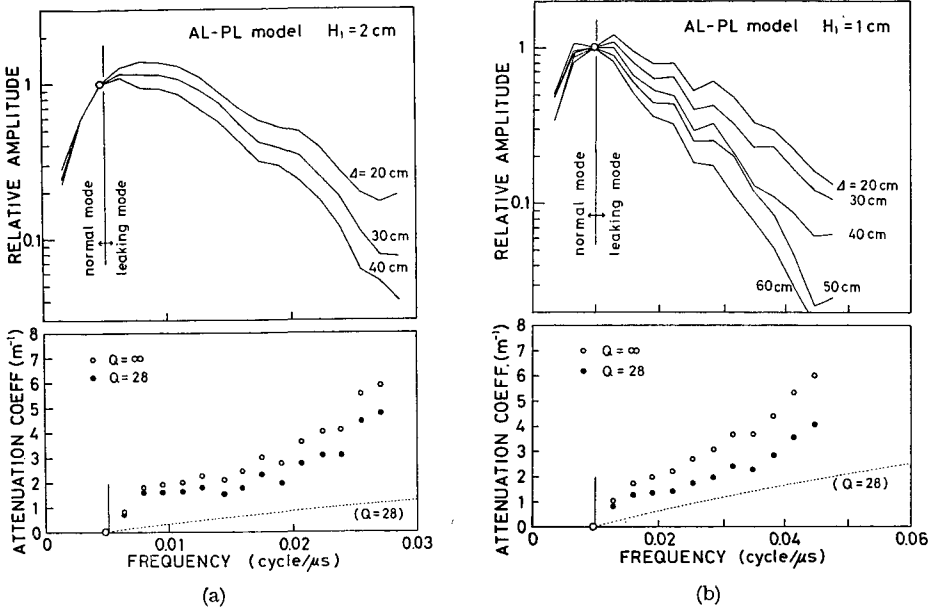


Fig. 55. Relative amplitude spectra and attenuation coefficients of the surface wave for AL-PL model. (a)  $H_1=2$  cm, (b)  $H_1=1$  cm.

energy integral<sup>40</sup>) but that of the leaking mode cannot be calculated here, because the definition of the amplitude distribution with depth of the leaking mode is vague. However, it is clear that  $Q=28$  indicates the maximum absorption of the leaking mode discussed here. Dotted lines in the lower parts of Figs. 55 (a) and (b) represent this absorption coefficients for  $Q=28$ . Closed circles in these figures are evaluated by subtracting the values on dotted lines from those of open circles. The attenuation coefficients of the leaking mode which are purely due to the energy leak must be situated between these open and closed circles.

When we restrict our attention to the dispersion of the leaking mode, two approximate methods have been very useful as mentioned before. But it is necessary for the analysis of the attenuation to find complex roots of the period equation, because the imaginary part of the complex root has a close relation to the attenuation of the leaking mode.

In Fig. 56, the complex root for AL-PL model is shown by dashed lines. This complex root is “ $k$ -real,  $f$ -complex” type and is similar to that by GILBERT<sup>13</sup>). Since imaginary part  $\tilde{f}$  is much smaller than real part  $\tilde{f}$ , the

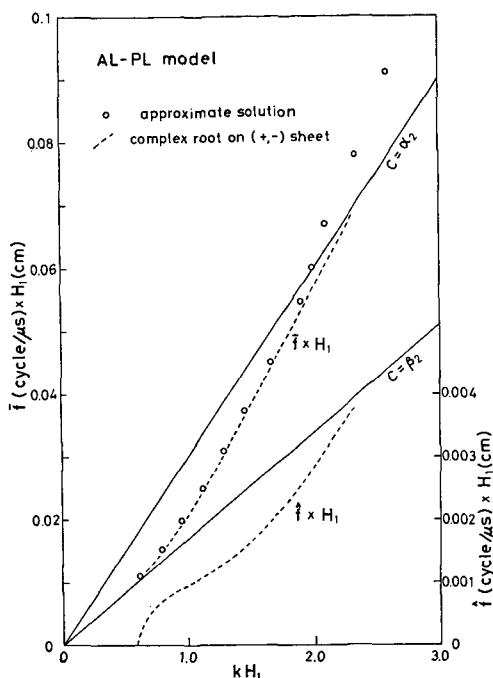


Fig. 56. Complex roots on (+, -) Riemann sheet for AL-PL model. Open circles are approximate solutions of leaking modes by two approximate methods.

scale of the ordinate for  $\hat{f}$  is largely exaggerated. Approximate solutions are also illustrated by small open circles. In the region of  $\beta_2 < c < a_2$ , the real part of the complex root fits well to these approximate solutions. The complex root shown in this figure is on the (+, -) sheet which is one of four Riemann sheets labeled by GILBERT<sup>13)</sup>. The approximate solutions in  $c > a_2$  may correspond to the complex root on the (-, -) sheet (See §7).

The expression of the surface wave contains a factor  $\exp(i\omega t)$  which means stationary vibrations. If frequency is assumed to be complex, namely  $f = \bar{f} + i\hat{f}$ , then  $\exp(i\omega t) = \exp(2\pi i \bar{f} t) = \exp(2\pi i \bar{f} t) \cdot \exp(-2\pi \hat{f} t)$ . The last exponential factor corresponds to attenuation with time. Now,  $t = x/U$  and  $\exp(-2\pi \hat{f} t) = \exp(-2\pi \hat{f} x/U)$ , where  $x$  and  $U$  mean the distance and the group velocity, respectively. Then, the attenuation coefficient  $a$  obtained from the spectral analysis can be related to the complex root by the following relation,

$$a = 2\pi \hat{f} / U \quad \text{or} \quad \hat{f} = aU / 2\pi. \quad (7)$$

Observed and theoretical attenuations are compared in Fig. 57. It is obvious

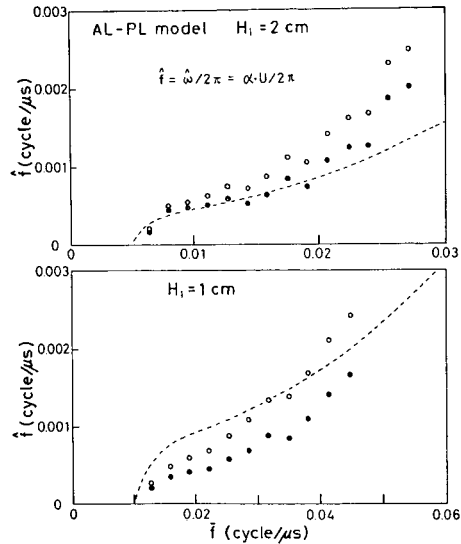


Fig. 57. Comparison of observed and theoretical attenuations for AL-PL model. Dashed lines are loci of the imaginary part of the complex root.

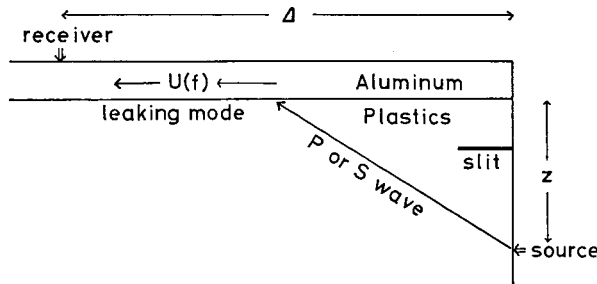


Fig. 58. Schematic diagram of the model experiment on coupling of the body wave and the leaking mode.

that the observed attenuation coefficient can be explained by the imaginary part of the complex root. This is one of the most important results in the present study.

Fig. 58 is the schematic diagram of the model experiment on the coupling of the body wave and the leaking mode. This type of coupling was first discussed by OLIVER<sup>24</sup>), and he suggested a hypothesis. According to him, this coupling occurs when the apparent velocity of the body wave, which comes up from the half space to the wave guide, is equal to the phase

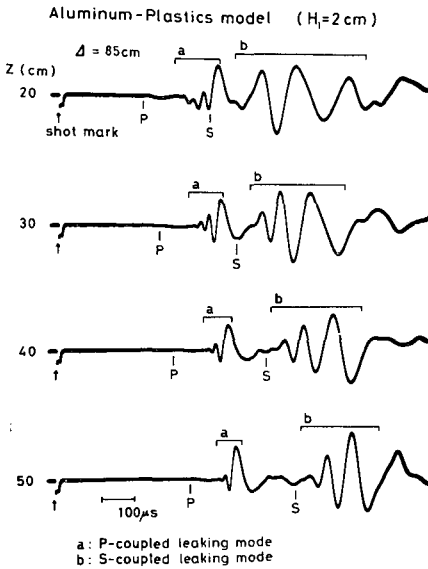


Fig. 59

Fig. 59. Observed records. Brackets **a** and **b** indicate P-coupled and S-coupled leaking modes respectively.

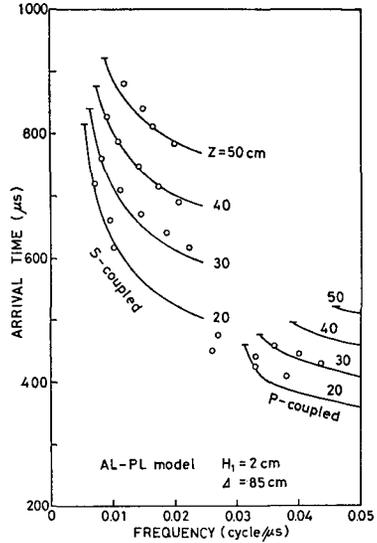


Fig. 60

Fig. 60. Observed and theoretical arrival times of P-coupled and S-coupled leaking modes. Theoretical curves were calculated by Eq. (8).

velocity of the leaking mode. OLIVER<sup>24</sup>), SU and DORMAN<sup>11</sup>) and CHANDER et al.<sup>26</sup>) investigated the long period vibrations near S arrivals using OLIVER's hypothesis. Since the leaking mode is a predominant surface wave on AL-PL model, it seems to be very easy to examine the coupling by using this model. A slit on the side of the model, as shown in Fig. 58, was set to avoid any surface wave which travels around the corner.

In the present experiment, the epicentral distance  $\Delta$  was fixed in 85 cm taking account of the size of the model. The "source depth"  $z$  was changed from 20 to 50 cm.

From OLIVER's hypothesis, the arrival time  $t(f)$  of the wave train can be explained by a following simple equation,

$$t(f) = \frac{c(f) \cdot z}{V \cdot (c(f)^2 - V^2)^{1/2}} + \frac{\Delta - z / (c(f)^2 - V^2)^{1/2}}{U(f)} \quad (8)$$

where  $V$  is the shear or the compressional wave velocity in the half space. This equation can be easily evaluated from dispersion curves of the leaking mode.

Actual records obtained are shown in Fig. 59, and observed arrival times

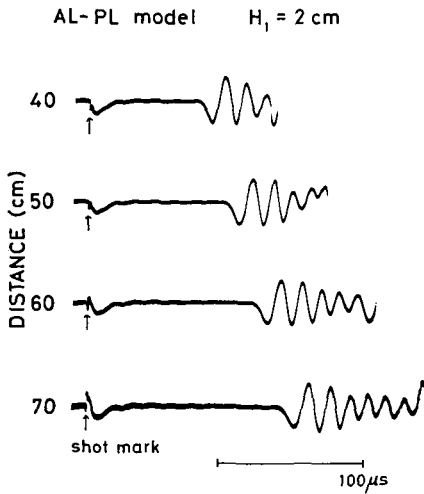


Fig. 61

Fig. 61. Observed records of the wave train on AL-PL model corresponding to  $M_{11}$  wave on the "plate" model.

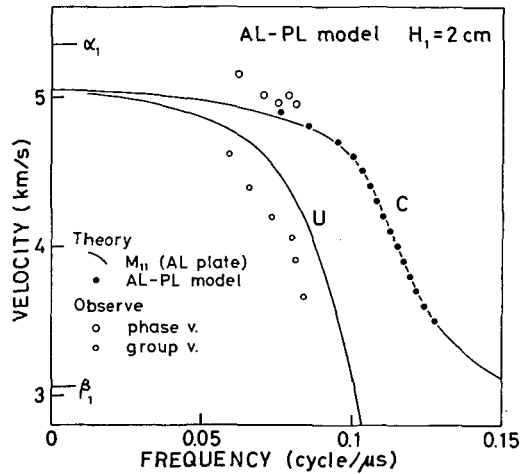


Fig. 62

Fig. 62. Observed and theoretical dispersions of the wave train corresponding to  $M_{11}$  wave.

are compared with theoretical curves in Fig. 60. In Fig. 59, brackets **a** and **b** indicate regions of P-coupled and S-coupled leaking modes respectively. The agreement between observed and theoretical arrival times is very good. Thus, OLIVER's hypothesis of the coupling of the body wave and the leaking mode could be confirmed by the present model experiment. It must be noticed in this model experiment that the leaking mode in the region of  $c > a_2$  had very large amplitudes, though no reasons can be given now.

At the end of this section, surface waves which exist on the high velocity layer model and correspond to  $M_{11}$  waves on the "plate" model will be discussed. Very high gain records for AL-PL model are represented in Fig. 61. The gain of these records is so high that traces of later phases which were found in Fig. 53 (a) are all off scale. The layer thickness of the model is 2 cm.

Solid lines in Fig. 62 are the dispersion curves of  $M_{11}$  wave for an aluminium plate, and solid circles represent the approximate solutions of the leaking mode for AL-PL model. The agreement is very good. Open circles are observed dispersion data from the records in Fig. 61. It is soon recognized from these figures that the existence of the leaking mode corresponding to

$M_{11}$  wave is sure. The amplitude of this wave train is not so large, probably due to small excitation and large attenuation.

### 5. Wave group II observed on the record of small explosion seismology.

On the records of small explosion seismology, we often find several predominant wave groups. These wave groups have been called (usually in Japan) wave groups I, II, III and IV<sup>41)</sup>. Wave group I is the first arrival and is the refracted P wave. Wave groups III and IV have characteristics of surface waves and they have been recognized as higher and fundamental modes of Rayleigh type surface waves. Wave group II appears just after wave group I, and it has large amplitude especially in the experiment on the "wet" or "muddy" field.

Many arguments about wave group II have been reported but no definite conclusions have been given as far as the present author knows. There are two stand points in the discussion on wave group II, namely, whether this wave group is the surface wave or the body wave. In early studies of small explosion seismology, this wave was recognized as a normal higher mode of the Rayleigh type<sup>42)</sup>. However, the above recognition has such a difficulty that the phase velocity of this wave train is much larger than any shear wave velocity in the structure under consideration. OKADA<sup>43)</sup> explained that this wave group was constructed by the superposition of many body waves. KUBOTERA and OHTA<sup>44)</sup> took this wave group as surface waves on a liquid layer over a liquid half space, though the media of the actual field were not liquid but "wet" solid.

It is the author's opinion that wave group II must be discussed in the light of the leaking mode because of its larger phase velocity and of the feature of its dispersion. In §5.1, the dispersion curves of the leaking mode for single layer models which have various velocity contrasts and various Poisson's ratios will be calculated. This calculation will show the transition from the surface wave on the solid-solid model to that on the liquid-liquid model. In §5.2, some actual records of wave group II will be analyzed.

#### 5.1. Theoretical dispersion curves.

Elastic constants of the models analyzed in this section are tabulated in Table 10. These single layered models are divided into three groups according to the velocity contrast between the surface layer and the half space. The

Table 10. Elastic constants of models.

1) velocity contrast: 2.0

| Model | $a_2/a_1$ | $\beta_1/a_1$ | $\beta_2/a_1$ | $\rho_2/\rho_1$ | $\sigma$ |
|-------|-----------|---------------|---------------|-----------------|----------|
| A-1   | 2.0       | 0.577         | 1.155         | 1.0             | 0.250    |
| A-2   | 2.0       | 0.500         | 1.000         | 1.0             | 0.333    |
| A-3   | 2.0       | 0.250         | 0.500         | 1.0             | 0.467    |
| A-L   | 2.0       | —             | —             | 1.0             | (0.5)    |

2) velocity contrast; 1.5

| Model | $a_2/a_1$ | $\beta_1/a_1$ | $\beta_2/a_1$ | $\rho_2/\rho_1$ | $\sigma$ |
|-------|-----------|---------------|---------------|-----------------|----------|
| A-11  | 1.5       | 0.577         | 0.866         | 1.0             | 0.250    |
| A-12  | 1.5       | 0.500         | 0.750         | 1.0             | 0.333    |
| A-12A | 1.5       | 0.400         | 0.600         | 1.0             | 0.405    |
| A-12B | 1.5       | 0.333         | 0.500         | 1.0             | 0.438    |
| A-13  | 1.5       | 0.250         | 0.375         | 1.0             | 0.467    |
| A-1L  | 1.5       | —             | —             | 1.0             | (0.5)    |

3) velocity contrast: 3.0

| Model | $a_2/a_1$ | $\beta_1/a_1$ | $\beta_2/a_1$ | $\rho_2/\rho_1$ | $\sigma$ |
|-------|-----------|---------------|---------------|-----------------|----------|
| A-21  | 3.0       | 0.577         | 1.732         | 1.0             | 0.250    |
| A-22  | 3.0       | 0.500         | 1.500         | 1.0             | 0.333    |
| A-22A | 3.0       | 0.400         | 1.200         | 1.0             | 0.405    |
| A-23  | 3.0       | 0.250         | 0.750         | 1.0             | 0.467    |
| A-24  | 3.0       | 0.167         | 0.500         | 1.0             | 0.486    |
| A-2L  | 3.0       | —             | —             | 1.0             | (0.5)    |

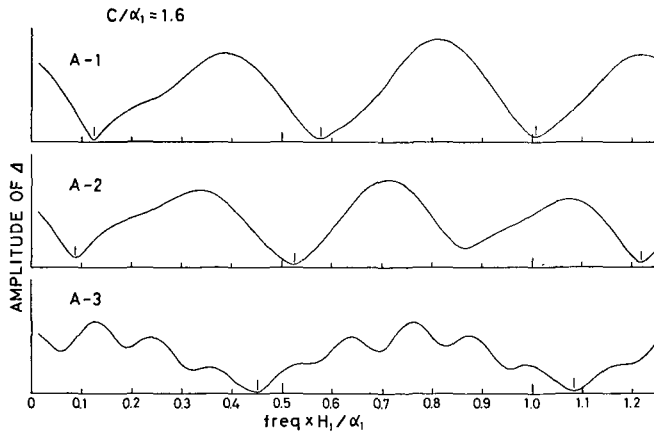


Fig. 63. Calculated examples of the period functions for models A-1, A-2 and A-3. Ordinate is arbitrary linear scale.

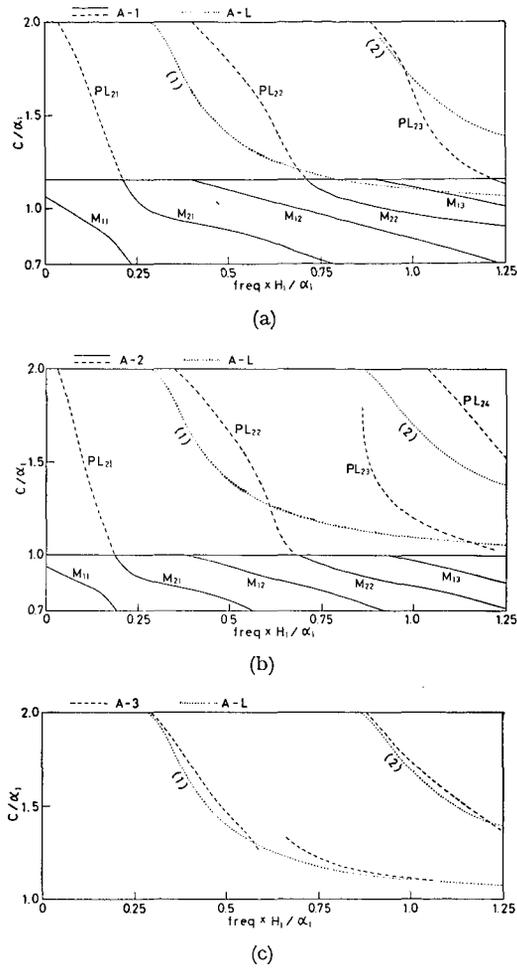


Fig. 64. Theoretical phase velocity curves of the normal and leaking modes for the models whose velocity contrasts are 2.0. (a) Model A-1, (b) Model A-2 and (c) Model A-3. Dotted lines represent the dispersion curves of the pressure wave for Model A-L.

velocity contrasts discussed here are 1) 2.0, 2) 1.5 and 3) 3.0, and Poisson's ratios are changed from 0.25 to 0.5 in each group. Dispersion curves of leaking modes were calculated by OLIVER and MAJOR's and SU and DORMAN's methods.

In Fig. 63, some calculated examples of the period functions for Models A-1, A-2 and A-3 are shown where the phase velocity is  $1.6 \times \alpha_1$ . Sharp

minima indicated with small dashes can be found. The pattern of the period function for A-3 is characterized by the superposition of two different vibrations. These longer and shorter period vibrations may be correlated with the compressional and shear waves in the surface layer.

Phase velocity curves of the normal and leaking modes are shown in Figs. 64 (a), (b) and (c). In these figures, the dispersion curves for Model A-L which is a single layered liquid model are also represented by dotted lines for comparison. Notations (1) and (2) in the figures mean the order number of the pressure wave.

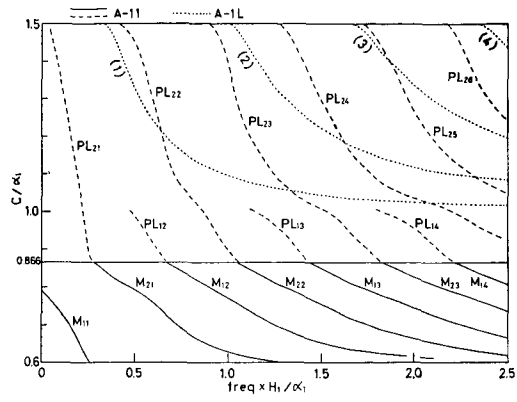
In Fig. 64(a), dispersion curves of the normal and leaking modes for A-1 are illustrated by solid and dashed lines respectively. As in § 3, the leaking modes were labeled according to the connections to M waves. Poisson's ratio of this model is 0.25, and therefore, this figure is very similar to Fig. 5 for PL-AL model. No remarkable correlations between A-1 and A-L can be found. In this case, the series of  $PL_{1n}$  is not so clear as in the case of PL-AL model.

Fig. 64 (b) is the case of Model A-2. Dispersion curves become closer to each other because of the smaller shear wave velocity, but this figure is essentially similar to Fig. 64 (a).

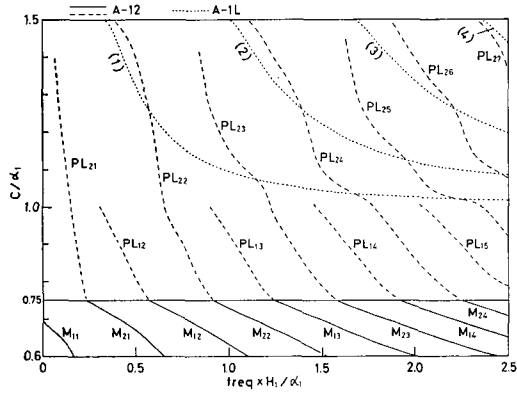
The dispersion curves for Model A-3 are shown in Fig. 64 (c). Only sharp minima were picked up to determine these dispersion curves (See Fig. 63). The phase velocity curve for A-3 is very close to that for A-L, and it is easily understood that the phase velocity of the leaking mode may be close to that of the pressure wave for the large Poisson's ratio model. In Fig. 64(c), the dispersion curve of the leaking mode has a gap at about  $c/\alpha_1=1.3$ . This character will be discussed later in more detail.

In Figs. 65 (a), (b), (c), (d) and (e), the dispersion curves for Models A-11, A-12, A-12A, A-12B and A-13 are illustrated. Again, the dispersion curves of the pressure waves for Model A-1L are drawn by dotted lines in each figure. Dispersion curves of the phase velocity less than  $0.6 \times \alpha_1$  were neglected.

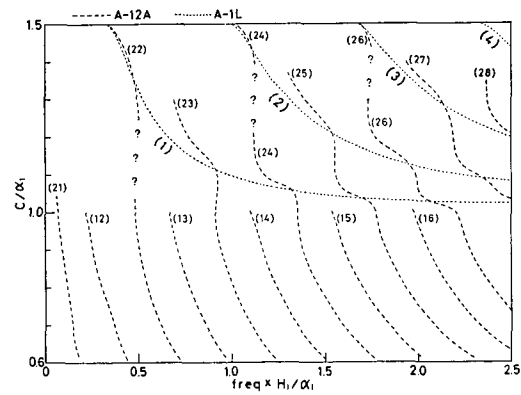
Poisson's ratio of Model A-11 is 0.25 and the phase velocity curves for this model are shown in Fig. 65(a). Notations of (1),  $PL_{21}$ ,  $M_{11}$  etc. are same to those in the previous case. No remarkable correlations between dispersion curves of the leaking mode and the pressure wave can be found. Dispersion curves of  $PL_{1n}$  waves seem to begin from the points where  $c \approx \alpha_1$ , and this velocity has been called the "quasi-cutoff" velocity by GILBERT



(a)



(b)



(c)

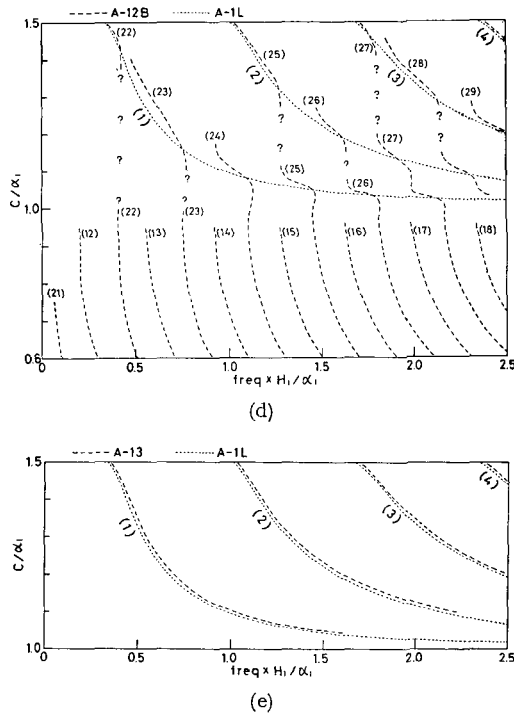


Fig. 65. Theoretical phase velocity curves of the normal and leaking modes for the models whose velocity contrasts are 1.5. (a) Model A-11, (b) Model A-12, (c) Model A-12A, (d) Model A-12B, (e) Model A-13. Dotted lines represent the dispersion curves of the pressure wave for Model A-1L.

and LASTER<sup>19</sup>).

The dispersion curves for Model A-12 whose Poisson's ratio is 0.333 are shown in Fig. 65 (b). The quasi-cutoff velocity is also exist. Slight correlation between the leaking mode and the pressure waves is recognized.

The dispersion curves for Model A-12A whose Poisson's ratio is 0.405 are shown in Fig. 65(c). Specific intervals of phase velocity curves become smaller due to larger Poisson's ratio. Since Poisson's ratio of this model is larger than that of usual elastic media, it may be questionable to call the leaking mode on this model as "PL wave". In this paper, the leaking modes like this are indicated simply by notations (21), (12), (22) etc. according to the connections to the M waves.

The dispersion curves for Model A-12B whose Poisson's ratio is 0.438 are shown in Fig. 65(d), and the correlation between the leaking mode and

the pressure wave is now very clear. From the examples of A-12A and A-12B, the transition from the leaking mode to the pressure wave can be easily understood. In the computation of OLIVER and MAJOR's method, minima of the period function are very sharp near the dispersion curve of the pressure wave where excitation of the leaking mode may be expected to be large. The transition from the solid-liquid model to the liquid-liquid model has a similar nature to the present problem<sup>45)</sup>.

Fig. 65 (e) is the case of Model A-13 whose Poisson's ratio is 0.467. Obtained dispersion curves of the leaking mode are very close to those of the pressure wave except for slight shifts to high frequency. Actually, dispersion curves for Model A-13 may be composed of many dispersion curves closely spaced, as in the case of A-12B etc. The "resolution power" of the approximate methods may be not enough to separate these curves, and only sharp minima near the pressure wave were picked up as the dispersion curve of the leaking mode. In Fig. 65 (d), there are some parts on dispersion curves where  $dc/df > 0$ , resulting in the negative group velocity. The concept of the negative group velocity has not been clear.

Figs. 66 (a), (b), (c), (d) and (e) are the dispersion curves for Models A-21, A-22, A-22A, A-23 and A-24 whose velocity contrasts are all 3.0. Dotted lines in each figure are dispersion curves of the pressure wave for Model A-2L. Elastic constants of these models have been tabulated in Table 10.

The dispersion curves for Model A-21 whose Poisson's ratio is 0.25 are shown in Fig. 66(a). Dispersion curves of  $PL_{13}$  modes are not so clear for this model, probably because "quasi-cutoff" velocity  $a_1$  is smaller than  $\beta_2$ . In general, the dispersion curve of the normal mode for a model whose velocity contrast is pretty large has the very complicated feature. For example, the set of dispersion curves of M waves has many "kinks" at  $c/a_1 \approx 1$ . Also in the leaking mode region, we must take attention to a fact that the dispersion curves of  $PL_{13}$  and  $PL_{22}$  waves seem to be connected "at a glance" with those of  $M_{22}$  and  $M_{13}$  waves respectively.

Fig. 66(b) is the case of Model A-22 whose Poisson's ratio is 0.333. Obtained phase velocity curves of the normal and leaking modes are essentially similar to the case of A-21 but these curves become closer to each other. We can find a remarkable "kink" at a point where  $c = \beta_2$  and  $f \times H_1/a_1 = 0.6$ . Dispersion curves of  $PL_{13}$  and  $PL_{22}$  waves seem as if they are continuations of  $M_{22}$  and  $M_{13}$ , but actually they are connected with those of  $M_{13}$  and  $M_{22}$  respectively. No remarkable approach of the dispersion curves of the leaking

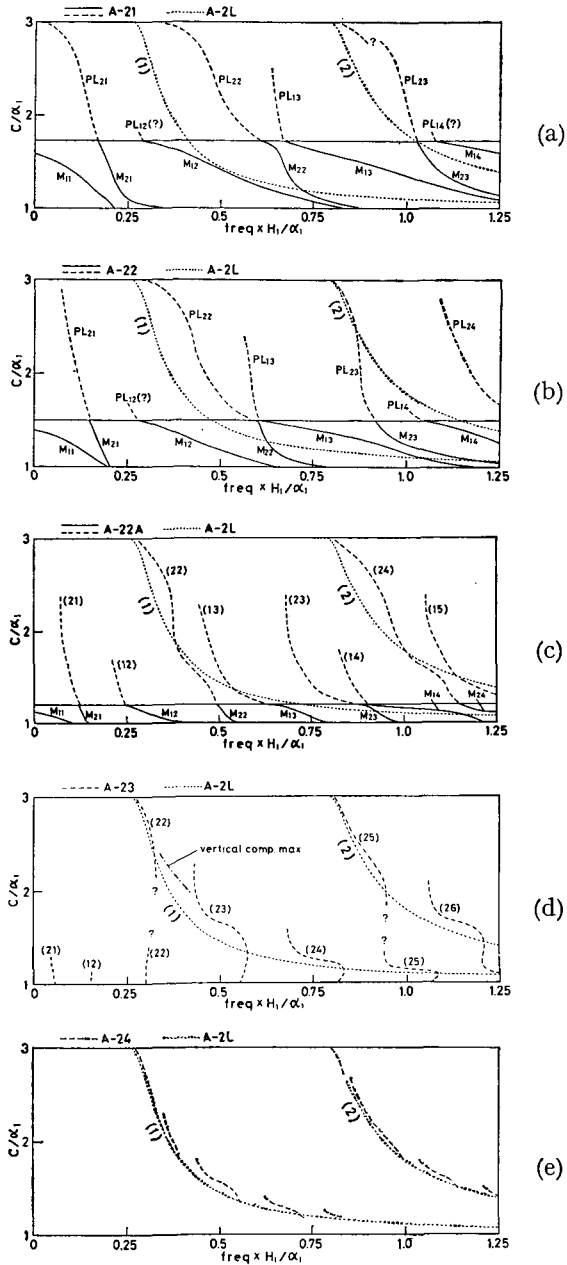


Fig. 66. Theoretical phase velocity curves of the normal and leaking modes for the models whose velocity contrasts are 3.0. (a) Model A-21, (b) Model A-22, (c) Model A-22A, (d) Model A-23 and (e) Model A-24. Dotted lines represent the dispersion curves of the pressure wave for Model A-2L.

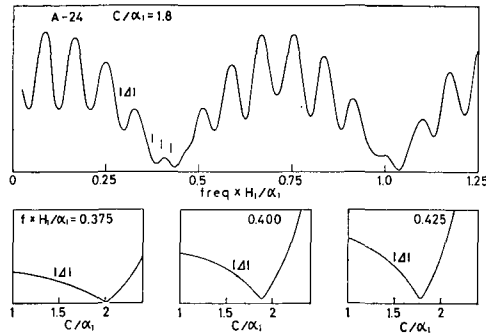


Fig. 67. Calculated examples of the period function for Model A-24 under two different conditions. Upper;  $c = \text{const.}$  Lower;  $f = \text{const.}$

mode to those of the pressure wave can be found.

The dispersion curves for Model A-22A whose Poisson's ratio is 0.405 are shown in Fig. 66 (c), and some parts of the leaking mode have approached to the pressure wave. It must be remarked that (22), (13),  $M_{23}$ ,  $M_{14}$  and  $M_{24}$  waves are suggested to have the close relation with the pressure wave. It may be expected that the "excitation function" of these waves<sup>46)</sup> has large values near the dispersion curve of the pressure wave.

Fig. 66 (d) is the case of Model A-23 whose Poisson's ratio is 0.467 and is larger than the previous values. But dispersion curves of the leaking mode do not come so close to the pressure wave as in the case of Models A-13 or A-3. This may be due to the larger velocity contrast. By tracing the maxima of the spectrum of the vertical component, dispersion curves of (22) and (23) were connected to each other as indicated by a chain line.

Fig. 66(e) is the case of Model A-24 whose Poisson's ratio is 0.486. These curves are very close to the pressure wave for Model A-2L, but they are divided into small pieces. These curves were obtained by tracing only the sharp minima of the period function. The wave train with large amplitudes cannot be expected in the region of "dull" minima.

In Fig. 67, some calculated examples of the period function for Model A-24 are shown. The upper figure is drawn under the condition of " $c = \text{const.}$ " As mentioned before, this curve is composed of two vibrations with different wave lengths, and the "dividing" of the dispersion curves, as in Fig. 66 (e) is due to this short period vibration of the period function. On the other hand, if the period function is drawn under the condition of " $f = \text{const.}$ ", no short period vibrations appear as shown in the lower figure of Fig. 67. The

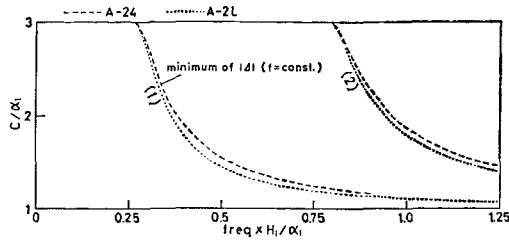


Fig. 68. Approximate dispersion curves of the leaking mode for Model A-24 obtained under the condition of “ $f=\text{const.}$ ”

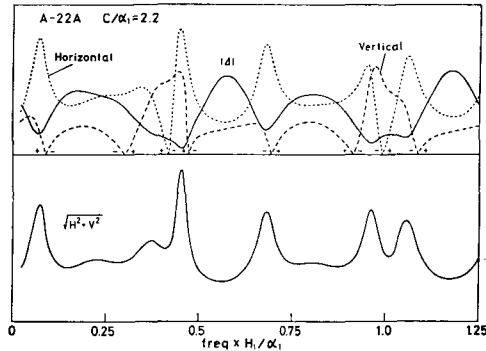


Fig. 69. Upper; Example the calculation by two approximate methods for Model A-22A.  
Lower; Spectrum of synthesized amplitude.

former condition makes many “gaps” on the dispersion curve of the leaking mode. But the period function which is drawn under the latter condition is not disturbed by the short period vibration as in the lower figure of Fig. 67. Fig. 68 represents the dispersion curves of the leaking mode which were obtained by tracing the minima of the period function under a new condition “ $f=\text{const.}$ ” mentioned above. New curves are not broken and very close to those of the pressure wave as in the case of Models A-3 or A-13. It is clear from Fig. 66 (e) and Fig. 68 that the dispersion curve for Model A-24 is practically equivalent to that for Model A-2L.

In all models with large Poisson’s ratio, namely A-3, A-13 and A-24, dispersion curves of the leaking mode are similar to those of the pressure wave. As mentioned before, wave group II is especially remarkable on the “soft ground” where Poisson’s ratio is nearly 0.5. Consequently, it was been confirmed that wave group II may be taken approximately as the pressure wave

in the field like this.

Next, some additional discussions about the approximate method will be given. As represented in the previous part of this paper, the approximate methods for the leaking mode are disturbed by two kinds of "anti-symmetries", namely the sudden sign change of the spectrum and steep exponential increase of the period function. The upper figure of Fig. 69 is an example of the calculation by two approximate methods. It is obvious that the positions of maxima of the spectra are disturbed by sudden changes of their sign. The lower figure illustrates the spectrum of synthesized amplitude  $(H^2 + V^2)^{1/2}$ , where  $H$  and  $V$  mean the two components of the spectrum. All the maxima of this new spectrum seem to be "symmetrical" and close spaced maxima does not disturb each other, namely the spectrum has distinct peaks. This synthesized amplitude may have "physically" more explicit meaning than each spectral component. This method was especially useful when Poisson's ratio was between 0.3 and 0.4.

### 5.2. Analyses of experimental records of wave group II.

In this section, actual records of wave group II will be analyzed. Fig. 70 is the example of wave group II which were observed in the experiment of small explosion seismology at Shirone, Niigata Prefecture<sup>44</sup>). Epicentral distances are from 101 to 122 m, and records of other epicentral distances are not shown here. Shot depths are 2 m (upper figure) and 20 m

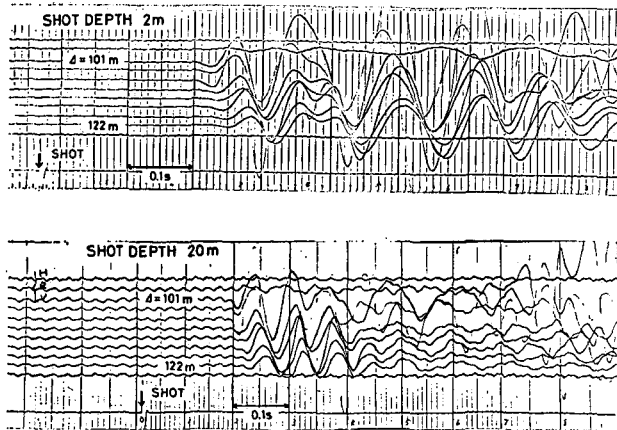


Fig. 70. Actual records of wave group II observed at Shirone, Niigata Prefecture. Upper; shot depth 2 m, Lower: shot depth 20 m.

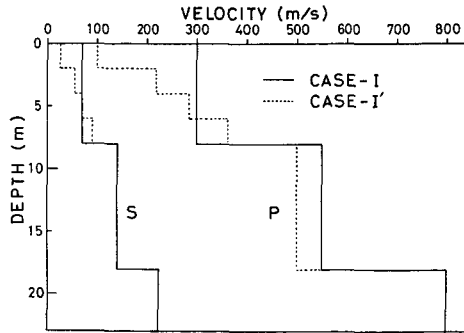


Fig. 71. Compressional and shear wave velocity distributions of CASE-I and CASE-I'.

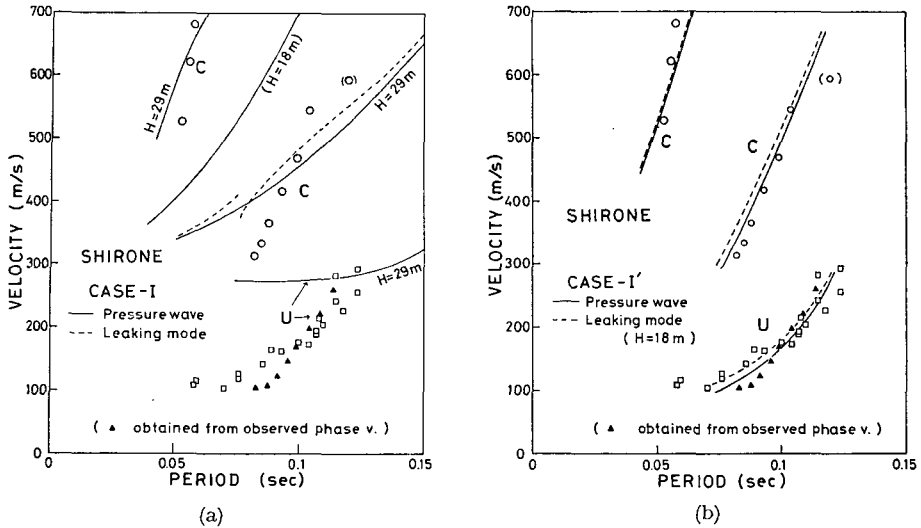


Fig. 72. Phase and group velocities of wave group II and theoretical dispersion curves.

(a) CASE-I, (b) CASE-I'.

Solid and dashed lines represent the dispersion curves of the pressure wave and the leaking mode respectively.

(lower figure) respectively. Predominant wave trains have periods of about 0.1 seconds in upper records and of 0.06 seconds in lower records. The latter one may be a higher mode.

Phase and group velocities of wave group II were obtained by using the records of the epicentral distance from 30 to 122 m. Usual peak and trough methods were carried out. Phase and group velocities observed are illustrated

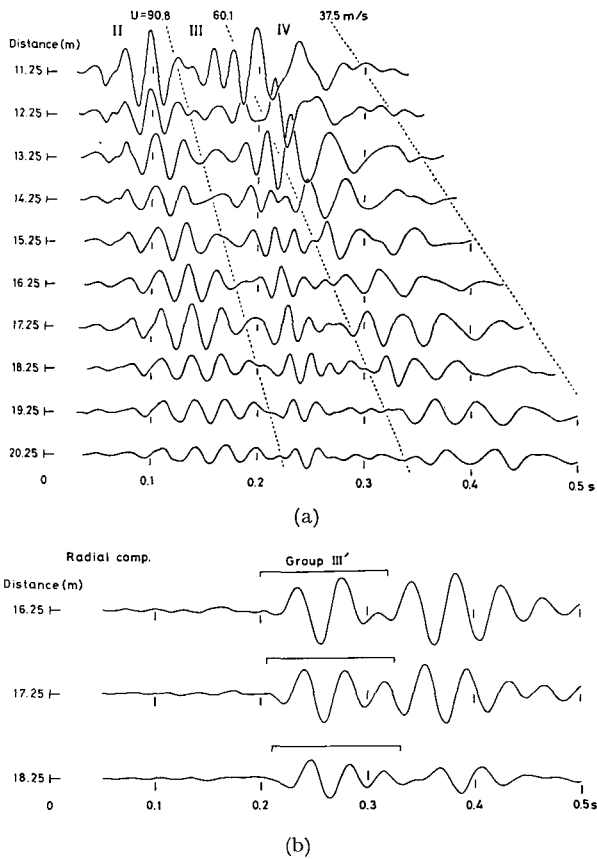


Fig. 73. Observed records obtained by small explosions in the ground of Geological Survey of Japan.  
 (a) vertical component, (b) radial component.

in Figs. 72 (a) and (b) together with theoretical dispersion curves for the models which are shown in Fig. 71.

The observed dispersion data and theoretical curves for CASE-I are shown in Fig. 72 (a). The calculated group velocity from the graphic differentiation of the observed phase velocity  $\circ$  is also represented with  $\blacktriangle$  which agrees very well with the directly observed group velocity. This result should suggest high reliability of both observed phase and group velocity data.

For the higher mode, only phase velocity data are shown for simplicity. CASE-I was determined from the result of the refraction analyses in the same field. Solid lines in Fig. 72(a) represent the dispersion curves of the

pressure wave for CASE-I. When the total thickness of two surface layers is assumed to be 18 m which was determined from the refraction analyses, the period of the theoretical curve is, on the whole, smaller than that of observed data. If more thicker surface layers are assumed, namely about 29 m in total, the better agreement is obtained but it is not enough particularly for the group velocity. In Fig. 72 (a), the approximate dispersion curve of the leaking mode for CASE-I is also illustrated by dashed lines which has similar features to those mentioned in § 5.1.

In Fig. 72(b), theoretical dispersion curves for CASE-I' are shown. The surface layer of this model has velocity gradient in total, being composed of four thin layers as illustrated in Fig. 71. This special structure is proposed by the tendency of observed group velocities. As shown in Fig. 72 (b), the agreement between theoretical curves for CASE-I' and observed data becomes excellent for both phase and group velocities. Total thickness of the layers above the half space of CASE-I' is taken as 18 m and agrees with the result from the refraction analyses. The average velocity in the surface layers in CASE-I might be overestimated by the refraction analysis. Solid and dashed lines represent the dispersion curves of the pressure wave and the leaking mode respectively. They are very close to each other.

This wave group II may be not sensitive to the structure of the shear wave<sup>2)</sup>. The shear wave structure must be deduced from analyses of the normal mode, such as Rayleigh wave. However, such analyses are not given here because the improved velocity structure of the shear wave will cause little change of the dispersion curve of the leaking mode.

Another example is the experiment by small explosions which was carried out in the ground of Geological Survey of Japan, Kawasaki, in 1953. This was one of the earliest field experiments by *Seismic Exploration Group of Japan*. Figs. 73 (a) and (b) represent some observed records of vertical and radial components respectively. These records are obtained mainly for the purpose of the analyses of the surface waves, and they are very beautiful because of suitable gain arrangement. TAZIME<sup>41)</sup> analyzed these records and proposed the "quarter wave-length low".

Observed wave trains are clearly divided into three groups, namely wave groups II, III and IV, by two lines of the constant group velocity as shown in Fig. 73 (a). An additional line,  $U=37.5$  m/s indicates the end of wave group IV. In the record of the radial component (Fig. 73 (b)), wave group II is very small but wave group III' has large amplitude and long

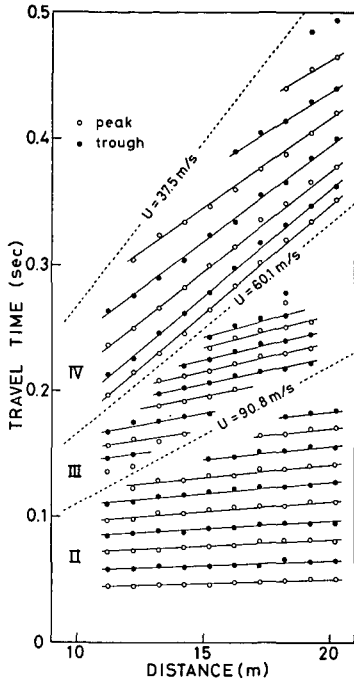


Fig. 74

Fig. 74. Travel time diagram of peaks and troughs obtained from the records in Fig. 73 (a).

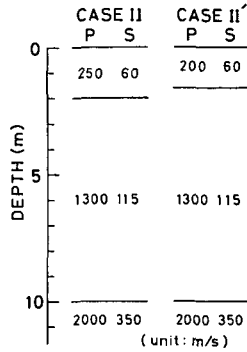


Fig. 75

Fig. 75. Proposed velocity distributions of CASE-II and CASE-II'.

periods.

Fig. 74 is the travel time diagram of peaks and troughs in the records of the vertical component. In the previous studies of small explosion seismology, this kind of the diagram has been drawn usually by picking up untouched peaks and troughs on the actual records. But these wave forms are often much disturbed by many "noises". In the present study, Fig. 74 was obtained after smoothing the wave form. Observed phase and group velocities were calculated from this travel time diagram. From the records of the radial component, only group velocities of wave group III' were calculated.

In Fig. 75, two structural models discussed here are shown, and theoretical dispersion curves for these models are given in Fig. 76, Fig. 77 and Fig. 78. CASE-II is based on the analysis by OHTA et al.<sup>47)</sup> of the refraction measurement which was carried out in the same field discussed here. As mentioned later, this model is satisfactory to explain the dispersion of observed wave trains. A revised model, CASE-II', was proposed to get better

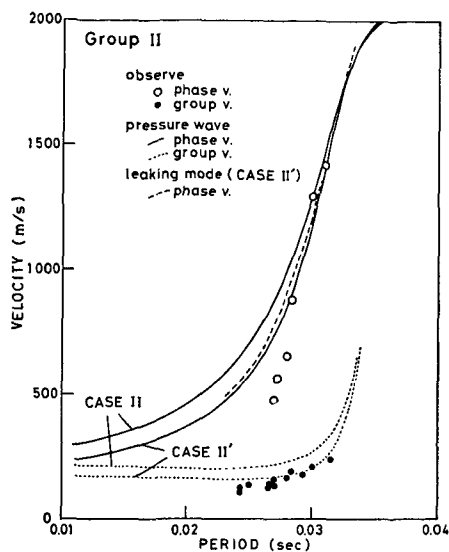


Fig. 76

Fig. 76. The dispersion of wave group II. A dashed line is the dispersion curve of the leaking mode for CASE-II'.

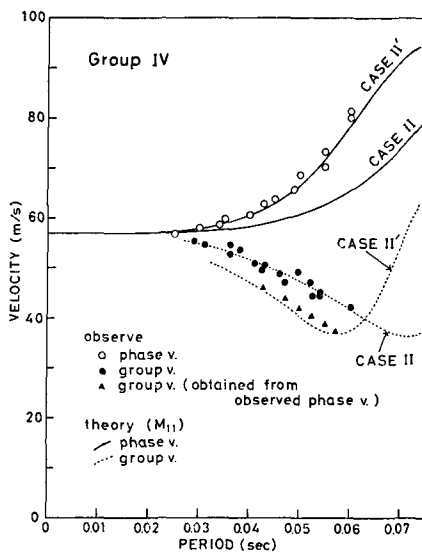


Fig. 77

Fig. 77. The dispersion of wave group IV. Solid and dotted lines are the dispersion curves of  $M_{11}$  wave for CASE-II and CASE-II'.

results.

The observed and theoretical dispersions of wave group II are shown in Fig. 76. Solid and dotted lines indicate theoretical phase and group velocities of the pressure wave, respectively. Better results have been obtained from CASE-II', mainly because of the smaller compressional wave velocity in the uppermost layer. The approximate phase velocity of the leaking mode for CASE-II' was also computed by the usual way, and is represented by a dashed line in Fig. 76. The agreement between the dispersion curves of the pressure wave and the leaking mode is good. Again this result suggests that wave group II observed at "wet" field can be easily analyzed by taking it as the pressure wave. Small discrepancies between observed and theoretical dispersions at the shorter period may be decreased if any velocity gradient is introduced in the surface layer.

The observed and theoretical dispersions of wave group IV are shown in Fig. 77. Solid and dotted lines are theoretical phase and group velocities of  $M_{11}$  wave. As to CASE-II, the theoretical group velocity fits to observed one very well, but the period of the theoretical phase velocity is formidably larger

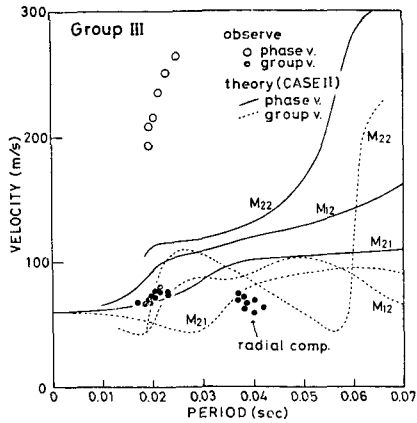


Fig. 78. The dispersion of wave group III. Solid and dotted lines are dispersion curves of the higher modes for CASE-II.

than that of observed data. Therefore, the group velocity  $\blacktriangle$  has been obtained from the graphic differentiation of the observed phase velocity  $\circ$ . But  $\blacktriangle$  does not agree with the group velocity  $\bullet$  observed directly. This means that no structural models can be satisfied by both phase and group velocities at the same time for wave group IV. This strange situation is probably due to the lateral change of the under-ground structure. As to CASE-II', the theoretical phase velocity fits very well to the observed data because of the thinner surface layer.

It is remarkable that the shear wave velocity 60 m/s in the surface layer was successfully determined by OHTA et al. As illustrated in Fig. 77, observed values of phase and group velocities are converged upon a velocity of 57 m/s which corresponds to the velocity of the free Rayleigh wave.

Dispersions of wave group III are represented in Fig. 78. It may be soon understood that wave group III in Figs. 73 (a) and (b) must be any higher mode of Rayleigh type surface waves. Theoretical curves of higher modes have been calculated only for  $M_{21}$ ,  $M_{12}$  and  $M_{22}$  waves, because no quantitative discussions seem to be possible about these higher modes.

Another example of the analysis of wave group II has been given in the study by TAZIME, YOSHII and IGARASHI<sup>9)</sup>. In this study, wave group II was approximately analyzed as the pressure wave, and good agreement between the observation and the theory was also obtained.

## 6. Dispersed water waves observed on the continental shelf of East China Sea.

During the experiment of seismic refraction profiles on the continental shelf of East China sea, under US-Japan cooperative science program, two records of dispersed water waves were obtained. These records will be analyzed in this section.

In Fig. 79, the locations of the seismic refraction profiles near the Nansei Shoto island arc are shown. The crustal structure derived from these profiles is shown in Fig. 80<sup>(48)</sup>. Two records of dispersed water waves were obtained in Profile 13 which was located on the continental shelf of East China Sea. Traced records are shown in Fig. 81. Shooting and receiving points are indicated by **S** and **R** in Fig. 79. Arrival times of direct water waves were determined from the records of the high frequency channel. These arrival times, 39.91 and 36.33 seconds, give the shot distances of 61.1 and 55.6 km respectively. Sound velocity in sea water is 1.530 km/s. Charge sizes of explosives were 384 and 288 lbs (TNT) and these were exploded on the sea bottom because of very shallow sea water, about 130 m.

Receiving and shooting ships were Konan-maru No. 23 and Vema respectively. The output signal from the hydrophone was amplified by the amplifier having three channels. The records shown in Fig. 81 are those from the low frequency channel.

The records clearly indicate two different features of dispersion, namely

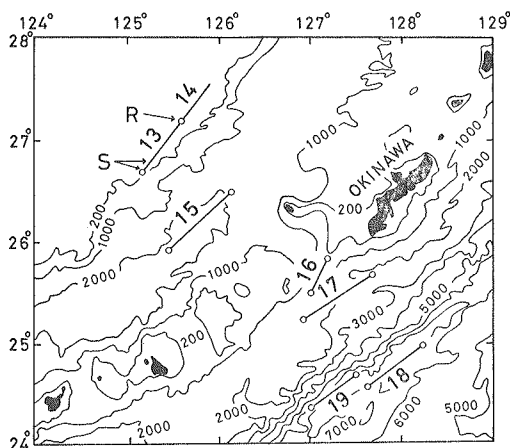


Fig. 79. Locations of seismic refraction profiles. **R** and **S** indicate the receiving and shooting points of the records discussed here.

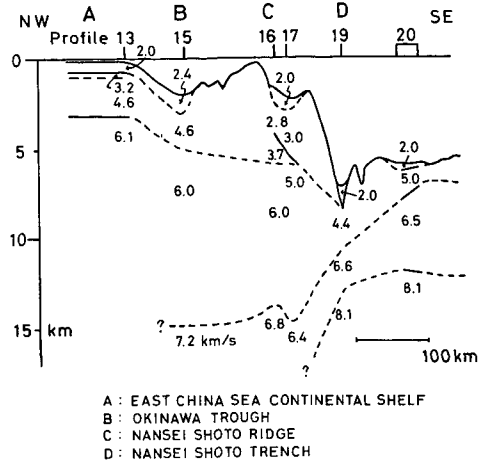


Fig. 80. Crustal structure derived from the seismic refraction analysis. (after MURAUCHI et al.<sup>48)</sup>)

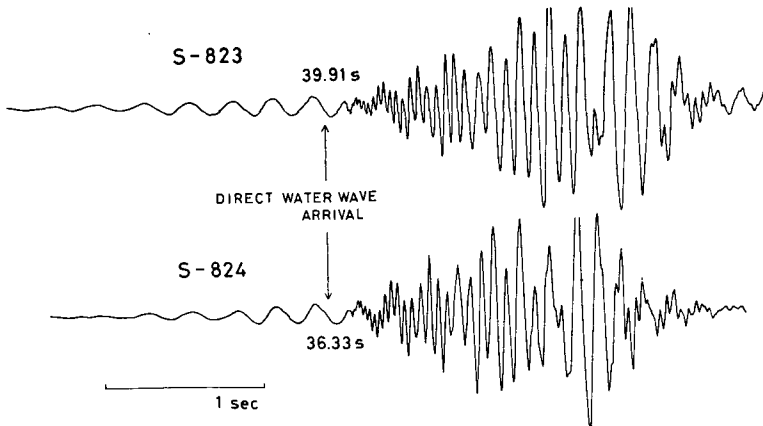


Fig. 81. Traced records of Shot-823 and Shot-824 in Profile 13. Direct water wave arrivals were determined from the records of the high frequency channel.

the inverse and the normal dispersion. These two groups seem to make up the Airy phase. In order to separate the wave train of normal dispersion having longer periods from that of inverse dispersion, middle points of short period swings were traced. Group velocities are represented in Fig. 82. The group velocities from two records fit to each other very well, and the accuracy of them may be better than  $\pm 0.5\%$ .

Since the longest period of observed data is about 0.3 seconds, these

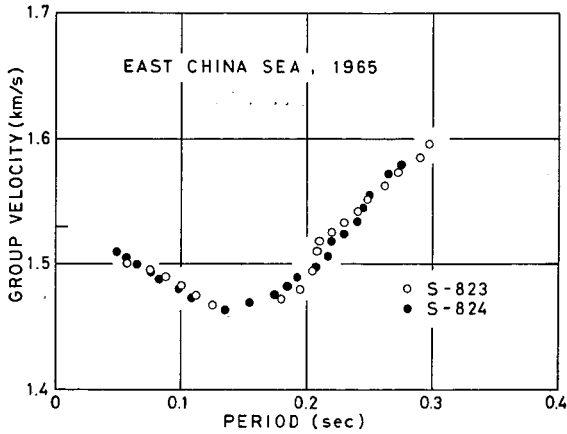


Fig. 82. Observed group velocities obtained from the records in Fig. 81.

dispersed waves mainly depend on the shallow sedimentary layer, probably shallower than 500 m. In general, the shallow sedimentary layer is characterized by the small shear wave velocity or small rigidity<sup>49)</sup>. This character allows us to neglect the shear wave in the sedimentary layer, approximately. This kind of the dispersed wave is called the pressure wave or the liquid wave.

The theory of the pressure wave has been discussed in detail by PEKERIS<sup>23)</sup>, but he gave the period equations only for the one or two layered model. These are not enough to discuss the detailed velocity structure in the sedimentary layer. Dispersion curves for more complicated models were shown by SATO<sup>50)</sup>, but his method of the computation was rather complicated. The matrix method for this problem has been given by DORMAN<sup>51)</sup>, and this method is used in the present study after some modifications.

The layer matrix for  $m$ 'th layer is

$$l_m = \begin{bmatrix} \cos P_m & i(r_{\alpha m}/\rho_m) \sin P_m \\ i(\rho_m/r_{\alpha m}) \sin P_m & \cos P_m \end{bmatrix} \quad (9)$$

where

$$r_{\alpha m} = \begin{cases} ((c/\alpha_m)^2 - 1)^{1/2} & \text{for } c > \alpha_m \\ -i(1 - (c/\alpha_m)^2)^{1/2} & \text{for } c < \alpha_m \end{cases}$$

and

$$P_m = kr_{\alpha m} H_m .$$

The period equation takes the following form,

$$\Delta = r_{\alpha n}(L)_{21} + \rho_n(L)_{11} = 0 . \quad (10)$$

Suffix  $n$  indicates the value in the half space.  $L$  is the product of layer matrixes, namely

$$L = l_{n-1} \cdots l_2 \cdot l_1. \quad (11)$$

The phase velocity curve is obtained from the solution of the equation (10).

The group velocity was calculated analytically in the present study in the following manner<sup>46)</sup>. The fundamental equation is

$$U = c + k \cdot \frac{dc}{dk} = c - k \cdot \frac{\partial \mathcal{A}(c, k)}{\partial k} \bigg/ \frac{\partial \mathcal{A}(c, k)}{\partial c}. \quad (12)$$

Now, we assume that  $(A)'$  indicates a matrix whose elements are partial derivatives of the elements of a matrix  $A$ . "Differentiated matrix"  $F'$  can be written as follows,

$$F' = r_{\alpha n}((L)')_{21} + r_{\alpha n}'(L)_{21} + \rho_n((L)')_{11}. \quad (13)$$

If we allow a relation,  $L_s = l_s \cdots l_1$ , then

$$(L_s)' = l_s(L_{s-1})' + (l_s)'L_{s-1} \quad (s = 2, 3, \dots, n-1). \quad (14)$$

When we substitute roots of  $\mathcal{A}=0$  into the equation (14), we can finally obtain  $(L_{n-1})'$ , namely  $(L)'$ . Using this  $(L)'$  and equation (13), we can calculate the group velocity by (12).

"Differentiated matrixes" are

$$\frac{\partial}{\partial k} (l_m) = \begin{bmatrix} -H_m r_{\alpha m} \sin P_m & i r_{\alpha m}^2 H_m \rho_m^{-1} \cos P_m \\ i \rho_m H_m \cos P_m & -H_m r_{\alpha m} \sin P_m \end{bmatrix} \quad (15)$$

$$\frac{\partial}{\partial c} (l_m) = \frac{c}{\alpha_m^2} \begin{bmatrix} -k H_m r_{\alpha m}^{-1} \sin P_m & i \rho_m^{-1} (r_{\alpha m}^{-1} \sin P_m + k H_m \cos P_m) \\ i \rho_m r_{\alpha m}^{-2} (-r_{\alpha m}^{-1} \sin P_m + k H_m \cos P_m) & -k H_m r_{\alpha m}^{-1} \sin P_m \end{bmatrix}. \quad (16)$$

In the case of  $c = \alpha_m$

$$\frac{\partial}{\partial k} (l_m) = \begin{bmatrix} 0 & 0 \\ i \rho_m H_m & 0 \end{bmatrix} \quad (17)$$

$$\frac{\partial}{\partial c} (l_m) = c^{-1} \begin{bmatrix} -(k H_m)^2 & 2i k H_m \rho_m^{-1} \\ -i \rho_m (k H_m)^3/3 & -(k H_m)^2 \end{bmatrix}. \quad (18)$$

The structure of Profile 13 shown in Fig. 80 has the sedimentary layer having sound velocities of 2.0 and 3.2 km/s. In general, the deep sea seismic refraction measurement is not enough to determine the detailed

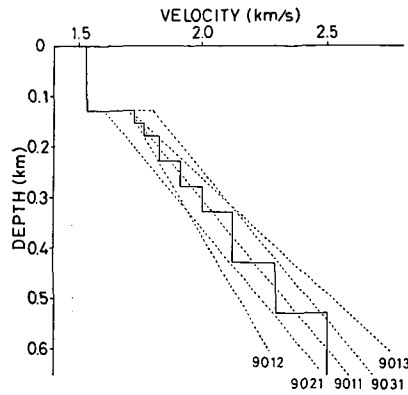


Fig. 83. Velocity distributions of five liquid models. The detail is illustrated only for Model 9011.

Table 11. Elastic constants of five models.

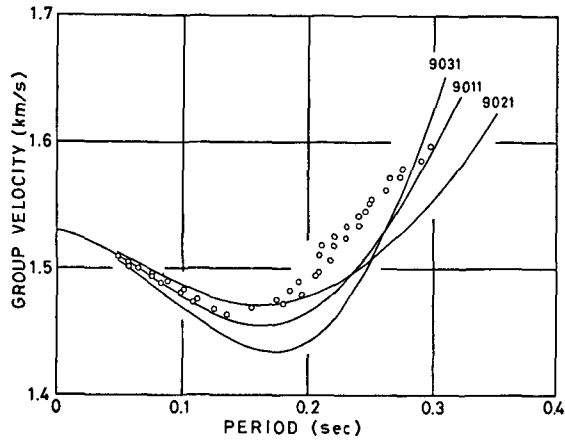
| m | H     | 9011     |        | 9021     |        | 9031     |        | 9012     |        | 9013     |        |
|---|-------|----------|--------|----------|--------|----------|--------|----------|--------|----------|--------|
|   |       | $\alpha$ | $\rho$ |
| 1 | 0.13  | 1.53     | 1.02   | 1.53     | 1.02   | 1.53     | 1.02   | 1.53     | 1.02   | 1.53     | 1.02   |
| 2 | 0.025 | 1.725    | 1.77   | 1.625    | 1.70   | 1.825    | 1.83   | 1.715    | 1.765  | 1.73     | 1.775  |
| 3 | 0.025 | 1.765    | 1.80   | 1.665    | 1.73   | 1.865    | 1.85   | 1.745    | 1.79   | 1.785    | 1.81   |
| 4 | 0.05  | 1.825    | 1.83   | 1.725    | 1.775  | 1.925    | 1.875  | 1.79     | 1.81   | 1.865    | 1.85   |
| 5 | 0.05  | 1.91     | 1.865  | 1.81     | 1.82   | 2.01     | 1.91   | 1.85     | 1.84   | 1.975    | 1.895  |
| 6 | 0.05  | 2.00     | 1.905  | 1.90     | 1.86   | 2.10     | 1.945  | 1.91     | 1.865  | 2.085    | 1.94   |
| 7 | 0.1   | 2.125    | 1.95   | 2.025    | 1.91   | 2.225    | 1.985  | 2.00     | 1.905  | 2.25     | 2.00   |
| 8 | 0.1   | 2.295    | 2.015  | 2.195    | 1.975  | 2.395    | 2.045  | 2.12     | 1.95   | 2.47     | 2.07   |
| 9 | INF   | 2.50     | 2.08   | 2.40     | 2.05   | 2.60     | 2.105  | 2.26     | 2.00   | 2.73     | 2.14   |

m; layer number, H; layer thickness (km),  
 $\alpha$ ; compressional wave velocity (km/s),  $\rho$ ; density (g/cm<sup>3</sup>).

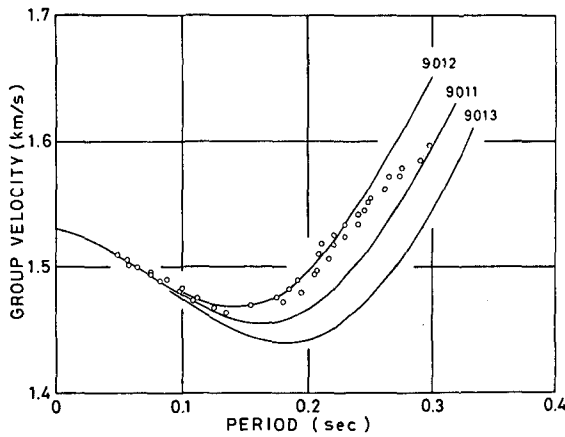
structure of the sedimentary layer. Probably, the shallow sediment such as in Profile 13 has a kind of velocity gradient. NAFE and DRAKE<sup>52)</sup> proposed the average velocity distribution in the shallower sea sediment as  $\alpha=1.70+1.70z$  where z is depth in km. In the present study, the velocity distribution was assumed to be given by a linear relation,  $\alpha=a+bz$ .

Five models were proposed for the theoretical calculation of the dispersion curve.

- 1) Model 9011;  $\alpha=1.70+1.70z$  (NAFE and DRAKE's model)
- 2) Model 9021;  $\alpha=1.60+1.70z$
- 3) Model 9031;  $\alpha=1.80+1.70z$
- 4) Model 9012:  $\alpha=1.70+1.20z$



(a)



(b)

Fig. 84. Comparison of observed data and theoretical dispersion curves for five models. (a) Models 9011, 9021 and 9031. (b) Models 9011, 9012 and 9013.

5) Model 9013;  $\alpha = 1.70 + 2.20z$

For the calculation by the matrix method, these velocity distributions were approximated by many thin layers as illustrated in Fig. 83. Detailed elastic constants of these models are tabulated in Table 11. The density in this table is based on NAFE and DRAKE's study.

Fig. 84 (a) gives the theoretical group velocity curves for Models 9011, 9021 and 9031 together with the observed data. These models have a same value of the velocity gradient, namely  $b = 1.70 \text{ s}^{-1}$ . When we restrict

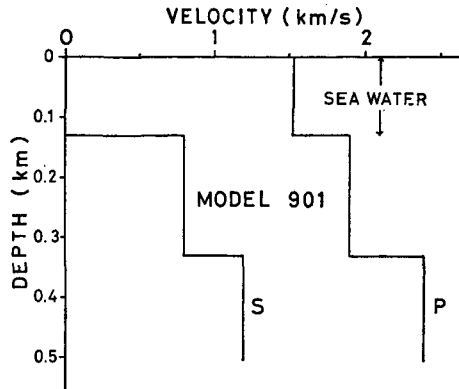


Fig. 85. Velocity distribution with depth of Model 901.

Table 12. Elastic constants of Model 901.

| $m$ | $H$  | $a$  | $\beta$ | $\rho$ |
|-----|------|------|---------|--------|
| 1   | 0.13 | 1.53 | —       | 1.02   |
| 2   | 0.20 | 1.90 | 0.80    | 1.80   |
| 3   | INF  | 2.40 | 1.20    | 2.30   |

$\beta$  ; shear wave velocity (km/s)

our attention to the shorter period portion, we can find the best agreement between the theory and the observation for Model 9011. This result suggests that the best value of  $a$  is about 1.70 km/s, because this shorter period portion may depend mainly on the shallower structure.

Theoretical group velocity curves for Models 9011, 9012 and 9013 are shown in Fig. 84 (b). Since these curves are abruptly converged in the shorter period, the determination of  $a=1.70$  in Fig. 84 (a) seems to be good. In the period range of 0.04–0.25 seconds, the best result was obtained for Model 9012 whose velocity distribution is  $a=1.70+1.20z$ . Beyond about  $T=0.25$  seconds, the theoretical curve for Model 9012 deviates from observed data. Probably, it is due to the deeper structure or the influence of the shear wave.

When we consider the influence of the shear wave in the discussion of the water wave, this wave must be treated as a kind of the leaking mode because the shear wave velocity in the shallower sediment may be less than the sound velocity in sea water. A simple model 901, shown in Fig. 85 and Table 12, was proposed for the analysis of the influence of the shear wave. In this

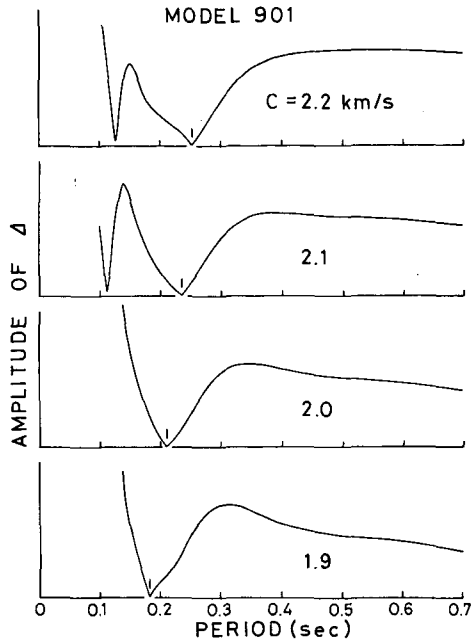


Fig. 86. Calculated examples of absolute values of the period function for Model 901. The ordinate is the arbitrary linear scale.

model, the shear wave velocity in the half space is less than the sound velocity in the water layer, and the period equation has no real roots in the region of  $c > \alpha_1 > \beta_3$ .

Calculated examples of the absolute value of the period function for Model 901 are illustrated in Fig. 86. A  $4 \times 4$  elements matrix for the liquid layer used in this calculation is as follows<sup>53</sup>,

$$a_m = \begin{pmatrix} 1 & 0 & 0 & 0 \\ 0 & \cos P_m & i r_{\alpha m} (\rho_m c^2)^{-1} \sin P_m & 0 \\ 0 & i r_{\alpha m}^{-1} \rho_m c^2 \sin P_m & \cos P_m & 0 \\ 0 & 0 & 0 & 1 \end{pmatrix} \quad (19)$$

The abscissa of this figure means period and the ordinate is the arbitrary linear scale. Two pairs of sharp minima of  $|A|$  can be found in this figure, and the minima of the longer period may correspond to the water wave discussed here. Those of the shorter period may be a higher mode.

In Fig. 87,  $|A|$  is illustrated with contour lines. A very sharp "trough"

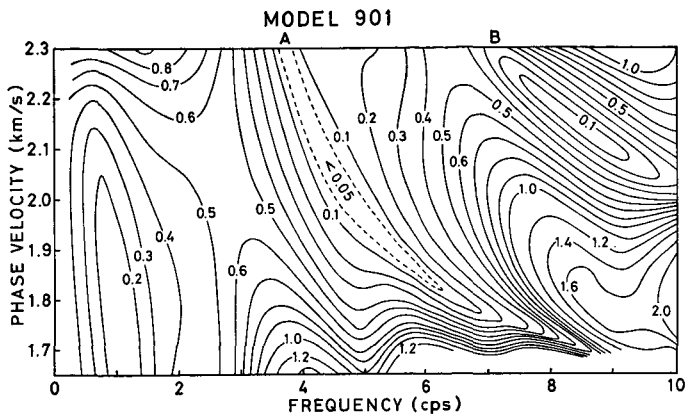


Fig. 87. Distribution of the absolute value of the period function represented with contour lines for Model 901. The dispersion curve of the leaking mode is obtained by tracing a sharp "trough".

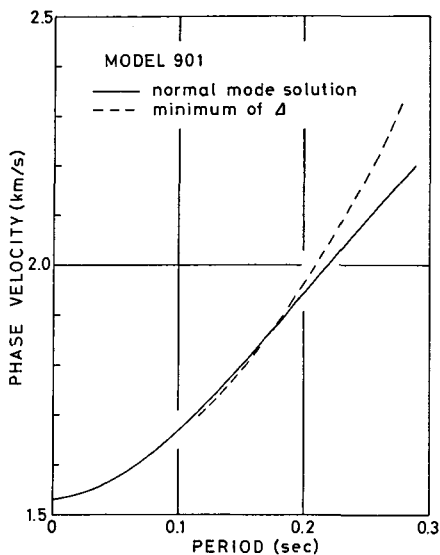


Fig. 88. Theoretical phase velocity curves for Model 901. Solid and dashed lines indicate the pressure wave and the leaking mode respectively.

designated by **A** corresponds to the water wave. This trough is also shown in Fig. 88 as the dispersion curve of the leaking mode. The solid line in this figure is the dispersion curve of the pressure wave calculated by neglecting the shear wave in Model 901. These two curves are very close to each other

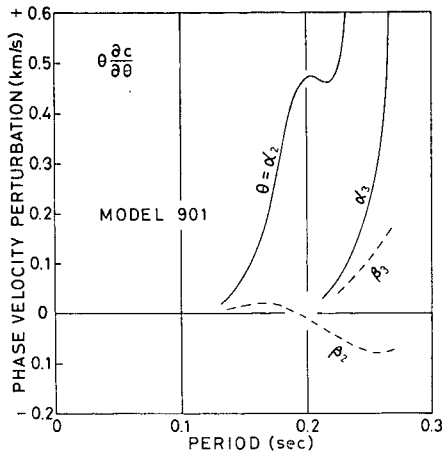


Fig. 89. Phase velocity perturbations with respect to small changes of parameters for Model 901.

in the longer period. This result suggests that the approximation of water wave as the pressure wave is reasonable at least in the shorter period.

In Fig. 89 the phase velocity perturbation with respect to small changes of four parameters,  $\alpha_2$ ,  $\alpha_3$ ,  $\beta_2$  and  $\beta_3$  for Model 901 are given. These perturbations can be calculated analytically for Love and Rayleigh waves<sup>54),55)</sup>, but no methods have been given for the leaking mode. Curves in Fig. 89 were calculated by the numerical method<sup>56)</sup>.

The accuracy of these curves is not so high because they were calculated from small differences of the "approximate" dispersion curves. As shown in Fig. 89, perturbations with respect to the compressional wave are a few times of those with respect to the shear wave, i.e., the dispersion of the water wave is almost controlled by the compressional wave distribution. This property of the water wave is very similar to that of PL wave.

The dispersion curve of the leaking mode for a more realistic model 9012L is shown in Fig. 90. Elastic constants of this model are tabulated in Table 13, and are exactly same to those of Model 9012 except for the shear wave. A solid line is the phase velocity of the pressure wave for Model 9012. Solid and open circles represent the three sets of observed phase velocities obtained under an assumption of the same source condition for two explosive shots. Since this assumption is somewhat doubtful, no detailed discussions on this figure will be given here. But, the dispersion curve of the leaking mode appears to well explain the observed data.

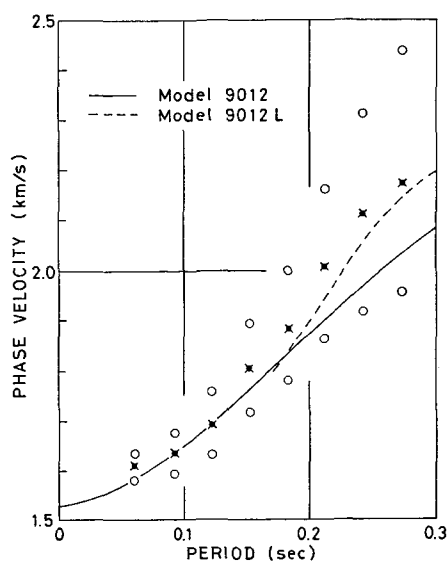


Fig. 90. Theoretical phase velocity curves for Models 9012 and 9012L. Open and solid circles are observed phase velocities.

Table 13. Elastic constants of Model 9012L.

| $m$ | $H$   | $\alpha$ | $\beta$ | $\rho$ | $\sigma$ |
|-----|-------|----------|---------|--------|----------|
| 1   | 0.13  | 1.53     | —       | 1.02   | (0.5)    |
| 2   | 0.025 | 1.715    | 0.66    | 1.765  | 0.413    |
| 3   | 0.025 | 1.745    | 0.70    | 1.79   | 0.404    |
| 4   | 0.05  | 1.79     | 0.75    | 1.81   | 0.393    |
| 5   | 0.05  | 1.85     | 0.82    | 1.84   | 0.378    |
| 6   | 0.05  | 1.90     | 0.89    | 1.865  | 0.361    |
| 7   | 0.1   | 2.00     | 0.99    | 1.905  | 0.338    |
| 8   | 0.1   | 2.12     | 1.13    | 1.95   | 0.302    |
| 9   | INF   | 2.26     | 1.30    | 2.00   | 0.253    |

$\sigma$ ; Poisson's ratio

No comparisons between the observed group velocity and the theoretical one of the leaking mode are given in the present study. As shown in Fig. 82 observed group velocities have very high accuracy. On the other hand, such an accurate theoretical curve as observed one cannot be calculated by the approximate method.

Since the determination of the velocity distribution in the sedimentary layer is a very important problem, many methods have been developed for this purpose. NAFE and DRAKE'S study is based on the refraction measure-

ments and the rock sampling. An well known technique is that using the wide angle reflection in the sedimentary layer. This method was first represented by HILL<sup>57)</sup>.

Surface waves also have been analyzed in order to study the property of the sedimentary layer. It is well known that the existence of the sedimentary layer of low rigidity causes the great effect on the dispersion of higher Rayleigh modes on the oceanic path<sup>58)</sup>. But this kind of the observation is not enough to determine the detailed structure of the sediment. DAVIES<sup>59)</sup> observed Stoneley waves by the hydrophone on the sea bottom, and determined the velocity distribution in the very shallow sediment.

The common weak point in surface wave methods is that the effect of the compressional wave and the shear wave cannot be separate. Also in the present study, the effect of the shear wave on the dispersion of the water wave is very small but cannot be neglected particularly in the longer period. Since the accurate calculation of the leaking mode is very difficult, the "pressure wave approximation" is the best way to analyze the water wave, at present.

### **7. Some comparisons of complex roots and approximate solutions.**

The main aim of the present study is to represent the utility of two approximate methods for the leaking mode. As shown in the previous sections, approximate dispersion curves were successfully applied to the dispersion analyses of various leaking modes. However the discussions on excitation or attenuation of the leaking mode may need more "strict" solutions. It was already mentioned in § 2 that there was a big problem in the complex root solution. This problem may be expressed in another way as follows; what is the most reasonable additional condition under which complex roots of the period equation should be calculated? We must discuss this problem in the field of the observation as well as of mathematics.

In spite of the vagueness mentioned above, it was also represented in § 4.2 that observed attenuation of a leaking mode could be well explained by the imaginary part of the complex root. In the present section, some comparisons of complex roots and approximate solutions are given. These complex roots were calculated under the condition of  $\text{Im}(k)=0^{13)}$ . Since complex roots for PL waves were discussed by GILBERT and the other authors, the discussions in this section are confined mainly in high velocity layer models. The computer program of the present author is written by using the

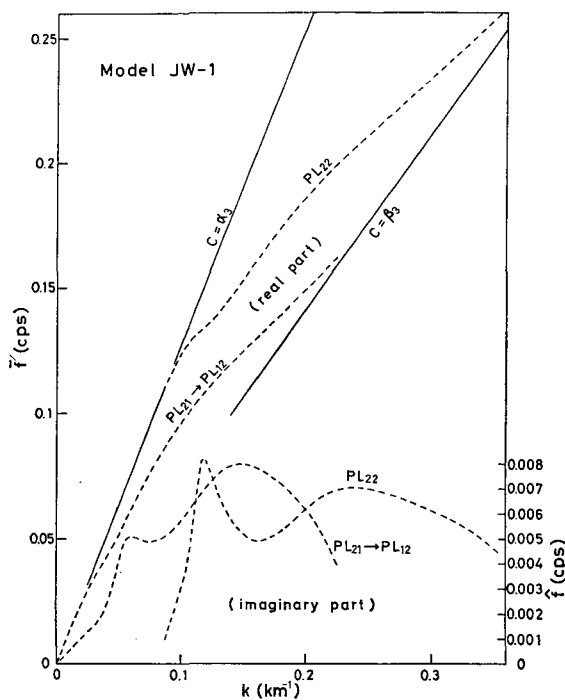


Fig. 91. Complex roots for Model JW-1. All these roots are on the (+, -) sheet.

matrix method, and the complex root is traced by referring to approximate solutions.

The calculated example for Model JW-1 is shown in Fig. 91. Since the period equation can be expressed as  $\Delta(k, \bar{f}, \hat{f})=0$  under GILBERT's condition, the abscissa and the ordinate are taken as  $k$  and  $\bar{f}$  or  $\hat{f}$ , respectively. The scale for  $\hat{f}$  is largely exaggerated because  $\hat{f}$  is much smaller than  $\bar{f}$ . Complex roots illustrated in this figure are all on the (+, -) sheet.

The comparison of this figure and GILBERT's result for a single layered model leads us to following conclusions; the dispersion curve of  $PL_{22}$  is almost equivalent to that of  $\bar{P}_{-+}$  mode in GILBERT's paper, but the  $PL_{21}$  and  $PL_{12}$  are connected to each other and are made into a single curve. This situation is clearly illustrated in Fig. 92. In this figure, phase velocity  $c$  was defined as  $c=2\pi\bar{f}/k$  by using the real part of complex frequency.

LASTER et al.<sup>14)</sup> computed complex roots for a single layered model under their additional condition  $\text{Im}(f)=0$  and GILBERT's condition  $\text{Im}(k)=0$ ,

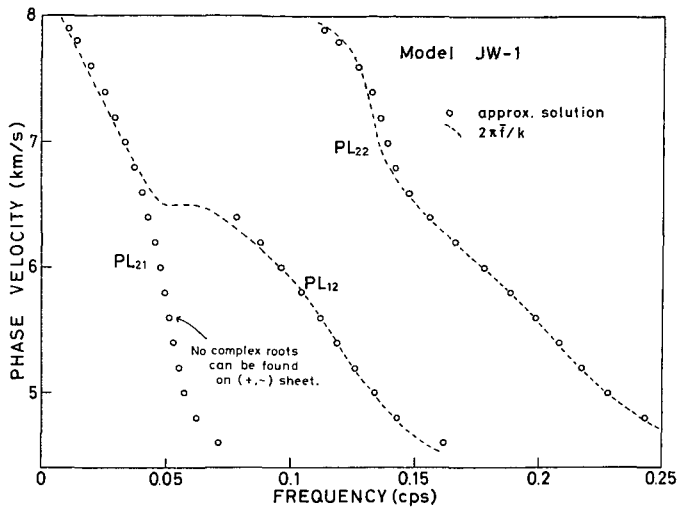


Fig. 92. Phase velocity dispersion curves for Model JW-1. Dashed lines indicate the phase velocity defined by the real part of the complex root.

and found much difference between two results. They concluded that this difference might be due to the additional condition. However the solution by LASTER et al. obtained under the former condition is similar to that shown in Fig. 92 which was calculated under the latter condition. This result may suggest that the situation is not so simple as that mentioned by LASTER et al. As illustrated in Fig. 92, dispersion curves from the complex root well consist with approximate solutions except for a transition from  $PL_{21}$  to  $PL_{12}$ . No complex roots corresponding to approximate solutions of  $PL_{21}$  in  $c < 6.5$  could be found on the  $(+, -)$  sheet. It is an interesting problem how is the continuation of  $M_{21}$  wave in the leaking mode region.

Complex roots for AL-PL model are shown in Fig. 93. The complex root on the  $(+, -)$  sheet has already been represented in Fig. 56. Approximate solutions in  $c > a_2$  correspond to complex roots on the  $(-, -)$  sheet. The leaking mode in this region must leak its energy of the compressional wave as well as that of the shear wave. This special nature is also suggested by the rather large imaginary part of the complex root. This large imaginary part may cause remarkable attenuation which is equivalent to  $Q \approx 10$ .

The phase velocity in Fig. 94 was also defined by the real part of the complex root. For the complex root on the  $(+, -)$  sheet, large deviation from the approximate solution can be found especially in the higher

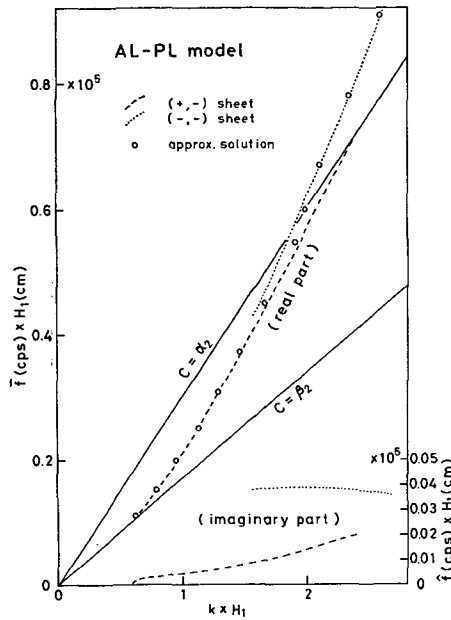


Fig. 93. Complex roots for AL-PL model. Dashed and dotted lines indicate complex roots on the (+, -) and (-, -) sheets respectively.

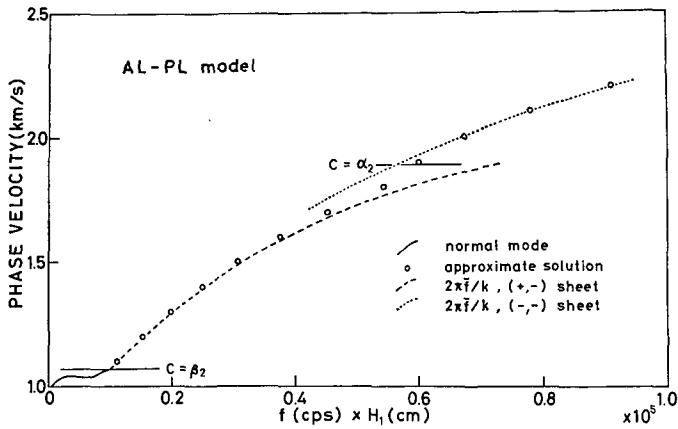


Fig. 94. Phase velocity dispersion curves for AL-PL model.

frequency region. It is also remarkable that the observed phase velocity from model seismology (§ 4.2) is more consistent with these approximate solutions than the "strict" dispersion curve (see Fig. 54).

Dispersion curves for AL-LAM model are given in Figs. 95 and 96.

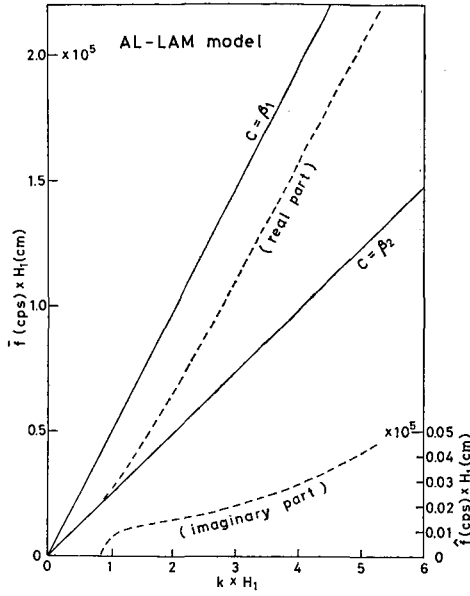


Fig. 95. Complex roots for AL-LAM model. Dashed lines indicate complex roots on the (+, -) sheet.

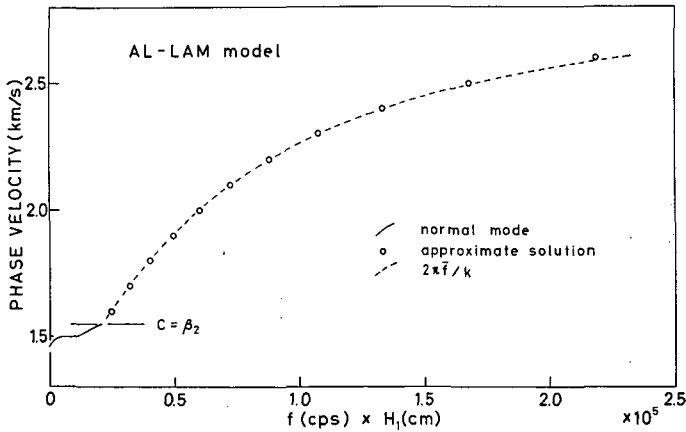


Fig. 96. Phase velocity dispersion curves for AL-LAM model.

The form of  $\hat{f}$  is similar to that for AL-PL model. The agreement between dispersion curves from complex roots and from approximate solutions is very good.

In Figs. 97, 98 and 99, the comparisons of approximate solutions and

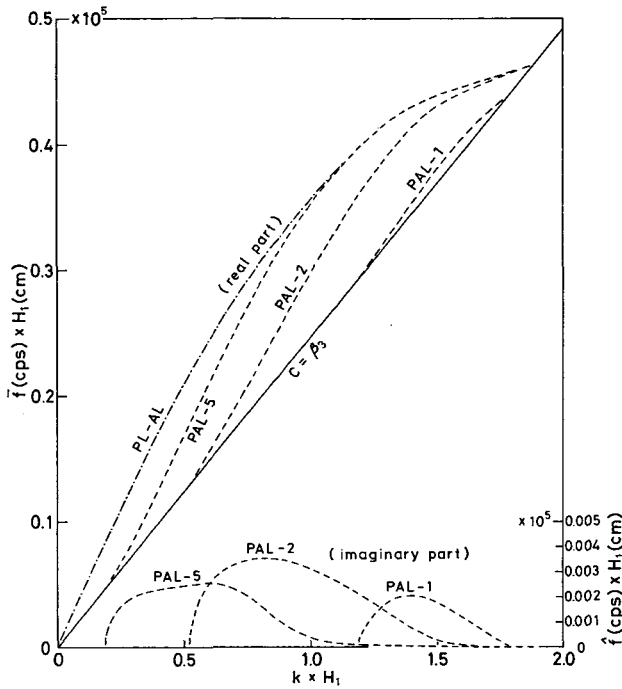


Fig. 97. Complex roots on the (+, -) sheet for PAL-models.

complex roots for PAL-models are represented. The agreements are remarkable. It is very interesting that the imaginary parts of PAL-5 and PAL-2 are very small where dispersion curves for these models are very close to that for PL-AL model. Leaking modes in these parts may have the nature of the “quasi-normal mode”. In Fig. 99 the period function for PAL-1 is illustrated with contour lines as in Fig. 40. The dispersion curve defined by the real part of the complex root is located just at the centre of a sharp trough.

### 8. Summary

As represented in the previous sections, it became obvious that two approximate methods were very useful tools for the analyses of leaking modes. Though the theory of the leaking mode is vague at present, many records of leaking modes have been accumulated. This situation may allow us to make use of these two methods. In order to reduce the vagueness of the theory, model experiments are very important because they provide the “ideal” observed data. Since the agreement between “approximate” solutions and the

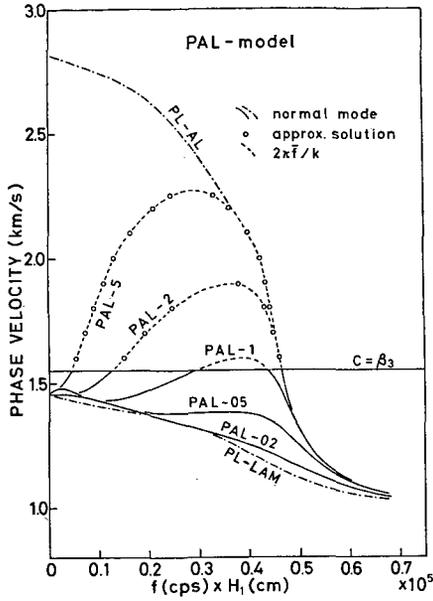


Fig. 98. Phase velocity curves for PAL-models.

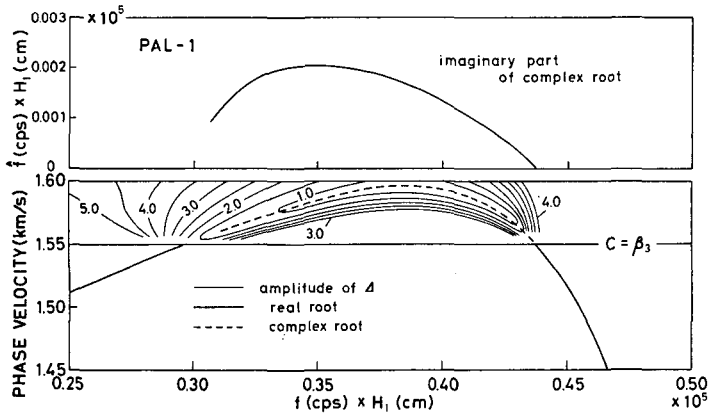


Fig. 99. Detailed comparison of the complex root and the approximate solution for PAL-1. The absolute value of the period function is illustrated with contour lines in  $c > \beta_3$ .

observed data of the model experiments (§3.1 and §4.2) was remarkable, now the adjective “approximate” seems to be unnecessary. It is very interesting that the complex root solution is not always strict physically in the leaking

mode problem.

PL wave is the most popular leaking mode but Japan islands is not a suitable field for the analysis of this wave because of its structural complexity. In § 3.2.2 theoretical curves for only JW-1 were compared with observed data. More detailed discussions on the crustal structure may be possible by making use of accurate observed data of the phase velocity.

The problem of wave propagation on high velocity layer models in the present paper is very interesting and unique. Wave propagation on the sandwiched high velocity layer models has very strange characteristics and this problem may be good as a theme in model seismology.

One of the most exciting part in this report is model seismology on wave propagation on the superficial high velocity layer models. Dispersions and attenuation of the wave trains were well explained by approximate solutions and complex roots.

The discussions on wave group II represented in § 5 made it obvious that this wave can be analyzed approximately as the pressure wave, though this has been understood vaguely. The approximate methods have not so good resolution power in the problem like wave group II. But the most "effective" part of the dispersion curve was emphasized by this "poor" resolution. The result that wave group II in the "wet" field can be treated approximately as the pressure wave allows us to study the P wave structure by using the surface wave.

#### **Appendix; Summary of the approximate dispersion curve of the leaking mode.**

As mentioned in the previous part of this paper, OLIVER and MAJOR's method is carried out by tracing the minimum of the absolute value of the period function  $\Delta$ . HASKELL<sup>17)</sup> has used the matrix method to express this period function for Rayleigh type surface waves.

$$\Delta = (J_{22} - J_{12})(J_{31} - J_{41}) - (J_{11} - J_{21})(J_{42} - J_{32}) \quad (\text{A-1})$$

where  $J_{ij}$  is the element of following matrix  $J$ ,

$$J = E_n^{-1} \cdot a_{n-1} \cdot a_{n-2} \cdots a_1. \quad (\text{A-2})$$

Symbols  $E_n^{-1}$  and  $a_m$  indicate the  $4 \times 4$  elements matrixes where suffix  $m$  is the layer number and  $n$  corresponds to the half space.

$$E_n^{-1} = \begin{pmatrix} -2(\beta_n/\alpha_n)^2 & 0 & (\rho_n \alpha_n^2)^{-1} & 0 \\ 0 & c^2(\gamma_n - 1)/\alpha_n^2 r_{\alpha n} & 0 & (\rho_n \alpha_n^2 r_{\alpha n})^{-1} \\ (\gamma_n - 1)/\gamma_n r_{\beta n} & 0 & -(\rho_n c^2 \gamma_n r_{\beta n})^{-1} & 0 \\ 0 & 1 & 0 & (\rho_n c^2 \gamma_n)^{-1} \end{pmatrix} \quad (\text{A-3})$$

and,

$$\begin{aligned} (a_m)_{11} &= \gamma_m \cos P_m - (\gamma_m - 1) \cos Q_m \\ (a_m)_{12} &= i((\gamma_m - 1)r_{\alpha m}^{-1} \sin P_m + \gamma_m r_{\beta m} \sin Q_m) \\ (a_m)_{13} &= -(\rho_m c^2)^{-1} (\cos P_m - \cos Q_m) \\ (a_m)_{14} &= i(\rho_m c^2)^{-1} (r_{\alpha m}^{-1} \sin P_m + r_{\beta m} \sin Q_m) \\ (a_m)_{21} &= -i(\gamma_m r_{\alpha m} \sin P_m + (\gamma_m - 1) r_{\beta m}^{-1} \sin Q_m) \\ (a_m)_{22} &= -(\gamma_m - 1) \cos P_m + \gamma_m \cos Q_m \\ (a_m)_{23} &= i(\rho_m c^2)^{-1} (r_{\alpha m} \sin P_m + r_{\beta m}^{-1} \sin Q_m) \\ (a_m)_{24} &= (a_m)_{13} \\ (a_m)_{31} &= \rho_m c^2 \gamma_m (\gamma_m - 1) (\cos P_m - \cos Q_m) \\ (a_m)_{32} &= i \rho_m c^2 (\gamma_m - 1)^2 r_{\alpha m}^{-1} \sin P_m + \gamma_m^2 r_{\beta m} \sin Q_m \\ (a_m)_{33} &= (a_m)_{22} \\ (a_m)_{34} &= (a_m)_{12} \\ (a_m)_{41} &= i \rho_m c^2 (\gamma_m^2 r_{\alpha m} \sin P_m + (\gamma_m - 1)^2 r_{\beta m}^{-1} \sin Q_m) \\ (a_m)_{42} &= (a_m)_{31} \\ (a_m)_{43} &= (a_m)_{21} \\ (a_m)_{44} &= (a_m)_{11} \end{aligned} \quad (\text{A-4})$$

where,

$$r_{\alpha m} = \begin{cases} ((c/\alpha_m)^2 - 1)^{1/2} & c > \alpha_m \\ -i(1 - (c/\alpha_m)^2)^{1/2} & c < \alpha_m \end{cases} \quad (\text{A-5})$$

$$r_{\beta m} = \begin{cases} ((c/\beta_m)^2 - 1)^{1/2} & c > \beta_m \\ -i(1 - (c/\beta_m)^2)^{1/2} & c < \beta_m \end{cases} \quad (\text{A-6})$$

$$\gamma_m = 2(\beta_m/c)^2 \quad (\text{A-7})$$

$$P_m = k r_{\alpha m} H_m \quad (\text{A-8})$$

$$Q_m = k r_{\beta m} H_m \quad (\text{A-9})$$

SU and DORMAN's method is based on HASKELL's surface displacement spectrum<sup>16)</sup> due to incident P or SV waves from the half space to the layers.

For incident P waves,

$$U_p = F_1(J_{42} - J_{32})/A \quad (A-10)$$

$$W_p = F_2(J_{41} - J_{31})/A$$

and for incident SV waves,

$$U_s = F_3(J_{12} - J_{22})/A \quad (A-11)$$

$$W_s = F_4(J_{21} - J_{11})/A$$

where  $U$  and  $W$  indicate the horizontal and vertical components of the surface displacement spectrum.

$F_i$  are as follows;

$$F_1 = 2c^2/a_n^2$$

$$F_2 = 2c^2/a_n^2 r_{\alpha n} \quad (A-12)$$

$$F_3 = 2\gamma_n^{-1} r_{\beta n}^{-1}$$

$$F_4 = 2\gamma_n^{-1}$$

In this case,  $c$  means the phase velocity or the apparent velocity of the incident wave.

SU and DORMAN introduced a small modification on  $F_i$ , but this modification is only due to the difference of the normalization and is not essential. SU and DORMAN's modified  $F_i$  are,

$$F_1 = F_2 = 2c/a_n \quad (A-13)$$

$$F_3 = F_4 = c/\beta_n$$

Dispersion curves of the leaking mode are determined by tracing the maximum of spectra (A-10) and (A-11).

*Acknowledgement.* The author wishes to thank Professor K. TAZIME for critical reading this report and for helpful discussions. He also wishes to thank Drs. N. DEN, H. OKADA and H. HOTTA for their helpful discussions.

Numerical calculations were carried out by NEAC-2203G in Hokkaido University Computer Centre and by HITAC-5020E in Tokyo University Computer Centre.

This paper was submitted to the Hokkaido University in March 1970 as the author's doctoral thesis.

## References

- 1) YOSHII, T.: Model Seismology on PL Modes. *Geophys. Bull. Hokkaido Univ.*, **19** (1968), 65-71, (in Japanese).
- 2) YOSHII, T.: Dispersed Water Waves Observed in East China Sea Continental Shelf, *Geophys. Bull. Hokkaido Univ.*, **20** (1968), 77-89, (in Japanese).
- 3) YOSHII, T.: Characteristics of Some Types of Leaking Modes, *Geophys. Bull. Hokkaido Univ.*, **21** (1969), 117-131 (in Japanese).
- 4) YOSHII, T.: Leaking Modes in Records of Earthquakes (Part 1), *Zisin*, **22** (1969), 54-65 (in Japanese).
- 5) YOSHII, T.: Characteristics of Some Types of Leaking Modes (Part 2), *Geophys. Bull. Hokkaido Univ.*, **22** (1969), 125-135, (in Japanese).
- 6) YOSHII, T.: Leaking Modes in Records of Earthquakes (Part 2), *Zisin*, **22** (1970), 318-327 (in Japanese).
- 7) YOSHII, T. and K. SUZUKI: Model Experiments on Surface Waves Propagating in High Velocity Layer Models, *Zisin*, **22** (1969), 236-244, (in Japanese).
- 8) TAZIME, K. and T. YOSHII: A Way to Conformal Mapping of the Characteristic Equation for Love-Type Waves (4), *Zisin*, **22** (1969), 20-28, (in Japanese).
- 9) TAZIME, K., T. YOSHII and T. IGARASHI: Measurements of the Vibration of the Pier by Explosions and the Seismic Prospecting at the Bridge of Nagadoro, Aomori Prefecture, *Geophys. Bull. Hokkaido Univ.* **21** (1969), 133-150, (in Japanese).
- 10) OLIVER, J. and M. MAJOR: Leaking Modes and the PL Phase, *Bull. Seism. Soc. Amer.*, **50** (1960), 165-180.
- 11) SU, S.S. and J. DORMAN: The Use of Leaking Modes in Seismogram Interpretation and in Studies of Crust-Mantle Structure, *Bull. Seism. Soc. Amer.*, **55** (1965), 989-1021.
- 12) ROSENBAUM, J.H.: The Long-Time Response of a Layered Elastic Medium to Explosive Sound, *J. Geophys. Res.*, **65** (1960), 1577-1614.
- 13) GILBERT, F.: Propagation of Transient Leaking Modes in a Stratified Elastic Wave-guide. *Rev. Geophys.*, **2** (1964), 125-153.
- 14) LASTER, S.J. et al.: Theoretical Investigation of Modal Seismograms for a Layer over a Half-Space, *Geophysics*, **30** (1965), 571-596.
- 15) TAZIME, K.: A Way to Conformal Mapping of the Characteristic Equation for Love-Type Waves, *Zisin*, **19** (1966), 135-146, (in Japanese).
- 16) HASKELL, N.A.: Crustal Reflection of Plane P and SV Waves, *J. Geophys. Res.*, **67** (1962), 4751-4767.
- 17) HASKELL, N.A.: The Dispersion of Surface Waves on Multilayered Media, *Bull. Seism. Soc. Amer.*, **43** (1953), 17-34.
- 18) KNOPOFF, L. et al.: Wave Propagation in a Medium with a Single Layer, *J. Geophys. Res.*, **65** (1960), 265-278.
- 19) GILBERT, F. and S.J. LASTER: Experimental Investigation of PL Modes in a Single Layer, *Bull. Seism. Soc. Amer.*, **52** (1962), 59-66.
- 20) TOLSTOY, I. and E. USDIN: Dispersive Properties of Stratified Elastic and Liquid Media — A Ray Theory, *Geophysics*, **18** (1953), 844-870.
- 21) SAITO, T.: Improvement on the Equipment for Model Seismology, *Geophys. Bull. Hokkaido Univ.*, **16** (1966), 1-10, (in Japanese).
- 22) HAMADA, K.: Model Experiments on Period of Surface Waves in a Medium with a Single Layer, *Zisin*, **16** (1963), 133-144, (in Japanese).

- 23) PEKERIS, C.L.: Theory of Propagation of Explosive Sound in Shallow Water, Geol. Soc. Amer. Mem., **27** (1948).
- 24) OLIVER, J.: On the Long Period Character of Shear Waves, Bull. Seism. Soc. Amer., **51** (1961), 1-12.
- 25) OLIVER, J.: Propagation of PL Waves across the United States, Bull. Seism. Soc. Amer., **54** (1964), 151-160.
- 26) CHANDER, R. et al.: On the Synthesis of Shear-Coupled PL Waves. Bull. Seism. Soc. Amer., **58** (1968), 1849-1877.
- 27) YOSHI, T.: Crustal Structure in North-eastern Japan from Short Period Surface Wave Dispersion, Geophys. Bull. Hokkaido Univ., **19** (1968), 73-79, (in Japanese).
- 28) MATUZAWA, T. and K. SATO: Bestätigung der Existanz der Longperiodischen Schwingungen bei Grossen Erdbeben, Bull. Earthq. Res. Inst., **17** (1939), 623-626.
- 29) MATUZAWA, T.: Study of Earthquake, Uno Shoten, (1964), 206-207.
- 30) MATUZAWA, T.: Observation of Some of Recent Earthquakes and Their Time-Distance Curves (Part 1), Bull. Earthq. Res. Inst., **5** (1928), 1-28.
- 31) IMAMURA, A.: On the Destructive Tango Earthquake of March 7, 1927, Bull. Earthq. Res. Inst., **4** (1928), 179-202.
- 32) KAWASUMI, N.: Jishin-do to Jishin-kisho, Zisin, Ser. I, **4** (1933), 71-94, (in Japanese).
- 33) WADATI, K., K. SAGISAKA and K. MASUDA: On the Travel Time of Earthquake Waves (Part 1), Geophys. Mag., **7** (1933), 87-99.
- 34) AKI, K.: Crustal Structure in Japan from the Phase Velocity of Rayleigh Waves, Part 1, Bull. Earthq. Res. Inst., **39** (1961), 255-283.
- 35) KANAMORI, H.: Study on the Crust-Mantle Structure in Japan, Bull. Earthq. Res. Inst., **41** (1963), 761-776.
- 36) YOSHI, T.: Portable Long Period Seismograph, Geophys. Bull. Hokkaido Univ., **13**(1965), 115-125, (in Japanese)
- 37) HUNKINS, K. and J.T. KUO: Surface Wave Dispersion in The Tonga-Fiji Region, Bull. Seism. Soc. Amer., **55** (1965), 135-145.
- 38) OLIVER, J., F. PRESS and M. EWING: Two-Dimensional Model Seismology, Geophysics, **19** (1954), 202-219.
- 39) NAFFÉ, J.E. and J.N. BRUNE: Observation of Phase Velocity for Rayleigh Waves in the Period Range 100 to 400 seconds, Bull. Seism. Soc. Amer., **50** (1960), 427-439.
- 40) ANDERSON, D.L.: Recent Evidence Concerning the Structure and Composition of the Earth's Mantle, Physics and Chemistry of the Earth, **6** (1965), Pergamon Press, 1-131.
- 41) TAZIME, K.: Wave Groups Generated by a Very Small Explosion, J. Phys. Earth, **4** (1956), 113-126.
- 42) TAZIME, K.: Relations between Charge Amounts and Periods in Resulting Seismic Wave Groups, J. Phys. Earth, **5** (1957), 51-59.
- 43) OKADA, H.: Analyses of Seismic Waves Generated by Small Explosions, J. Fac. Sci., Hokkaido Univ., VII, **1** (1962), 460-485.
- 44) KUBOTERA, A. and Y. OHTA: On Seismic Waves Generated by Small Explosions, Spec. Contr., Geophys. Inst. Kyoto Univ., **6** (1966), 267-279.
- 45) TAZIME, K. and K. HAMADA: Transition from Dispersive Rayleigh Waves to Sound Waves in a Layer Overlying a Liquid Half Space, Zisin, **14** (1961), 63-76, (in Japanese).

- 46) HARKRIDER, D.G.: Surface Waves in Multilayered Elastic Media I, *Bull. Seism. Soc. Amer.*, **54**(1964), 627-679.
- 47) OHTA, Y. et al.: A Note on the Shear Wave Prospecting at the Premises of Geological Survey of Japan, *Bull. Geolog. Surv. Japan*, **18** (1967), 43-48, (in Japanese).
- 48) MURAUCHI, S. et al.: Crustal Structure of the Philippine Sea, *J. Geophys. Res.* **73** (1968) 3143-3171.
- 49) NAFE, J.E. and C.L. DRAKE: Physical Properties of Marine Sediments, *The Sea*, **3** (1963), 794-815.
- 50) SATO, Y.: Numerical Integration of the Equation of Motion for Surface Waves in a Medium with Arbitrary Variation of Material Constants, *Bull. Seism. Soc. Amer.*, **49** (1959), 57-77.
- 51) DORMAN, J.: Period Equation for Waves of Rayleigh Type on a Layered, Liquid-Solid Half Space, *Bull. Seism. Soc. Amer.*, **52** (1962), 59-66.
- 52) NAFE, J.E. and C.L. DRAKE: Variation with Depth in Shallow and Deep Water Marine Sediments of Porosity, Density and the Velocity of compressional and Shear Waves, *Geophysics*, **22** (1957), 523-552.
- 53) TENG, T.: Reflection and Transmission from a Plane Layered Core-Mantle Boundary, *Bull. Seism. Soc. Amer.*, **57** (1967), 477-499.
- 54) ANDERSON, D.L.: Universal Dispersion Table, *Bull. Seism. Soc. Amer.*, **54** (1964), 681-726.
- 55) TAKEUCHI, H. et al.: Partial Derivatives of Surface Wave Phase Velocity with respect to Physical Parameter Changes within the Earth, *J. Geophys. Res.*, **69** (1964), 3429-3441.
- 56) BRUNE, J. and J. DORMAN: Seismic Waves and Earth Structure in the Canadian Shield, *Bull. Seism. Soc. Amer.*, **53** (1963), 167-210.
- 57) HILL, M.N.: Seismic Refraction Shooting in an Area of the Eastern Atrantic, *Phil. Roy. Soc. London*, **A244** (1952), 561-596.
- 58) OLIVER, J. and J. DORMAN: On the Nature of Oceanic Surface Waves with Predominant Period of 6 to 8 seconds, *Bull. Seism. Soc. Amer.*, **51** (1961), 437-455.
- 59) DAVIES, D.: Dispersed Stoneley Waves on the Ocean Bottom, *Bull. Seism. Soc. Amer.*, **55** (1965), 903-918.